NUMERICAL STUDY OF MICROWAVE BACKSCATTERING

FROM BREAKING WATER WAVES

By

SHIOU-JYH JA

Bachelor of Science
National Chiao-Tung University
Hsin-Chu, Taiwan
1991

Master of Science
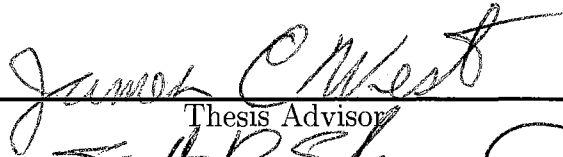Oklahoma State University
Stillwater, Oklahoma

1995

Submitted to the Faculty of the
Graduate College of the
Oklahoma State University
in partial fulfillment of
the requirements for
the Degree of
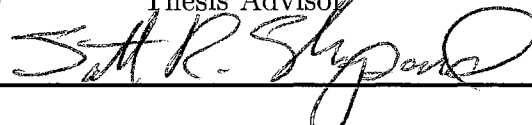DOCTOR OF PHILOSOPHY
December, 1999

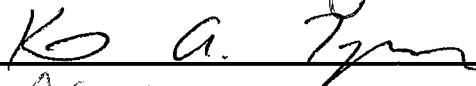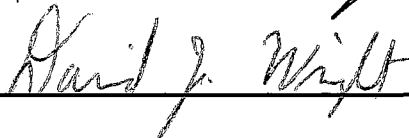# NUMERICAL STUDY OF MICROWAVE BACKSCATTERING

FROM BREAKING WATER WAVES

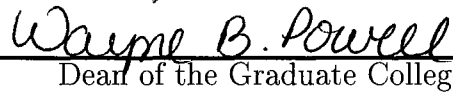Thesis Approved:

_____
Thesis Advisor

_____

_____

_____

_____
Dean of the Graduate College

ii

ACKNOWLEDGMENTS

I thank God for giving me all the wisdom and strength needed to finish this dissertation. This work is not possible to be done without His grace and many people's help. My dissertation advisor, Dr. James C. West, not only supported me throughout many years of studying, but also gave significant assistance and guidance to this study. I also would like to thank committee members, Dr. Keith Teague, Dr. Scott R. Shepard, and Dr. David Wright for their help and suggestions. My dear wife, Betty, supports me with all her love since we were married. She deserves to share this achievement with me. I also deeply appreciate the encouragement and prayers from our friends and relatives which help me to carried on.

TABLE OF CONTENTS

LIST OF FIGURES

vii

NOMENCLATURE

dB	decibels
ϵ	permittivity
$\mathbf{E^i}, E^i$	incident electric field
$\mathbf{E^s}, E^s$	scattered electric field
EFIE	electric field integral equation
GTD	geometrical theory of diffraction
$H_n^{(2)}$	n-th order Hankel function of second type
$H_n^{(1)}$	n-th order Hankel function of first type
$\mathbf{H^i}, H^i$	incident magnetic field
$\mathbf{H^s}, H^s$	scattered magnetic field
HH	horizontal polarization
j	$\sqrt{-1}$
$\mathbf{J}, J$	electric surface current density
k	wave number
K	surface wave number
KA	Kirchhoff approximation
l, l'	arc length along surface at observation, source
$L[]$	linear operator
λ	incident microwave wavelength

Λ	surface wavelength
$\mathbf{M}, M$	magnetic surface current density
MFIE	magnetic field integral equation
MM	moment method
μ	permeability
$\hat{\mathbf{n}}$	unit vector normal to surface
RCS	radar cross-section
ρ, ρ'	position vector of observation, source point
SPM	small perturbation method
TSM	two-scale model
θ_{local}	grazing angle of illuminating field (referenced to local facet)
θ_i	incident angle of illuminating field (referenced to vertical)
VV	vertical polarization

Chapter 1

INTRODUCTION

Microwave scattering from the ocean surface has been studied for more than thirty years. Sea-surface scattering is responsible for sea clutter that can mask the radar returns from targets on or above the surface. The scattering can also be analyzed directly to yield meteorological or oceanographical information. Numerous analytical models have been introduced to describe sea-surface scattering. One of the more successful models is the well-known two-scale model (TSM) [3][4].

The two-scale model (TSM) has been shown to accurately describe the ambient scattering at the small to moderate incidence angles. In this model, the scattering surface is divided into large- and small-scale surface components according to a certain threshold. Two different scattering models, the Kirchhoff approximation (KA) and the small perturbation method (SPM), are applied to the large- and small-scale components respectively to find the total scattered field. The KA [5] assumes that the large-scale surface has a large radius of curvature everywhere so that the surface current on the scatterer can be found from the physical optics approximation. For SPM [6], the scattered fields associated with the large-scale surface are perturbed using the small-scale roughness superimposed on the large-scale surface. SPM leads to Bragg-resonant scattering that is thought to be responsible for the ambient backscattering at moderate incidence angles [7]. Both KA and SPM are approximations of the exact solution, and other effects such as shadowing and multi-path scattering are

simplified or ignored. Therefore, TSM fails when the approximations under which it was derived are not met, which is usually the case at high incidence angles (Incidence angle is the angle between the radar look direction and vertical). At the more moderate incidence angles, TSM agrees with numerical calculations of the backscatter, but begins to lose accuracy at incidence angles greater than 75° [8].

Large-incidence sea-surface backscattering includes features that can not be explained by TSM. Experimental observations include Kalmykov and Pustovoytenko [9]. Trizna [10] gave a description of phenomena known as sea spikes: They often have horizontal-transmitted-horizontal-received (HH) polarization returns that exceed vertical-transmitted-vertical-received (VV) polarization returns, sometimes by as much as 10 dB. The HH sea spike echos typically have decorrelation times of several hundred milliseconds, while those of VV echos are only on the order of ten milliseconds. During sea spike events, the backscattered power can be more than 10 dB above the average value. Sea spikes can last up to a few hundred milliseconds. HH-to-VV backscattering ratios of greater than 0 dB are not predicted by TSM, which always gives a VV scattering greater than that at HH.

Sea spikes have been correlated with breaking waves in experimental observations [11], and they are much more common at high incidence angles (> 80°). Lee *et al.* [1] reported that sea spikes may be observed in Bragg scattering, but "super-events" where HH exceeds VV backscattering are exclusively related to non-Bragg scattering. Several models have been introduced to describe sea-spike scattering, such as wedge diffraction [12], specular reflection from a breaking wave at moderate incidence angles [13][14], bounded and tilted Bragg-resonant waves on the crest [15], and multi-path interference from the plume [16] (including Brewster angle damping effects [17]) at large incidence angles. Experimental studies have shown that polarization-independent specular reflection can be related to wave breaking events,
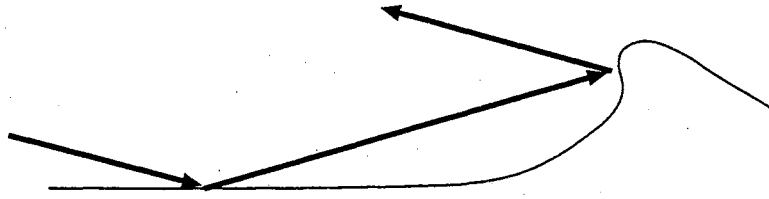
Figure 1.1: Multi-path scattering.

and can be a major contributor to the backscattering at moderate incidence angles [13][18]. However, specular reflection only predicts HH/VV ratios up to unity (0 dB), but not the "super-events" in which the HH/VV ratios are much greater than one. The multi-path scattering model [16] (Figure 1.1) relates the burst return power to the multiple-path reflection from the plume structure of a breaking crest. Polarization-dependent interference between the multi-paths can leads to very large backscattering and the HH > VV super events. Brewster angle damping can be incorporated into the multi-path model [17], which reduces the interference effects in VV scattering. The multi-path plus Brewster angle damping model has been supported by numerical simulations reported by West *et al.* [19] [20].

Another feature of high-incidence-angle scattering that TSM fails to predict is the difference in the frequencies at which peaks occur in the Doppler spectra of the HH and VV backscattering when looking in the upwind direction [21][22]. Each peak of the Doppler spectrum corresponds to the mean radial velocity of a scatterer. According to TSM, the peaks of the Doppler spectra of the two polarizations should occur at approximately the same frequency, with a larger magnitude at VV. Observations also have shown that the Doppler spectral peaks differ at the two polarizations (the Doppler "split") only under certain illumination conditions.

Lee *et al.* [1] experimentally demonstrated Doppler splitting in X-band (9 GHz) scattering from the open ocean. At moderate incidence angles when looking upwind the Doppler spectra of both polarizations show similar profiles with two Doppler shift peaks. The slower one is the Bragg-resonant peak which can be matched to the speed

wave propagation direction

orbital motion
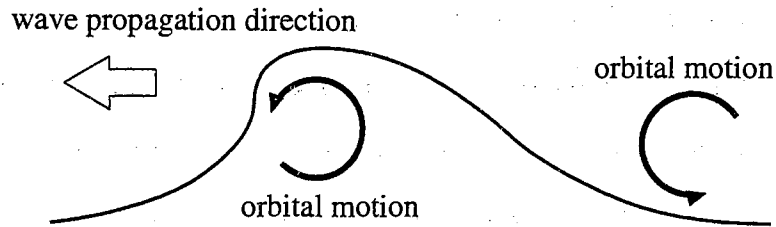
orbital motion

Figure 1.2: Orbital motion.

of freely-propagating short waves. As the incidence angle increases, the "slow peak" of HH gradually disappears from the HH spectrum while the "fast peak" becomes dominant. Conversely, the fast peak of VV diminishes while the slow one remains. Hence, Doppler splitting occurs (shown in Fig. 1.3(a)). The fast Doppler peak at VV is at 160 Hz, and the slow one at HH is at 100 Hz. The signals corresponding to the higher or lower Doppler shifts are termed "fast" or "slow" signals respectively. Super events can be observed in the fast signal at all incidence angles, while none can be seen in the slow signal. The slow signal characteristics agree with the predictions of TSM, so is also called the "Bragg signal". The fast signal is beyond TSM prediction, and hence is termed the " non-Bragg signal".

The Doppler shifts of fast scatterers have been experimentally measured to correspond to the phase velocity of the dominant wave on the surface [2][23]. Keller *et al.* [24] also report that the Doppler shift of the scattering during a breaking event corresponds to the phase velocity of the long wave. Lee *et al.* [1] also conjectured that "specular facets" may be possible source of the fast signal. The diffraction from the facet may give HH>VV, HH=VV, or HH<VV scattering, depending upon the facet size. The Doppler shifts of the slow signal can be matched to the total speed of the freely propagating small-scale waves [2]. This consists of the phase velocity of the Bragg-resonant small-scale wave, plus the orbital velocity of the large -scale waves that advect the small-scale waves. The large-scale wave orbital velocity is shown in Fig. 1.2.

4

In a later paper [2], Lee *et al.* presented observations of X-band backscattering from a plunging-breaking gravity wave mechanically-generated in a water tank. No wind was present in this study, so the Bragg-resonant scatter from small-scale waves distributed across the wave profile was much lower than would be expected in the open sea. During the wave breaking, the Doppler shift approached the frequency corresponding to the phase velocity of the gravity wave, giving a fast signal. Both VV and HH polarizations showed large backscatter (sea spike) and super events occurred in the fast signal. After the wave decayed and no breaking occurred, the Doppler shift dropped below the frequency of the phase velocity of the gravity wave giving a slow signal. The strength of the HH backscatter decreased by about 30 dB after breaking was completed, while VV dropped by about 10 dB. No super events occurred after breaking. They concluded that super events almost exclusively occur during the actual wave breaking process. HH/VV ratio can only approaches to but not exceed 0 dB when the wave is less energetic. The Doppler spectra measured by Lee *et al.* [2] at 89° incidence angle is redrawn in Fig. 1.3(b). A well-defined fast peak can clearly be seen at about 135 Hz in both HH and VV polarizations. A wider, lower magnitude slow peak appears at VV at 40 Hz. The wider bandwidth of the slow peak is due to the changing orbital velocity as the long wave propagates through the field of view. The slow Doppler peak of wave tank experiment results is much lower than that of the open-ocean observations, which is due to much less distributed roughness presented on the water tank surfaces. Peaks at around −120 Hz are the image signal due to the non-ideal quadrature mixers in the radar system.

In another study of open-ocean backscattering, Smith *et al.* [23] observed a Doppler splitting at 82° incidence and 3 GHz when looking upwind. In this case, the VV peak again appeared at a lower Doppler frequency than at HH, and had a 10 dB greater amplitude. However, when looking downwind both HH and VV spectra showed a

Return Loss Spectral Densigy (dB/Hz)

VV ———
HH --------

-20
-40
-60

slow
fast

-200   -100   100   200

Doppler Frequency (Hz)

(a)

80

60

Amplitude (dB)

40

20

HH

VV

slow
peak

fast peak

-240   -120   0   120   240

Doppler frequency (Hz)
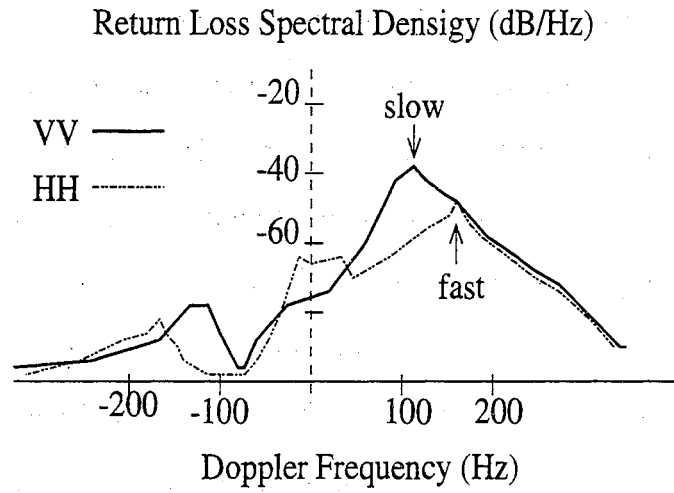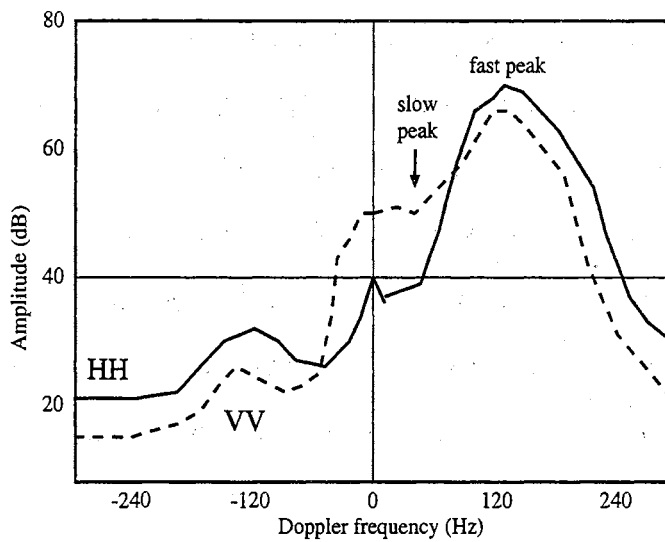
(b)

Figure 1.3: The redraw of Doppler spectra of the backscatter from (a) open-sea waves at 10° of incidence and (b) a machine-generated no-wind breaking wave at 11° of incidence in the upwind direction. The original figure is shown in Lee *et al.* [1] and [2] respectively.

6

Doppler peak at the slow speed, with the peak of HH being about 20dB lower. The down-wind looking scattering shows better agreement with the TSM predictions than when looking upwind. The change of the VV polarization Doppler spectra between downwind and upwind-looking is modest. The upwind/downwind asymmetry of HH polarization spectra is quite large, which shows a upward shift in the frequency of the Doppler peak and an increase in the amplitude of the peak when looking upwind.

Similar experimental results have been observed by Plant [15] at Ku band (14 GHz). He observed one dominant Doppler shift peak at lower speeds for both polarizations in the downwind and cross-wind looking direction, but saw the VV and HH Doppler peaks shift to slow and fast scatterer speeds respectively when looking upwind at high ($\geq$ 80°) incidence angles. Plant proposed a centimetric bound and tilted wave model to describe both the large HH returns and the Doppler split at high incidence angles. The model assumes that the fast-scatterer Doppler shifts are due to a Bragg resonance between capillary waves that are bound to the front face of the steepened longer waves. The local incidence angle for these Bragg scatterers is greatly reduced due to the tilt of the front face, giving anomalously high HH scattering that can be predicted by TSM. Because these bound waves propagate at the dominant wave speed, they would lead to the "fast scatterer" response in the HH Doppler spectra. However, this model still relies upon the TSM, and thus can not explain the super events.

Most studies in the literature have examined the statistics of the radar scattering. When the radar illuminates a patch of water surface, the echos from many different scattering centers are received, and are coherently added together. An ensemble average is then applied to estimate the scattering statistics. Numerical studies often use Monte-Carlo treatment of a randomly generated surfaces to estimate the scattering statistics [25]. However, it is difficult to distinguish the contribution of individual

7

scatterers from those studies.

A numerical treatment of the scattering from deterministic surfaces gives the exact backscattered field, allowing independent scattering features to be identified. The target surface also can be artificially modified to add or remove surface features, which aids in the identification of the scattering mechanisms. Since the exact field is available, the numerical results can also be used to test the accuracy of existing scattering models such as TSM under realistic conditions.

In this paper, an existing numerical technique, a hybrid approach that combines the moment method with the geometrical theory of diffraction (MM/GTD) [26][27] is applied to measured surface profiles of breaking water waves. The surface profiles give a continuous representation of the evolution of a spilling-breaker wave, enabling the calculation of the time-history of both the amplitude and Doppler spectrum of the backscattering. The calculated scattering is then examined to identify the scattering mechanisms that yield fast and slow signal at large incidence angles. Some surface modifications are introduced to further identify the scattering mechanism, and the front face of the surface is extended to introduce multi-path scattering that yields super events. The usefulness of TSM in predicting the scattering from these spilling breakers is also examined.

Due to the limitation of the sample data and computer resources, only the scattering from one-dimensional rough surfaces (i.e. the surface is uniform in the azimuthal direction) is considered in this dissertation. Numerical treatment is very expensive and the 2-D rough problem is currently cost prohibitive. The goal of studying the performance of TSM is to identify the condition under which the analytically based models are valid so that they may be applied with confidence to the more complicated 2-D problem.

8

Chapter 2

BACKGROUND

This chapter explains the terminologies and concepts used in this dissertation. First the oceanographic terminology is introduced, followed by the electromagnetic concepts.

2.1 Oceanography

The wind blowing over the ocean surface generates waves (generally referred to as wind-waves). Wind waves can be divided into two categories. The primary restoring force that controls the propagation of waves that are shorter than 17.4 mm in wavelength is surface tension. These waves are therefore termed "capillary waves", and are characterized by round crests and v-shape troughs. Gravity is the dominant restoring force for longer waves, so waves in this region are termed "gravity waves". Small-magnitude gravity waves are more sinusoidal in shape, but become less so as the amplitude increases.

Wind waves are often statistically described by linear wave-number power spectra. The two most popular spectra are those introduced by Pierson and Moskowitz [28] and Donelan and Pierson [29]. This is a very limited description of the surface since only small-amplitude gravity waves approximately meet the linear assumption. As the wave amplitude increases the profile becomes non-sinusoidal, and eventually breaking
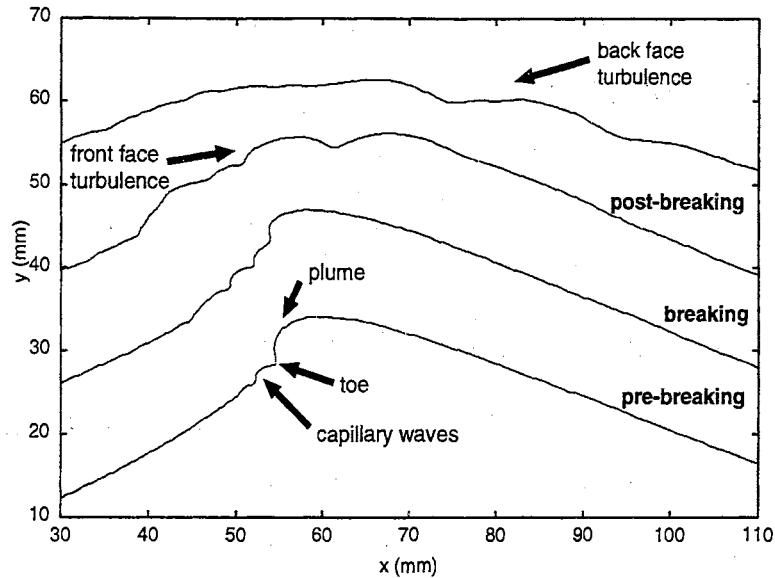
Figure 2.1: Typical features of water surface at different stages.

occurs. There are non-linear effects that can dramatically affect the backscattering.

Breaking waves can be roughly divided into two types, plunging and spilling. Plunging breakers are higher energy, and are characterized by a jet that moves faster than the wave crest, forming an air pocket beneath it. The jet is unsupported so collapses onto the front face of the wave, giving violent breaking. Spilling breakers are more gentle. They are more common in the open sea, but less well understood [30]. A spilling breaker begins when a bulge forms on the front face due to a mass of water that is moving faster than the phase velocity of the large wave (the "plume"). Parasitic capillary waves also form on the front face of the wave just behind the "toe" (where sharp concave curvature appears). Breaking appears as turbulence is generated in the underlying flow, which is then advected by the orbital motion of the large-scale wave. Examples of a spilling breaker at different times (taken from the data set to be used later in the scattering study) are shown in Fig. 2.1.

10
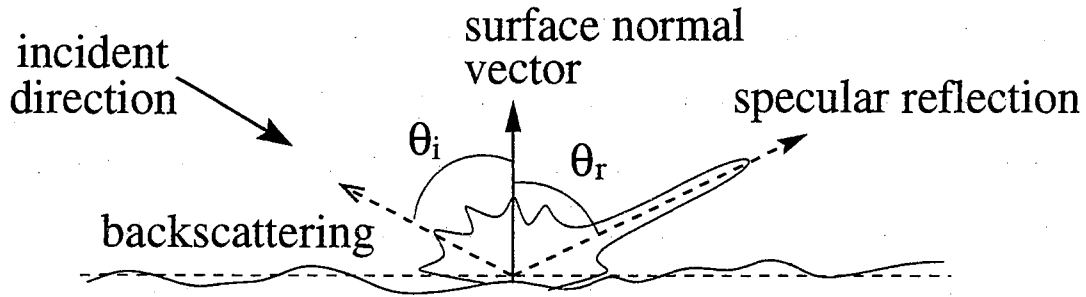
Figure 2.2: Geometry of scattering from a slightly rough surface.

2.2 Surface Scattering

2.2.1 Definitions

When an electromagnetic wave propagating in one medium, usually the free space, impinges upon another material of different constitutive properties (permittivity and permeability), some energy will be reflected back into the first medium and the remainder is transmitted into the second medium. The second medium in this scenario is termed the scatterer. The difference between the total field occurring with and without the scatterer in place is called the scattered field. The geometry of rough surface scattering is shown in Fig. 2.2. An incident plane wave is assumed. The θ_i and θ_r are the incident and reflection angles respectively. When the scattering surface is electromagnetically smooth, most of the scattered energy will propagate in the specular-reflection direction(i.e. $\theta_i = \theta_r$). When the surface is not smooth, significant energy may be scattered in all directions. This is called rough surface scattering.

One way to define a smooth plane is the *Rayleigh criterion,* which states that a surface is considered smooth if the phase difference of the scattered fields due to the difference of the surface height is less than $\pi/2$ radians [5]. Other stricter criteria use $\pi/4$ or $\pi/8$ phase difference. *Backscattering* (or *monostatic scattering)* refers to the energy scattered back to the transmitter along the same path of the incident energy.

As mentioned, due to computational complexity, only the two-dimensional scat-

11

tering from surfaces that are rough in one dimension (and uniform in the other) is considered. The scattering geometry is shown in Fig. 2.3. The surface displacement is in the y direction and depends upon x, but is uniform in z direction. The incident wave vector is $\mathbf{k_i}$. The global incidence angle is given by the angle between $\mathbf{k_i}$ and vertical, while the local incidence angle at a particular point on the wave is the angle between $\mathbf{k_i}$ and the surface unit normal vector $\hat{n}$. It is assumed that the distance between the transmitter and the target surface is large enough that the far-field approximation applies and both the incident field at the interface and the scattered field at the receiver propagate as uniform plane waves. Figure 2.3 shows a scattering geometry case, where the incident electric field is oriented in the horizontal (z) direction. This would corresponds to *perpendicular polarization* if the scattering surface were ideally planar. Exchanging the E- and H-field orientations yields *vertical polarization*, corresponding to *parallel polarization* in the flat-surface case. With a one-dimensionally rough surface the backscattered field is oriented the same as the incident field (no cross-polarized scattering is induced), so the horizontally polarized incident and scattered fields case is designated by HH (horizontal-transmitted-horizontal-received), and vertically polarized fields case is designated by VV (vertical-transmitted-vertical-received) .

Figure 2.3 also shows upwind illumination direction, where the incident vector is against the water wave propagation direction. Downwind illumination has the incidence vector looking in the wave propagation direction.

The *radar cross section* (RCS) of a scatterer is the equivalent area that intercepts an amount of incident energy that when re-radiated isotropically gives the same energy density at the receiver as received from the true scatterer. With a scatterer that is uniform in one dimension to infinity, a one-dimensional (1-D) RCS must be defined. This is given by [31]
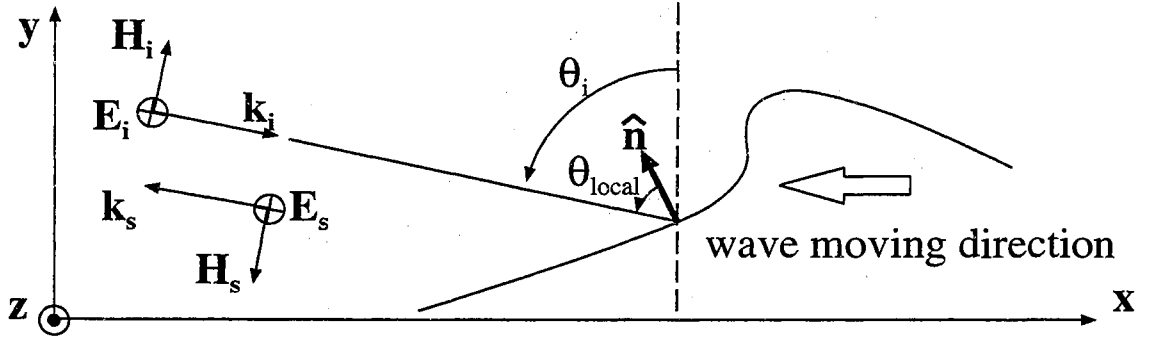
Figure 2.3: The geometry of 2-D backscattering from ocean surface in HH mode. The notation ⊕ indicates that the direction of the vector is going out of the paper.

$$\sigma_{1-D} = \lim_{\rho \to \infty} \left[2\pi\rho \frac{|E^s|^2}{|E^i|^2} \right]; \qquad \text{for deterministic surface} \qquad (2.1)$$

where ρ is the distance between scatterer and receiver, the E^i and E^s are the incident and scattered field. Random surfaces are usually described by a *scattering coefficient*, which gives the average RCS per unit length with 1-D rough surfaces. It is found from

$$\sigma^0_{1-D} = \lim_{\rho \to \infty} \left[\frac{2\pi\rho \langle E^s E^{s*} \rangle^2}{L |E^i|^2} \right] \qquad (2.2)$$

where L is the physical length, $\langle \bullet \rangle$ is the ensemble average, and the superscript $*$ stands for the complex conjugate. Since deterministic surfaces are used, RCS will be used in this study.

2.2.2 Bragg Scattering

If a rough surface includes energy at the appropriate wave number, strong backscatter may result from a resonant interaction between the radar waves and the surface roughness energy [7]. This mechanism is termed Brag scattering since it is similar to Bragg-resonant scattering in x-ray crystallography. Bragg scattering can be strong even when the Bragg-resonant wave energy is of very small amplitude. The geometry

13
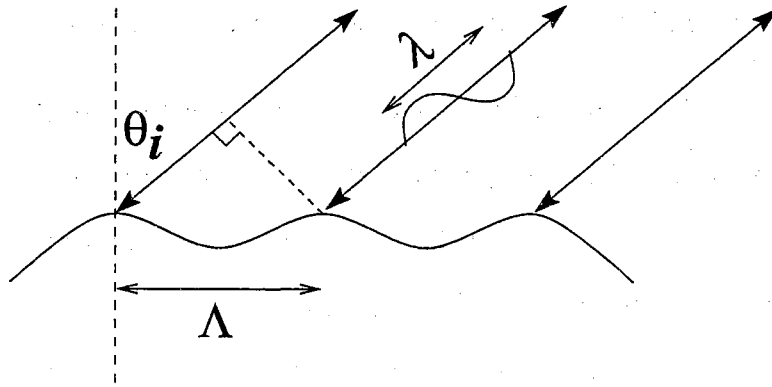
Figure 2.4: Bragg-resonant condition for backscattering.

of the Bragg resonance is illustrated in Fig. 2.4. The resonance condition is found from

$$2\Lambda\sin(\theta_i) = \lambda \tag{2.3}$$

where θ_i is the incidence angle, λ is the microwave wavelength, and Λ is the Bragg-resonant surface wavelength. Bragg resonance can also be written as $K = 2k\sin\theta_i$, where K is the Bragg-resonant surface wave number and k is the radar wave number. When the Bragg condition is met, the round-trip path lengths to points of identical displacement on the resonant wave differ by integer multiples of λ, which leads to constructive interference. Bragg-resonant scattering is directly predicted by the small-perturbation scattering model that is described in the next chapter. It acts as a filter which selects the matched surface component from the continuous spectrum of the target surface. Therefore, although no periodic structure appears on the surface, Bragg scattering can be observed as long as there is significant energy at the Bragg-resonant wave number in the surface roughness spectrum.

2.2.3 Quasi-Specular Scattering and the Facet Model

Most energy incident upon a slightly rough surface will be reflected in the specular direction. Therefore, the strength of the backscattering is usually much smaller than the scattering in the specular-reflection direction. However, if the surface is very rough or the slopes at some points are sufficiently high, there may be points where the incident vector is approximately parallel to the local surface normal. This leads to strong backscattering, known as quasi-specular scattering [32]. Bore features on the crests of breaking waves can lead to quasi-specular reflection even at high incidence angles. Simple models of quasi-specular reflection are based on optical approximations, so do not predict a polarization dependence.

The target surface can be subdivided into small consecutive segments as shown in Fig. 2.5. The lengths of the segments are chosen so that the additional surface roughness beyond that modeled as a planar facet across the segment is electromagnetically small. A local incidence angle can be defined relative to the normal of the planar facet. Including the electromagnetically-small roughness on the facets yield the complete surface segment, often referred to as a "slightly-rough facet". Each slightly-rough facet can be treated as a distinct scattering unit, and since the displacement away from ideally planar is electromagnetically small the small-perturbation approach or Kirchhoff approximation to be described in Chapter 3 can be used, depending upon the local angle of incidence. Not all surface features can be adequately described by slightly-rough facets.

2.3 Electromagnetic Theory

The source of a scattered field is the re-radiation of the current induced on or within the scatterer by the incident filed. Numerical calculation of the volume current in-
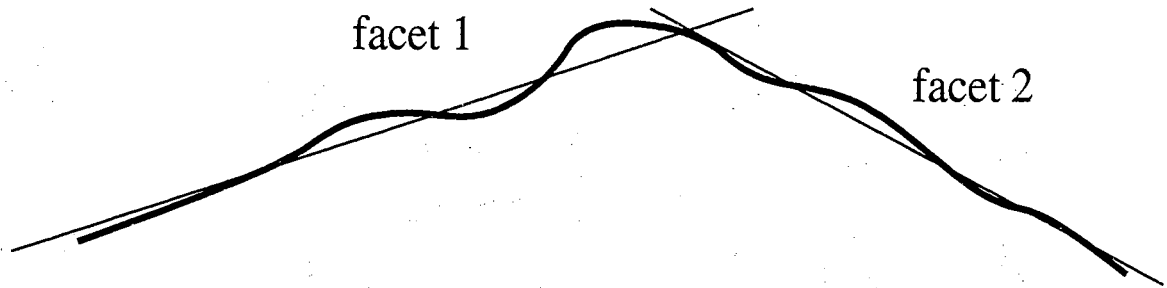
Figure 2.5: Facet model.

duced within a scatterer is numerically cost prohibitive. Instead an equivalent problem [31] is solved as shown in Fig. 2.6. Part (a) of the figure shows the electric and magnetic source current ($\mathbf{J}$ and $\mathbf{M}$) radiating into free space, thus giving the incident field $\mathbf{E}^i$ and $\mathbf{H}^i$. The scattering surface is added in part (b) giving the scattered field $\mathbf{E}^s$ and $\mathbf{H}^s$ to be found. The boundary conditions give a continuous tangential component of electric and magnetic field across the boundary. The equivalent problem to be solved numerically is shown in Fig. 2.6(c). It has the same constitutive parameters (permittivity ϵ_1 and permeability μ_1) above and below the interface, therefore a physical boundary no longer exists. The equivalent surface currents on the virtual boundary that insure the fields meet the boundary conditions are

$$\mathbf{J}_s = \hat{\mathbf{n}} \times (\mathbf{H}^i + \mathbf{H}^s) \tag{2.4}$$

and

$$\mathbf{M}_s = -\hat{\mathbf{n}} \times (\mathbf{E}^i + \mathbf{E}^s) \tag{2.5}$$

where $\mathbf{J}_s$ and $\mathbf{M}_s$ are the equivalent electric and magnetic surface currents. These equivalent currents plus the source currents give the incident plus scattered field above the surface and zero field below the scatterer. Once the equivalent surface currents are known, it is straightforward to compute the scattered field. Therefore, the goal of the scattering problem becomes finding the equivalent surface current. The numerical
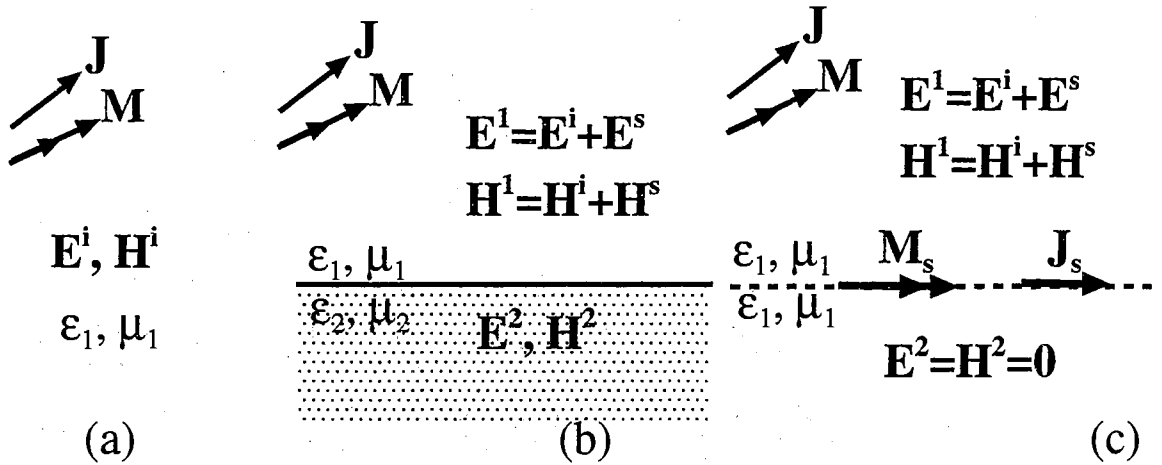
Figure 2.6: Equivalent for finite conductivity scatterer.

technique which is described in the next chapter serves this purpose. Note that the equivalence principle can only be applied to homogeneous scatters.

The perfect electric conductor (PEC) scattering problem is a special case of the general scattering medium case of Fig. 2.6. The equivalent magnetic surface current vanishes, and the equivalent electric surface current becomes the physical surface current.

Chapter 3

REVIEW OF SCATTERING MODEL AND NUMERICAL TECHNIQUE

3.1 Introduction

The most commonly used model to describe sea-surface scattering is the two-scale surface model (TSM) (also called the composite surface model (CSM)). It was introduced in the 1960's [33][4] and has been successfully used to describe ocean surface scattering at small and moderate incidence angles [33]. This model combines two different scattering models: the Kirchhoff approximation (KA) and the small-perturbation method (SPM). Each of these two approaches alone has its own advantages and limitations. The former is suitable for gently undulating surfaces and most accurately predicts specular-like scattering, while the latter applies to small-displacement, rapidly-changing surfaces and gives Bragg-resonant scattering .

TSM divides the roughness energy of the target surface into a superposition of a slowly undulating component and a rapidly changing component. In the ocean-surface case, the gently undulating surface usually has an electromagnetically large amplitude, and hence is typically called the large-scale surface. The rapidly fluctuating surface has an electromagnetically small amplitude, and hence is called the

small-scale surface. In the two-scale model, KA is applied to the large-scale surface to compute a partial scattered field. SPM is then applied to the small-scale surface yield a second partial field. Addition of the two partial fields gives the two-scale model field.

Most implementations of the two-scale model include ensemble averaging to yield a scattering coefficient [34]. These implementations are therefore applicable only to random surfaces. Here the fields directly scattered from deterministic surfaces are of interest. Therefore, the two-scale model formulation of Brown [35] which gives the KA and SPM fields associated with individual surface profile is used. The coherent addition of the two field terms yields the TSM field that is compared to the direct numerical calculations.

Analytical rough-surface scattering models have limited ranges of application that are not always well understood. Numerical calculation of the "exact" scattered field is therefore also used in this work. As mentioned in the previous chapter, the equivalent induced surface currents on the boundary of the equivalent problem are found first. The scattered field is then calculated from the radiation equation. The moment method (MM) will be used to find the equivalent surface currents. This discretizes an appropriate integral equation to yield a linear system of equations that are solved to yield the surface current. The radiated fields from the calculated discretizes current is computed to give the scattered field. The MM solution can be found to very high accuracy, so can be used as a reference solution to which the predictions of analytical models are compared. The implementation of MM used here is the hybrid approach extending MM by the geometrical theory of diffraction (GTD) as proposed by Burnside et al. [26] for perfectly conducting surface and extended to finite conductivity surfaces by West et al. [27]. Computer codes programmed by J. C. West and J. M. Sturm were used in this work. Details of MM/GTD numerical technique will be

reviewed in Sec. 3.4.

3.2 Analytical Scattering Models

3.2.1 Kirchhoff's Approximation

As previously described, the original scattering problem can be transformed to an equivalent problem in which the scattered fields are found from the radiation of equivalent surface currents of the scatterer boundary [31]. The Kirchhoff approximation approximates the equivalent current by assuming that the incident field impinges upon an infinite plane tangent to the point of incidence. This approximation works well when the the radius of curvature of the surface is relatively large compared to the wavelength of the incident wave. Hence, the equivalent surface current can be accurately approximated without the *a priori* knowledge of the scattered field.

The two-dimensional scattering geometry is shown in Figure 3.1. The equivalent surface currents can be approximated by the tangent-plane approximation [36]

$$
\mathbf{J_{KA}} = \begin{cases} \hat{n} \times \mathbf{H^1}\big|_{surface} = (1-\Gamma)\,\hat{n} \times \mathbf{H^i}\big|_{surface} & ; \ illuminated\,area \\ 0 & ; \ shadowed\,area \end{cases} \tag{3.1}
$$

and

$$
\mathbf{M_{KA}} = \begin{cases} -\hat{n} \times \mathbf{E^1}\big|_{surface} = -(1+\Gamma)\,\hat{n} \times \mathbf{E^i}\big|_{surface} & ; \ illuminated\,area \\ 0 & ; \ shadowed\,area \end{cases} \tag{3.2}
$$

where $\mathbf{J_{KA}}$ and $\mathbf{M_{KA}}$ are the approximate electric and magnetic current densities respectively, the $\mathbf{H^1}(\mathbf{E^1})$ is the total magnetic(electric) field in media 1, Γ is the reflection coefficient at the incident point where the boundary is assumed to be an infinite tangent plane, and $\hat{n}$ is the surface normal vector toward media 1. Equations
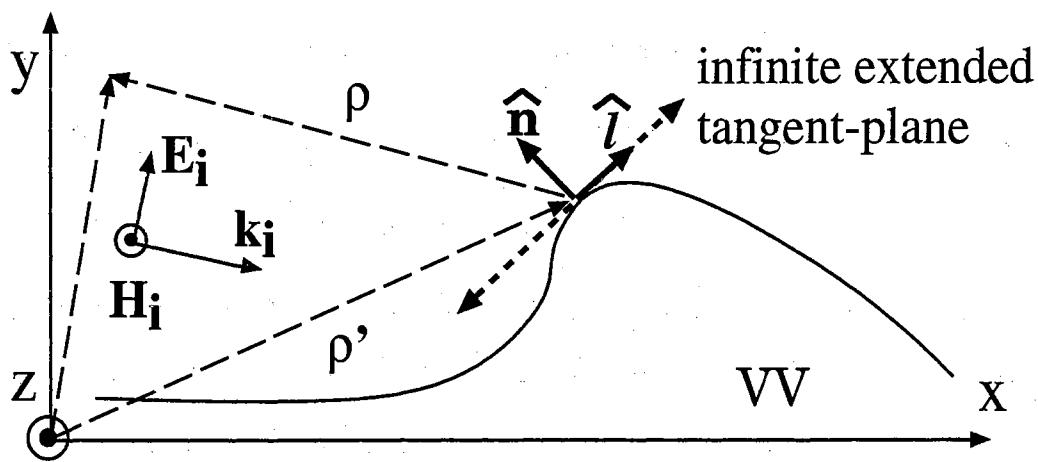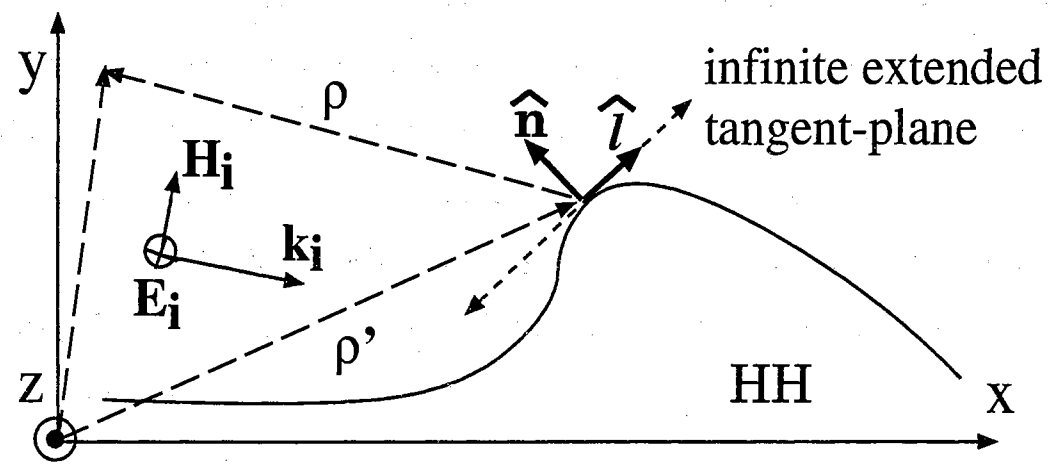
Figure 3.1: Scattering geometry in VV (upper plot) and HH (lower plot) polarization.

(3.1) and (3.2) are the general Kirchhoff approximation for any non-perfectly conducting scattering medium. For the highly conducting surface such as sea water, the relation between $\mathbf{J_{KA}}$ and $\mathbf{M_{KA}}$ can be related via the impedance boundary condition which is introduced later in Sec. 3.4.2.

With a perfect electric conductor (PEC) scatterer $\Gamma = -1$, so the electric surface current magnitude is just twice of the tangential component of the incident magnetic field on the surface. Once the KA current is found then the far field scattered field can be calculated numerically via the radiation equations [31]. The geometry is shown in Fig. 3.1. The scattered fields are found by integrating the radiation of electric surface current along the contour of the scatterer. For HH polarization, the scattered electric field can be found by

$$
\begin{aligned}
E_z^s(\boldsymbol{\rho}) \;=\; & \frac{k\eta_0}{4} \int_c J_z(l')\, H_0^{(2)}(k|\boldsymbol{\rho} - \boldsymbol{\rho}'|)\, dl' \\
& + j\frac{k}{4} \int_c M_l(l')(\hat{n}' \cdot \frac{\boldsymbol{\rho} - \boldsymbol{\rho}'}{|\boldsymbol{\rho} - \boldsymbol{\rho}'|})\, H_1^{(2)}(k|\boldsymbol{\rho} - \boldsymbol{\rho}'|)\, dl',
\end{aligned}
\tag{3.3}
$$

At VV polarization it is easier to find the scattered magnetic field

$$
\begin{aligned}
H_z^s(\boldsymbol{\rho}) \;=\; & -j\frac{k}{4} \int_c J_l(l')(\hat{n}' \cdot \frac{\boldsymbol{\rho} - \boldsymbol{\rho}'}{|\boldsymbol{\rho} - \boldsymbol{\rho}'|})\, H_1^{(2)}(k|\boldsymbol{\rho} - \boldsymbol{\rho}'|)\, dl' \\
& - \frac{k\eta_0}{4} \int_c M_z(l')\, H_0^{(2)}(k|\boldsymbol{\rho} - \boldsymbol{\rho}'|)\, dl'
\end{aligned}
\tag{3.4}
$$

In equation (3.3) and (3.4) the superscript s refers to scattered field, the subscript z represents the z-direction component, the subscript l is the direction tangential to the surface along the surface arc-length, k is the wave number, η_0 is the free space intrinsic impedance, $J_{z,l}(l')$ and $M_{z,l}(l')$ are the KA current, $H_n^{(2)}$ is the nth order Hankel function of the second type, $\boldsymbol{\rho}$ and $\boldsymbol{\rho}'$ are the position vector of the observation and source point, $|\boldsymbol{\rho} - \boldsymbol{\rho}'|$ is the distance between the source and observation point, and l is the arc length of each differential segment of the scatterer surface profile. For far-field scattering, the Hankel functions can be replaced by their large-argument asymptotic approximations:
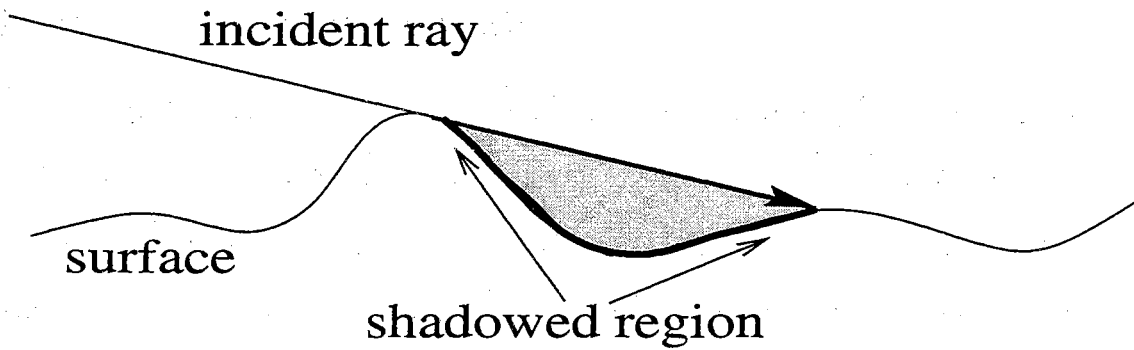
Figure 3.2: Surface shadowing

$$H_0^{(2)}(k\rho) \overset{k\rho\to\infty}{\Longrightarrow} \sqrt{\frac{2j}{\pi k\rho}}e^{-jk\rho}$$

$$H_1^{(2)}(k\rho) \overset{k\rho\to\infty}{\Longrightarrow} j\sqrt{\frac{2j}{\pi k\rho}}e^{-jk\rho}$$

One limitation of KA is the tangent-plane assumption. It assumes that the interface where the incident ray hits is an infinitely extending planar interface. Therefore, the radius of curvature of the surface must be large with respect to the electromagnetic wavelength for a valid result. A second limitation of KA is that the interactions among different portions of the surface are ignored. That is, the fields scattered from one part of the surface to another are not taken into account. Therefore, KA does not predict the multi-path reflection which is thought to be important at high incidence angles. Finally, surface self-shadowing is not accurately represented by KA. The shadowing effect can be roughly approximated by simply setting the surface current in the shadowed region to zero, as shown in Fig. 3.2. However, at the high incidence angles large sections of the surface are shadowed, and the diffracted and multi-path scattered fields from other surface patches becomes more important in the shadow region than at moderate incidence angles [8].

3.2.2 Small-Perturbation Method

The small-perturbation method (SPM) was introduced by Rice [6] in 1951. SPM is formulated for target surfaces that have electromagnetically small surface heights displacement and small r. m. s. slopes. The fields outside and inside the scatterer are expanded in a perturbation series in the surface wave-number domain. If the conditions listed are satisfied, then a truncated perturbation series can be used to approximate the fields, and the scattered field can be found by matching the surface boundary conditions. Here we use first-order SPM, which includes the zeroth (KA applied to a planar surface) and first order terms of the perturbation series. Higher order perturbation terms can also be found [37], but here "SPM field" refers first-order SPM field only.

Ulaby gives the first-order perturbation field as

$$E_{pp} = \frac{1}{2\pi} \int_{-\infty}^{\infty} (j2k\cos\theta \alpha_{pp} Y) e^{-jk_x x'} dk_x; \quad p = h \, or \, v \tag{3.5}$$

where h and v stand for horizontal and vertical polarization, k_x is the x-component of the surface wave number k, Y is the Fourier transform of the surface height, θ is the incidence angle, and α_{pq} is given by

$$\alpha_{hh} = \frac{\cos\theta_i - \sqrt{\epsilon_r - \sin^2\theta_i}}{\cos\theta_i + \sqrt{\epsilon_r - \sin^2\theta_i}}$$

$$\alpha_{vv} = (\epsilon_r - 1)\frac{\sin^2\theta_i - \epsilon_r\sqrt{1 + \sin^2\theta_i}}{[\epsilon_r \sin\theta_i + \sqrt{\epsilon_r - \sin^2\theta_i}]^2}.$$

When a randomly rough surface is considered, the scattering coefficient can be computed by ensemble averaging the scattered field as given by (2.2). The resulting 1-D scattering coefficient derived by first order SPM is [7]

$$\sigma_{pp} = 4k^3 \sigma_l^2 \cos^4\theta_i |\alpha_{pp}|^2 W(2k\sin\theta_i); \quad p = h \, or \, v \tag{3.6}$$

where σ_{pp} is the scattering coefficient for VV or HH, σ_l^2 is the variance of the surface height, θ_i is the incidence angle, ϵ_r is the dielectric constant of the scatterer, and $W(2k\sin\theta_i)$ is the Fourier transform of the surface correlation coefficient evaluated at the Bragg wave number (often termed the *normalized roughness spectrum* in the literature). The normalized roughness spectrum at the Bragg wavenumber is found from

$$W(2k\sin\theta_i) = \frac{1}{2\pi} \int_{-\infty}^{\infty} \int_{-\infty}^{\infty} \rho(u,v) \exp[-jk_x u - jk_y v] \, du \, dv \qquad (3.7)$$

where $k_{x,y}$ are the vector component of the electromagnetic wave number in the x and y directions respectively, and $\rho(u,v)$ is the surface correlation coefficient.

Equation (3.6) shows that the scattering coefficient depends directly on the surface roughness spectrum $W(K)$ at the Bragg resonance condition, $K = 2k\sin\theta_i$. Therefore, Bragg scattering is predicted by first-order SPM. First-order SPM also includes a polarization-dependence factor α_{pp}.

Sea-surface Bragg-resonant scattering theory was formulated assuming that several periods of the Bragg-resonant wave appear on the surface. However, as will be shown, deterministic SPM can also accurately model the scattering from deterministic surface features that do not show wave-like structure, such as small-scale bore features on the wave profile. A Fourier transform of the feature does yield energy at the Bragg-resonant wave number. However, this effect is not consistent with the original interpretation of Bragg scattering, and therefore is not referred to as Bragg scattering. Instead this is simply called diffractive scattering. "Bragg scattering" is used when there is obviously several periods of Bragg-resonant waves on the surface.

3.3 Two-Scale Model

3.3.1 TSM Implementation on Deterministic Surfaces

In past research, the statistics of sea echos were studied. Hence traditional SPM implementations find a scattering coefficient by ensemble averaging the SPM scattering cross-sections, as in (3.6). However, scattering widths of deterministic surfaces prior to ensemble averaging are treated in this work. Hence the above mentioned method can not be applied directly.

As mentioned, Brown [35] presented an analytical technique to find the first-order SPM field via the boundary perturbation approach developed by Burrows [38]. This technique allows the calculation of the scattering from a deterministic surface through SPM. The target surface is separated into large- and small-scale components via some criteria. The large-scale surface must be sufficiently smooth for KA to be applied, and the roughness of the small-scale surface must be small compared to the electromagnetic wavelength for the application of SPM. The zeroth-order scattering is computed from the large-scale surface via KA, then the first-order result is calculated by perturbing the field from the large-scale surface using the small-scale surface displacement. Assuming a perfectly conducting surface, the KA field scattered by the large-scale surface is

$$E^0_{pp,PEC} = -j\frac{k}{4\pi}\sqrt{\frac{-j2\pi}{k\rho}}\exp(-jk\rho)\int (\hat{n}\cdot\hat{k})\exp(-j2k\cdot\rho')\,dl'; \quad p = h \, or \, v, \quad (3.8)$$

and the first-order perturbation field is found from

$$E^1_{pp,PEC} = \frac{k^2}{\pi}\sqrt{\frac{-j2\pi}{k\rho}}\exp(-jk\rho)\int [2(\hat{n}\cdot\hat{e}_p)^2 + (\hat{n}\cdot\hat{k})^2]\exp(-j2k\cdot\rho')y_s\,dl' \quad (3.9)$$

where ρ and ρ' are the position vectors of the observation and source point respectively, $\hat{n}$ is the unit normal vector of the large-scale surface, $\hat{e}_p$ is the unit vector of incident

electric field, y_s is the displacement of the small-scale surface, and the integration is along the large-scale surface contour.

Equation 3.9 was derived assuming perfect conductivity. It is modified to account for finite surface conductivity by multiplying the following factor into the integrand of equation (3.9) [39]:

$$A_{hh} = \frac{\alpha_{hh}|_{FC}}{\alpha_{hh}|_{PEC}} = -\frac{\cos\theta_l - \sqrt{\epsilon_r - \sin^2\theta_l}}{\cos\theta_l + \sqrt{\epsilon_r - \sin^2\theta_l}} \qquad (3.10)$$

$$A_{vv} = \frac{\alpha_{vv}|_{FC}}{\alpha_{vv}|_{PEC}} = \frac{-\cos^2\theta_l}{1 + \sin^2\theta_l}(\epsilon_r - 1)\frac{\sin^2\theta_i - \epsilon_r\sqrt{1 + \sin^2\theta_i}}{[\epsilon_r\sin\theta_i + \sqrt{\epsilon_r - \sin^2\theta_i}]^2}$$

where $\alpha_{pp}|_{FC}$ and $\alpha_{pp}|_{PEC}$ signify α_{pp} with finite and perfect conductivity surface respectively.

The TSM field is the coherent (phase-preserved) addition of the KA and SPM fields. The surface self-shadowing effect is included by simply setting the SPM field to zero when the angle between incident wave vector and surface normal vector is less than 90°.

3.3.2 Surface Separation

A procedure must be developed to divide an arbitrary rough surface into large- and small-scale components. This is usually accomplished by applying linear low-pass and high-pass filters that yield the large- and small-scale surfaces respectively. Several surface wave number thresholds have been used as the cutoff point for these filters. For example, Brown [35] used a filter cutoff wave number of $K_c \cong \frac{k}{3}$, which gives $4k^2\overline{y_s^2} = 0.1$ for random rough surfaces which follow a linear Pierson-Moskowitz wind-wave spectrum. Durden and Veseky [40] numerically applied the moment method to Pierson-Moskowitz-spectra surfaces and found that the conventional TSM was most accurate when $K_c \cong \frac{k}{2}$ at moderate incidence angles, but increased to slightly less than

27

k at the highest incidence angles. Johnson *et al.* [25] also used the $K_c \cong \frac{k}{2}$ threshold for a numerical Monte-Carlo study with the surface realizations by generated from the linear Pierson-Moskowitz spectrum, and had good agreement between the TSM and MM results at incidence angles ranging from 0° to 60° of incidence. In treating directly measured wind-roughened surfaces, West et.al. [41] used the threshold

$$K_c = \begin{cases} \frac{k}{1.5}, & \theta_i \leq 30° \\ \frac{k}{3.0}, & \theta_i > 30° \end{cases} \tag{3.11}$$

where the K_c is the cutoff surface wave number.

In the following work, the threshold

$$K_c = k \tag{3.12}$$

will be used. This was determined empirically beforehand by applying different thresholds and comparing the TSM and MM results. The procedure for surface separation is given in Chapter 5.

3.4 Numerical Technique

3.4.1 Moment Method for PEC Scatterer

The moment method numerically solves an integral equation describing the electromagnetic boundary conditions at the scatterer surface to yield the equivalent surface current density. Once the surface currents are found, the scattered field is calculated from the far-field radiation of the currents. The boundary condition of the scattering problem can be expressed by two different integral equations, the electrical field integral equation (EFIE) or the magnetic field integral equation (MFIE), depending on the particular field boundary condition that is applied to the surface. The EFIE

which matches the electric field at the boundary is most easily applied at HH polarization. At the surface of a perfect electric conductor, the electrical field boundary condition is

$$\hat{n} \times \mathbf{E^i}\Big|_{on\,the\,boundary} = -\hat{n} \times \mathbf{E^s}\Big|_{on\,the\,boundary}.$$ (3.13)

Using the two-dimensional scattered field in (3.3) with only the electric surface current (since a perfectly conducting surface is assumed), and recognizing the incident field has only a z-component, (3.13) becomes the EFIE [31] :

$$\begin{aligned} E_z^i(\rho) &= \frac{k\eta_0}{4} \int_c J_z(l') H_0^{(2)}(k|\boldsymbol{\rho} - \boldsymbol{\rho}'|)\, dl' \\ &= L_E[J_z(l)] \end{aligned}$$ (3.14)

where the notations are the same as those in (3.3). At VV polarization the MFIE which matches the magnetic field is more easily applied. The magnetic field boundary condition is

$$\mathbf{J_s} = \hat{n} \times (\mathbf{H^i} + \mathbf{H^s})\Big|_{on\,the\,boundary}$$ (3.15)

Using the scattered field of (3.4) in (3.15) and again assuming perfect conductivity gives the MFIE [31]

$$\begin{aligned} H_z^i(\rho) &= -0.5 J_l(l') - j\frac{k}{4} \oint_c J_l(l') \left(\hat{n}' \cdot \frac{\boldsymbol{\rho} - \boldsymbol{\rho}'}{|\boldsymbol{\rho} - \boldsymbol{\rho}'|} \right) H_1^{(2)}(k|\boldsymbol{\rho} - \boldsymbol{\rho}'|)\, dl' \\ &= -L_M[J_l(l)] \end{aligned}$$ (3.16)

The integration is the principle value integral around the singularity at $\rho = \rho'$.

The EFIE and MFIE can be solved numerically by the moment method (MM) [42]. The moment method expands the unknown current into a series of basis functions, given by

$$\mathbf{J_s} = \hat{\mathbf{i}} \sum_{n=1}^{N} \alpha_n f_n; \quad \hat{\mathbf{i}} = \begin{cases} \hat{\mathbf{z}}; & for\,HH \\ \hat{\mathbf{l}}; & for\,VV \end{cases}$$ (3.17)

29

where the α_n's are unknown coefficients to be found and f_n's are the basis function. For the HH polarization, the residual is defined as

$$R = E_z^i - \sum_{n=1}^{N} \alpha_n L_E(f_n) \tag{3.18}$$

Due to only a limited number of basis functions being used, the residual can only be minimized in the weighted manner. The weighted residual is defined as

$$R_m = \langle W_m , R \rangle = \left\langle W_m , E_z^i(l) \right\rangle - \left\langle W_m , \sum_{n=1}^{N} \alpha_n L_E[f_n(l)] \right\rangle \tag{3.19}$$

where

$$\langle w(l) , g(l) \rangle = \int w^*(l) \cdot g(l) \, dl$$

W_m is the mth weighting function. Forcing the weighted residual to zero gives

$$\sum_{n=1}^{N} \alpha_n \langle W_m(l) , L_E[f_n(l)] \rangle = \left\langle W_m(l) , E_z^i(l) \right\rangle \tag{3.20}$$

Equation (3.20) can be written in matrix form as

$$[A_{mn}][\alpha_n] = B_m \tag{3.21}$$

$$A_{mn} = \langle W_m(l) , L_E[f_n(l)] \rangle$$

$$B_n = \left\langle W_m(l) , E_z^i(l) \right\rangle$$

The unknown coefficients α_n can now be found by solving this matrix equation using ordinary linear algebra techniques, giving the MM solution.

The usual approach for rough surface scattering calculations is to use sub-domain pulse basis functions for the current expansion, given by

$$f_n(l) = \begin{cases} 1; & l_n - \frac{\Delta}{2} \leq l < l_n + \frac{\Delta}{2} \\ 0; & otherwise \end{cases} \qquad n = 1...N \tag{3.22}$$

where Δ is the size of the sub-domain. Impulse functions located at the center of each pulse basis function are typically used for the weighting functions, given by

$$W_m(l) = \delta(l - l_m)$$

where $\delta(l)$ is the Dirac delta function. Note that since $\langle \delta(l - l_m), R(l) \rangle = R(l_m)$, the surface boundary conditions are forced to be met exactly at discrete points. This approach is therefore also termed "point collation" or "point matching" [31]

This choice of basis and weighting functions divides the surface into N discrete segments. The matrix element A_{mn} describes the electromagnetic interaction between the individual segments, so any diffraction and multi-path scattering effect are included in moment method solution. Use of smaller and smaller basis function will converge the MM solution to the exact solution in the absence of round-off error. The MM solutions are therefore typically used as the exact reference solutions [34].

3.4.2 Moment Method for Sea Water

The surfaces to be considered in this work consist of sea water, which has a large but finite conductivity. The moment method must be modified to account for the finite conductivity surface. With finite conductivity, a volume current rather than a surface current is induced to give the scattered field. The MM is not well suited to find volume currents. However, since the scattering medium is homogeneous, the equivalent problem of Fig. 2.6 can be solved. The equivalent problem includes both electric and magnetic surface currents. Both currents can be expanded in basis function series. However, this doubles the number of unknowns to be found, which increases the computational complexity of the MM solution as much as eightfold [43]. Instead we use an impedance boundary approach which requires only one current component to be found.

Senior [44] showed that when the scatterer has sufficiently large dielectric constant and conductivity that the following conditions are met

$$|N| \gg 1, \qquad |\text{Im}(N)k\rho_l| \gg 1 \qquad (3.23)$$

where $N = \sqrt{\epsilon_r}$ is the complex refraction index and ρ_l is the radius of curvature at

that surface point, the field transmitted into the scatterer will approximately propagate normal to the interface. Therefore, the two equivalent sources can then be approximately related as

$$\mathbf{M} = -Z_s \hat{\mathbf{n}} \times \mathbf{J} \tag{3.24}$$

where Z_s is the intrinsic impedance of the surface. This is the impedance boundary condition (IPB). Using this, only the unknown J_s must be found. West et al. [27] have derived the IPB EFIE and MFIE for sea water surfaces. Due to the additional magnetic current source, the scattered field is written as the sum of contributions from both the electric and magnetic current sources:

$$E_z^s = E_z^s(J_z) + E_z^s(M_l). \tag{3.25}$$

The boundary condition of equation 3.13, therefore becomes

$$E_z^i\Big|_{on\,the\,boundary} = - \left[E_z^s(J_z) + E_z^s(M_l)\right]\big|_{on\,the\,boundary}$$

The first term on the right hand side is $L_E(J_z)$ of (3.14). The second term is found by applying duality to (3.16), giving

$$E_z^s(M_l(l'), \boldsymbol{\rho}) = 0.5M_l(l') + j\frac{k}{4}\int_c M_l(l')(\hat{n}' \cdot \frac{\boldsymbol{\rho} - \boldsymbol{\rho}'}{|\boldsymbol{\rho} - \boldsymbol{\rho}'|}) H_1^{(2)}(k|\boldsymbol{\rho} - \boldsymbol{\rho}'|)\,dl'. \tag{3.26}$$

The magnetic current source in (3.26) is replaced by the electric current source via (3.24), giving

$$\begin{aligned} E_z^s(M_l(l'), \boldsymbol{\rho}) &= -0.5Z_s J_z(l') \\ &\quad -j\frac{k}{4}\int_c Z_s J_z(l')(\hat{n}' \cdot \frac{\boldsymbol{\rho} - \boldsymbol{\rho}'}{|\boldsymbol{\rho} - \boldsymbol{\rho}'|}) H_1^{(2)}(k|\boldsymbol{\rho} - \boldsymbol{\rho}'|)\,dl' \qquad (3.27) \\ &= -Z_s L_M[J_z(l')]. \end{aligned}$$

Finally the EFIE for impedance interface is written as

$$E_z^i(\vec{\rho}) = L_E[J_z(l')] - Z_s L_M[J_z(l')]. \tag{3.28}$$

The MFIE for the impedance boundary can be obtained by applying duality to (3.27) and again using (3.24), yielding

$$H_z^i(\vec{\rho}) = -L_M[J_z(l')] + \frac{Z_s}{\eta_0^2}L_E[J_z(l')] \tag{3.29}$$

The same numerical moment-method procedure as was used for PEC surfaces can now be applied to (3.28) or (3.29) to find the equivalent surface currents for the impedance surface. The scattered field is then found from (3.3) or (3.4).

Due to the practical computer limitations, the surface profiles modeled in the MM treatment must be truncated. These artificial edges introduced by the truncation leads to non-physical diffraction, which gives both unrealistic interactions between surface segments and unrealistically strong far-field diffraction. The tapered incident beam proposed by Thorsos [45] can only alleviate this problem at moderate incidence angles. In this approach, the angular distribution of the tapered incident field is described by an electromagnetically valid Gaussian weighting function. However, the tapered beam gives unrealistic surface illumination at high incidence angles unless the treated surface is very long [46]. Long surfaces are computationally expensive for standard MM, so a different approach introduced in the next section is used to avoid edge effects.

3.4.3 Hybrid MM/GTD Technique

The limitation of standard MM at very high incidence angles due to the artificial truncation of the surface can be avoid using the hybrid MM/GTD technique developed by Burnside *et al.* [26] and implemented for rough surface scattering by West [8]. A brief review of this approach follows. In this approach, the two-dimensional surface is extended to infinity as shown in Fig. 3.3. The dotted line shows the actual rough surface and the solid line shows the infinite planar extension. GTD is used to derive single basis functions that are used on the extensions at each end. In this way, the

artificial edge effects are avoided without seriously compromising the efficiency of MM. The extensions are angled to infinity so that all points on the extension are shadowed from the points on the actual surface, except for the intersection points B and C. Therefore, the field illuminated on the extensions can be described by the incident field plus the diffracted field from point B or C. All points on the extensions beyond point A or D (termed "GTD region" hereafter) are assumed to be sufficiently far from B or C so that the diffracted field in that region can be described by the GTD field, given by

$$F^d(\rho, \phi) = \hat{z} F_0 \frac{e^{-jk\rho}}{\sqrt{\rho}} f(\phi); \text{ within GTD region} \tag{3.30}$$

where F_0 is an unknown coefficient corresponding to the electric (HH polarization) or magnetic (VV polarization) field diffracted from point B or C, $f(\phi)$ is an arbitrary function that gives an angular dependence, and ρ is the distance from the diffraction point to the observation point in the GTD region. Since the surface is planar in the GTD region, the total field in the GTD region is given by the sum of the diffracted field (F^d) and the geometrical optics incident (F^i) plus reflected fields(F^r):

$$F^{total} = F^d + F^i + F^r. \tag{3.31}$$

The electric surface current on the extension can now be found by applying the surface boundary condition to (3.31), giving (assuming a perfectly conducting surface)

$$\mathbf{J_{GTD}} = \begin{cases} \mathbf{J_d} + \mathbf{J_{KA}}; & \text{within GTD region} \\ 0; & \text{otherwise} \end{cases} \tag{3.32}$$

where $\mathbf{J_d}$ is due to the diffracted field and $\mathbf{J_{KA}}$ is due to the incident plus reflected fields. They can be found by (3.30) and (3.1) as

$$\mathbf{J_d} = \begin{cases} \hat{l} J_0 \frac{e^{-jk\rho}}{\sqrt{\rho}}; & \text{VV polarization} \\ \hat{z} J_0 \frac{e^{-jk\rho}}{\sqrt{\rho^3}}; & \text{HH polarization} \end{cases} \tag{3.33}$$

$$\mathbf{J_{KA}} = 2\hat{n} \times \mathbf{H^i},$$

34
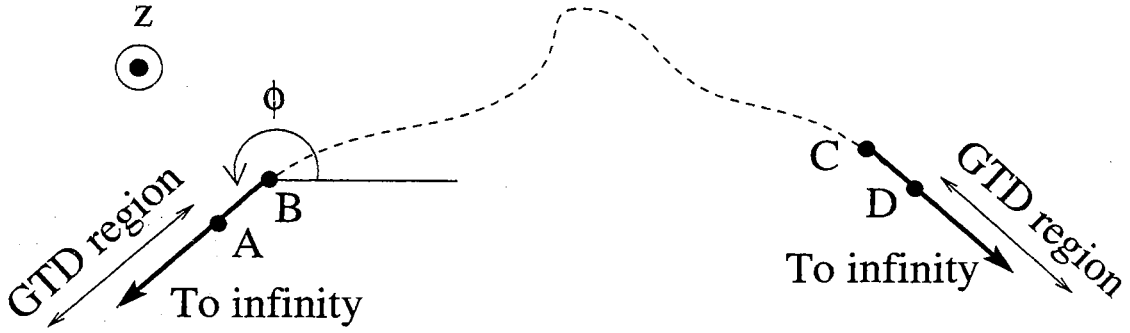
Figure 3.3: Extensions for MM/GTD technique

where J_0 is the unknown coefficient associated with the single basis function in the GTD region to be found using the moment method and $\mathbf{H}^i$ is the incident magnetic field. The surface current between point A and D (the "MM region") is expanded using standard MM pulse basis functions. The expansion of the total surface current can be expressed as

$$
\mathbf{J_s} = \begin{cases} \mathbf{J_{MM}} = \hat{\mathbf{i}} \sum_{n=1}^{N} a_n f_n(l), & \hat{\mathbf{i}} = \hat{z} \, or \, \hat{\mathbf{l}}; \quad \text{MM region} \\ \mathbf{J_{GTD}} = \mathbf{J_d} + \mathbf{J_{KA}}; & \text{GTD region} \end{cases}
\tag{3.34}
$$

Note that the entire unknown current in the GTD region is represented by a single basis function. By substituting this current into the EFIE or MFIE ((3.14) or (3.16)) and follow the same numerical technique, the surface current can be found. The scattered field is again found from the far-field radiation of the current (using (3.3) or (3.4)).

3.4.4   Hybrid MM/GTD for Sea Water

The hybrid MM/GTD approach can also be used to find the equivalent surface current on finite conductivity boundary. The only modification needed is that the Kirchhoff approximation in the GTD regions are replaced by equation (3.1) and the appropriate impedance boundary field integral equation (3.28) or (3.29) are treated.

Chapter 4

NUMERICAL SCATTERING CALCULATIONS

The backscatter from the time histories of two spilling breaking waves found using MM/GTD numerically technique is presented here. These two series of surface profiles are extracted from the video snapshots of spilling breaking waves, which were mechanically generated in a water tank. The time histories were provided by professor James H. Duncan of the University of Maryland Department of Mechanical Engineering.

The time history of the high incidence angle backscattering cross-section of the waves are first presented. The frequencies considered are 10 GHz and 20GHz, with the look direction upwind at an 80° incidence angle. The time dependence of the Doppler shift of the backscatter is then examined. This is used to identify the surface features responsible for the scattering at different times. The goal of this analysis is to identify possible scattering features and mechanisms that lead to "fast" and "slow" scattering. Finally, the front faces of one wave profile history are artificially extended to introduced super events, and to demonstrate the effects of these events on the Doppler shift.

4.1 Descriptions of Water Surface Data

The time histories of two spilling breakers are treated in this work. They were mechanically generated by a vertical oscillating wedge in a 14.8 m long, 1.22 m wide and 1.0 m deep water tank without any wind blowing. A video camera was mounted on a carriage which moves along the tank at the same speed as the phase velocity of the breaking wave, aligned with the wave crest. Two light-emitting diodes were attached to the carriage, which illuminated fluorescent dye on the surface that was imaged. Each surface profile in the time history was detected from a single video frame. The video camera viewed the wave propagation from the side, looking down at 5° from horizontal. The camera operated at a sampling frequency of 472 frames/second. The full description of the water tank and experiment procedure is given by Duncan *et al.* [30].

The time history of the first wave to be examined is shown in Fig. 4.1. This figure was formed by stacking 329 individual profiles vertically, giving an increasing time in the vertical axis. Some individual surfaces are plotted in Fig. 4.2. Since the camera was moving at the long wave phase velocity, a surface feature shifting toward left or right with increasing time indicates that it is moving faster or slower than the camera. For example, there is a feature at $x = 40$ mm at 400 ms that is moving faster than the wave crest, and other features that are left behind after 350 ms. These waves were generated with a clean water surface, so this time history is termed "clean". The measured surface profiles are 117 mm in length, which is sufficient to give a clear view of the temporal evolution of the crest. The complete data set lasts 697 ms. The initial crest height is 29 mm, and the maximum height reaches 35 mm at 190 ms. A plume starts to appear at 210 ms. Some parasitic capillary waves of approximately 5 mm wavelength are formed just below the "toe" of the plume from 210ms to 310 ms. This wave breaks at 370 ms. After breaking, the plume collapses and turbulent
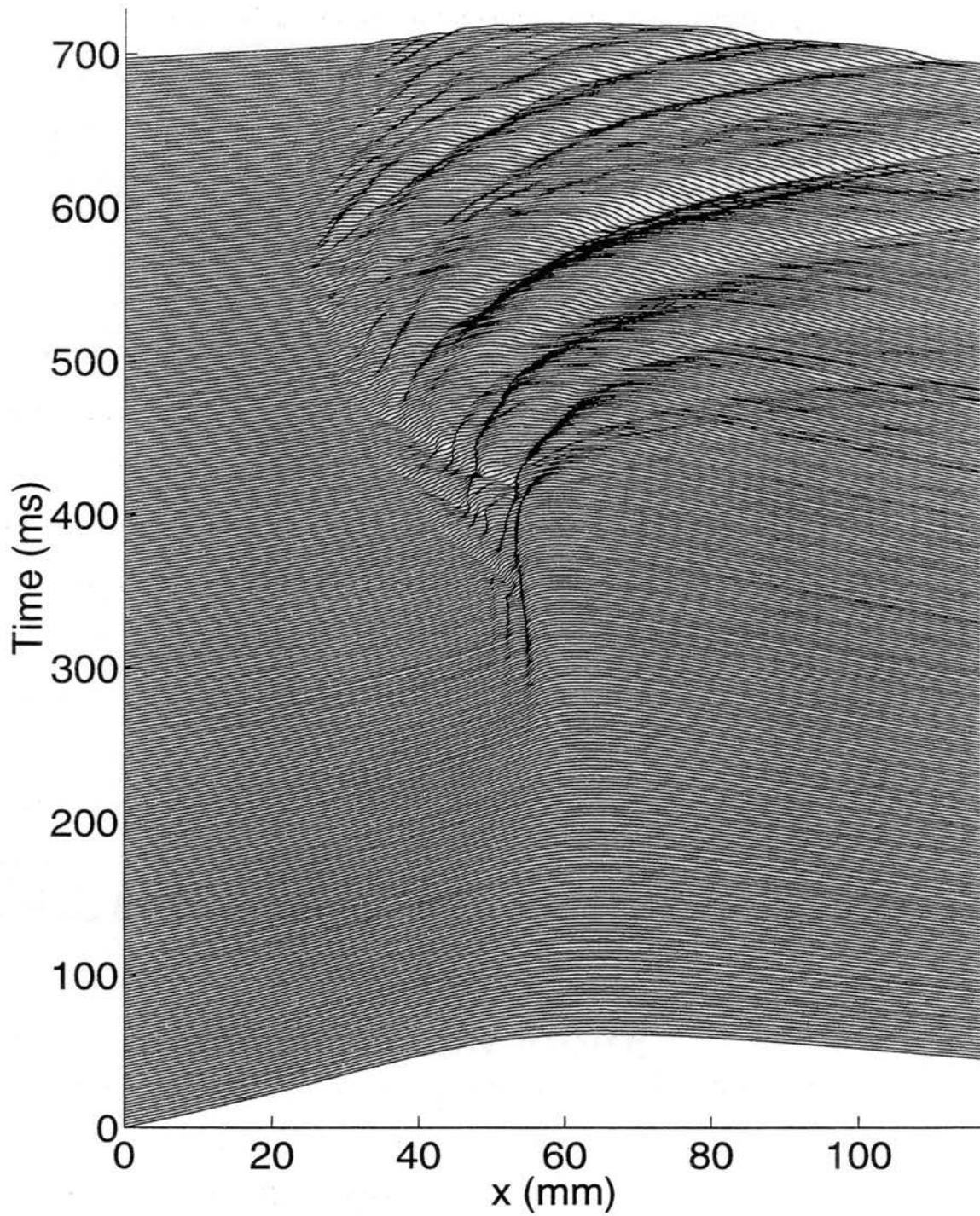
Figure 4.1: Time history plot of the "clean" waves.

regions are generated on the front face of the wave. The turbulence is carried by the orbital motion of the long wave, so is passed by the wave crest. New turbulent regions then form continuously. There are also features moving faster than the gravity wave that present on the front face after wave breaking.

The second wave time-history to be considered was generated under similar conditions as the "clean" wave, except that liquid soap was added to the water surface to act as a surfactant. This wave is therefore termed "surfactant", and is shown in Fig. 4.3. Again, some individual profiles are plotted in Fig. 4.4. The total time of this data set is 803 ms. The surfactant dramatically reduces the surface tension of the water, affecting the breaking process throughout. Surface tension is much less an important restoring force with larger waves that appear in the open ocean, so this case may be more representative of large-scale breaking in the open sea. The crest height of the "surfactant" wave starts at about 31 mm and reaches the maximum of 40 mm at 300 ms. The plume formation begins at 310 ms, and builds up until 400 ms. No parasitic capillaries form on the front face during this time, and the front face is steeper than in the clean case. After the initial breaking the features on the front face appear to be more chaotic than those in the "clean" data set. Also, additional micro-breaking events occur after the initial breaking, one at 560 ms and another is at 740 ms. The last breaking event is much lower magnitude than the previous two. After the initial breaking a steep surface feature forms that moves at the phase velocity of the long wave, and eventually causes the second breaking at 560 ms. A feature that moves faster than the wave phase velocity again appears on the front face of the wave after the second breaking. Turbulent regions are continuously shed from the crest after the initial breaking.
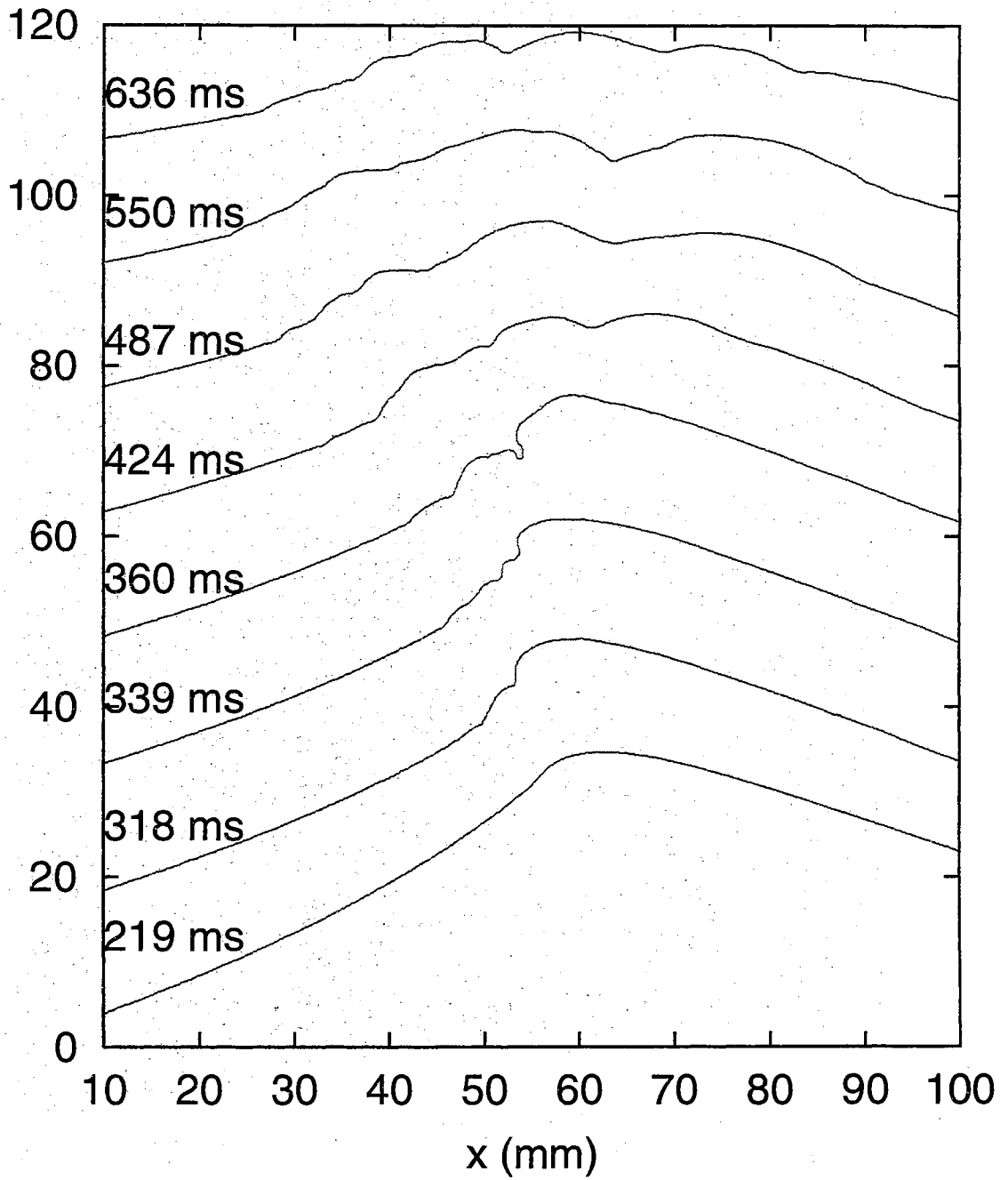
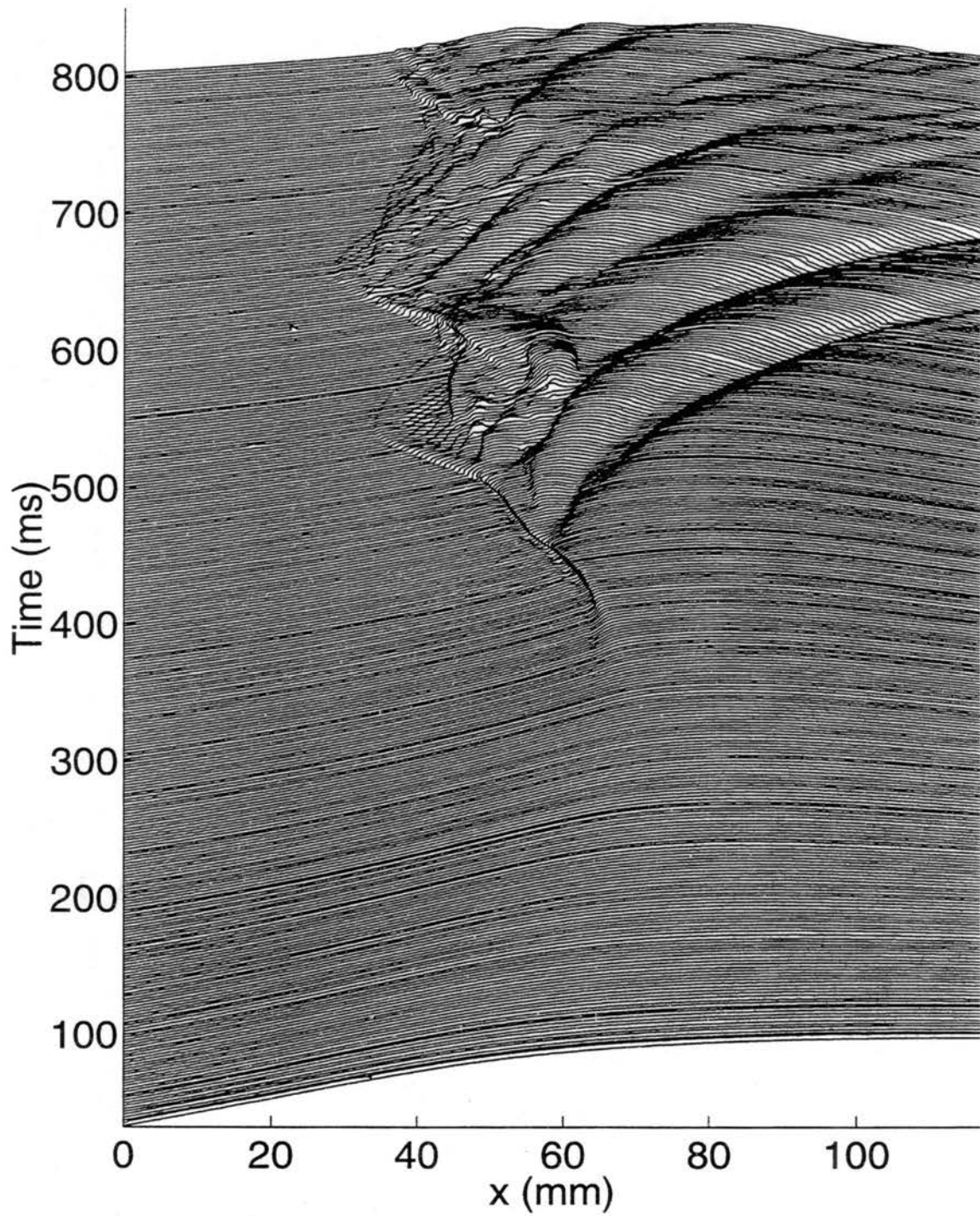Figure 4.2: Some individual surface profiles of "clean" waves.

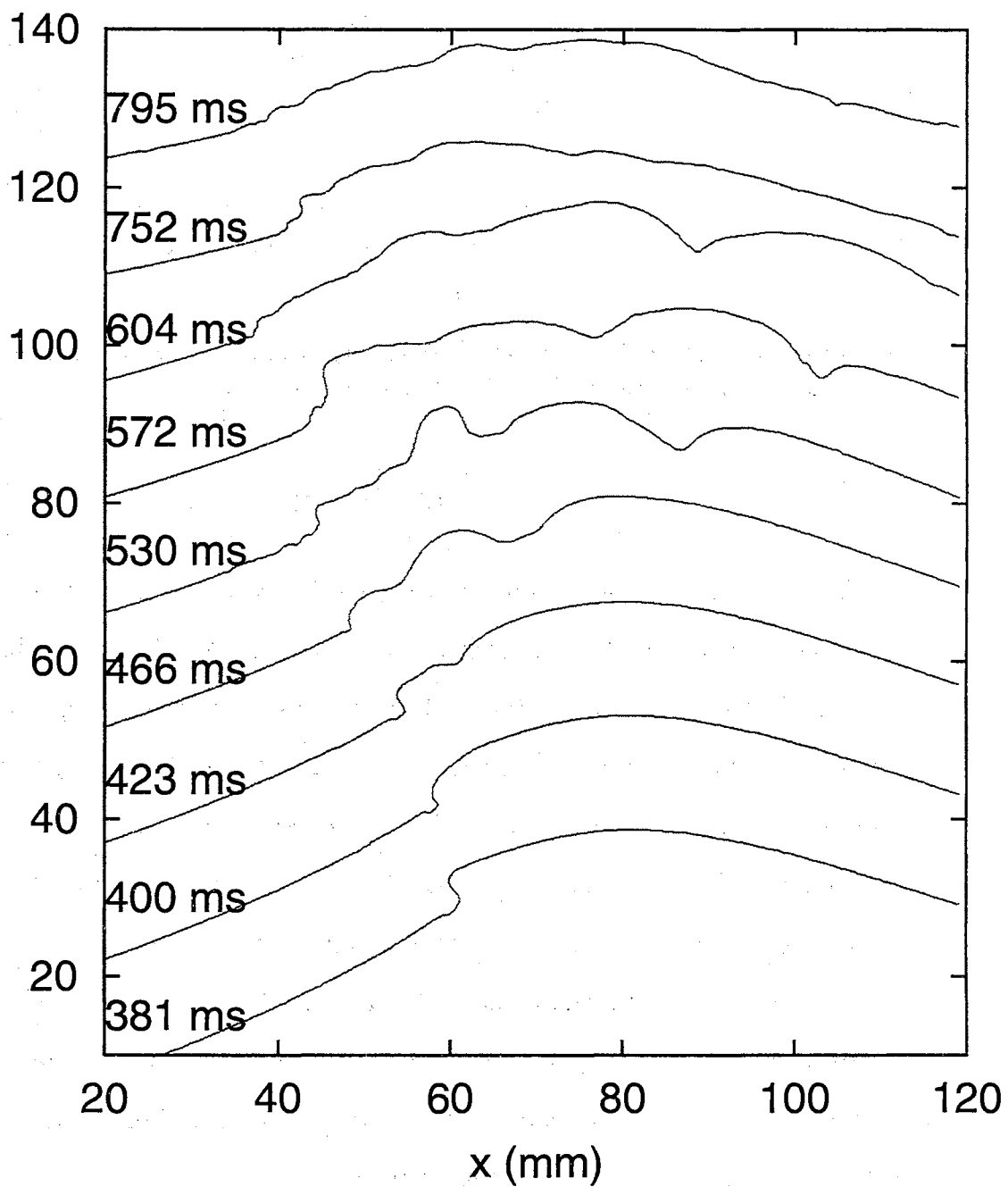Figure 4.3: Time history of the "surfactant" waves.

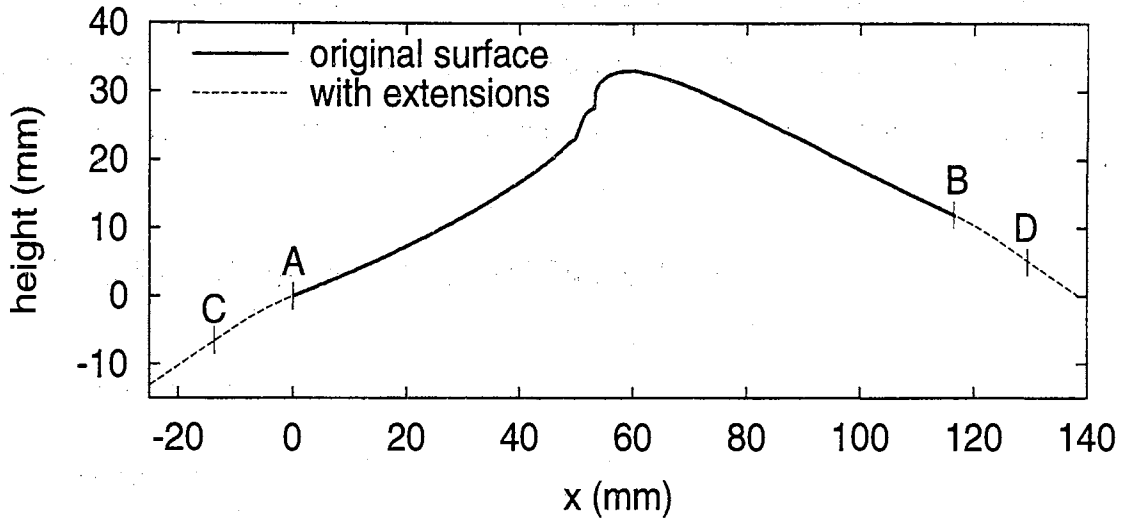Figure 4.4: Some individual surface profiles of "surfactant" waves.

Figure 4.5: Example of surface extensions used with MM/GTD numerical technique. Points A and B are the diffraction points, and the GTD regions begin a half wavelength from points C and D.

4.2 Simulation Parameters

The electromagnetic backscatter from the individual wave surface was found using the hybrid MM/GTD technique described in chapter 3. Each surface profile was resampled to equal step sizes in the arc-length direction before computation. Thirty-three moment method sub-domain basis functions were used per radar wavelength to describe the surface currents. Both ends of the surface profiles were extended to infinity to avoid edge effects and allow the use of the numerical technique. One example of the surface extension is plotted in Fig. 4.5. The radius-of-curvatures of the curved sections (curve "A-C", and "B-D") which connect the actual surface section to the infinite planar extensions are two radar wavelengths. The planar extensions are angled at 30° to horizontal. The GTD basis functions used to describe surface currents on the extensions begin a half wavelength from the diffraction point (marked by "C" and "D").

The backscattered fields from the individual profiles were found to yield a continuous time history. The phase of the backscatter was maintained to allow the calcula-

43

tion of the Doppler shift, as described later. The analysis focuses on upwind-looking backscattering since that is the orientation that gives sea spikes, super events, and fast Doppler scattering. However, sample downwind-looking scattering is also shown.

4.3 Backscattering from "Clean" Wave

4.3.1 10 GHz Response

Amplitude history

The time history of the backscattering cross-section from the "clean" wave is shown in Fig. 4.6, which shows the one-dimensional backscattering cross-section in dB relative to one meter (dB-m). The numerical calculations were performed at 10GHz with an incidence angle of 80° from the left (corresponding to an upwind-looking direction). The time history of backscatter can be roughly separated into three stages. The first stage occurs before 150 ms. At this time, the wave crest is round and there is little distributed surface roughness. The backscatter at this time is quite low, and therefore subject to numerical errors in the MM/GTD technique [27]. This is not realistic representation of open sea conditions since wind-generated roughness would appear in this case. The backscatter at this stage is therefore not considered further. The second stage begins at 150 ms. The signal strength starts rising at this time and keeps increasing until it reaches a maximum at 300 ms in both polarizations. This stage corresponds to the time where the gravity wave is steepening and a plume is forming, and ends when the plume collapses at 370 ms. The third stage is characterized by rapidly changing backscatter at later than 370 ms. At this time, the plume has collapsed and turbulent regions are continuously generated from the front face of the long wave. Distributed roughness due to these turbulent regions eventually covers the entire measured portion of the back face of the wave.
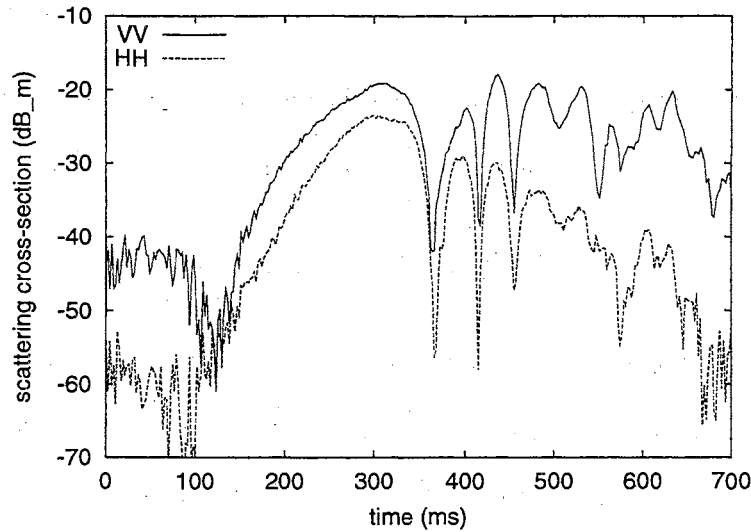
Figure 4.6: Time history of the backscattering cross-section of the "clean" wave at 10 GHz and nominal 80° incidence when looking upwind. Both VV and HH responses are shown.

The HH backscattering is weaker than that at VV at all times in Fig. 4.6. Super events have therefore not been observed. During the second stage, the difference of the backscattering coefficient in both polarization is almost constant at about 5 dB. However, the HH/VV ratios continuously decreases during the third stage. While the relative maxima (local peaks) in the third stage are approximately the same magnitude at VV, the peak strength of HH continuously drops.

The increasing signal during the second scattering stage is correlated with the formation of the plume structure before breaking, suggesting that the plume is responsible for this scattering. The third stage scattering on the other hand appears to correspond to the turbulent structures. The rapid changes in the positions and magnitudes of turbulent cells are likely responsible for the rapid fluctuations in the scattering.

45

Doppler shift history

Doppler history of the backscatter was found using the time-dependent Fourier transform approach, also referred to as short-time Fourier transform, described by [47]

$$X[n, f] = \sum_{m=-L/2}^{L/2} x[n+m]w[m]\exp[-j2\pi fm] \tag{4.1}$$

where x is the backscattered signal, w is a window sequence with length L, and f is the frequency. The short-time Fourier transform $X[n, f]$ is the spectrum of the backscatter at time $t = n\Delta t$ where Δt is the time interval between each surface. The complete time history was divided into sub-domains using a Hamming weighting window. An FFT was then used to find the Doppler spectrum within each sub-domain. The entire sub-domain extended for 106 ms (50 individual profiles), and adjacent sub-domains over lapped for 80% of their entire duration. Two adjacent sub-domain weightings are shown in Fig. 4.7. The Hamming weighting window used is

$$w(m) = \begin{cases} 0.54 - 0.46 * \cos[\frac{2\pi}{50}(m+25)], & -25 \leq m \leq 25 \\ 0, & otherwise \end{cases} \tag{4.2}$$

This minimizes the sidelobes in the Doppler spectra.

There is a trade-off when choosing the duration of the sub-domains. Longer sub-domains give a better frequency resolution at the expense of time resolution. The 106 ms hamming window gives a mainlobe bandwidth of approximation 9 Hz and sidelobes of about $-50\,$dB in strength, which has good balance in both time and frequency resolution.

The motion of the camera must be compensated when the Doppler frequencies are found. This was accomplished by first multiplying the scattering from the individual profiles by
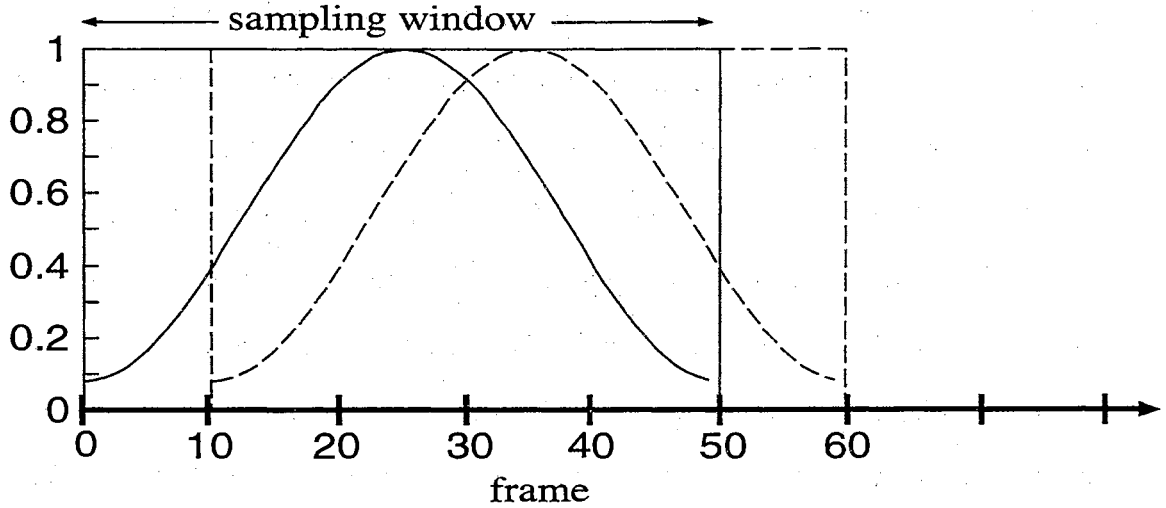
Figure 4.7: Windowing function for the short-time Fourier transform.

$$p(t) = \exp[j\, 2k\, v_c\, t\, \sin(\theta_i)] \qquad (4.3)$$

where v_c is the camera velocity, θ_i is the incidence angle, and t is the time of the profile sampling. This adds a phase shift equal to that introduced by the reduction in round-trip distance due to the camera motion.

The time history of the Doppler shift corresponding to the backscatter in Fig. 4.6 is shown in Fig. 4.8. The Doppler frequency is related to the scatterer motion by

$$f = \frac{2\, v_r}{\lambda} \qquad (4.4)$$

where f is the Doppler frequency, v_r is the component of the scatter velocity in the backscatter direction (i.e. the radial velocity), and λ is the microwave frequency. The signal strengths in the plots are normalized to the maximum magnitude of that polarization. Each plot in Fig. 4.8 shows both the contour plot of the complete Doppler spectrum as well as the trails of the local magnitude peaks. The contours are spaced by 2 dB increments in magnitude, and the relative magnitudes of the peak trails are colored according to the gray-scale bar below the plot.

The VV Doppler history in part (a) of the figure shows that the strongest backscat-

47

tering occurs at two different scatterer speeds. The higher-speed shift is at 64 Hz, peaking at 300 ms, and the slower is at 48 Hz, peaking at 480 ms. Comparing with the amplitude history shows that the faster speed corresponds to the second scattering stage where the wave is steepening and the plume is forming. The 62 Hz Doppler shift is approximately that expected for a scatterer traveling at the phase velocity of wave. The slower speed appears immediately after the plume breaks and corresponds to the third scattering stage. Lee *et al.* [1] used the terms "fast" and "slow" scattering to distinguish these two types of responses, and this naming convention is used here. The faster 64 Hz signal is the fast scattering while the 48 Hz response is the slow scattering. The fast scattering shows an abrupt cut-off at about 380 ms, and immediately after that the slow signal appears. This time corresponds to the actual wave breaking. After breaking, both the previously mentioned slow scattering at 48 Hz appears, as well as a much faster, low magnitude scattering at 72 Hz. A slower scattering at 40 Hz appears at 600 ms.

The HH Doppler history for the clean wave is shown in part (b) of the Fig. 4.8. The strongest scattering again appears at 64 Hz and 300 ms. The later slow scattering is much lower in magnitude relative to the fast scattering peak at this polarization, and the slowest scattering at 40 Hz does not appear above the −14 dB limit of the plot. The very fast signal at 72 Hz also does not appear.

Short arrows have been added to the surface time history plot in Fig. 4.1 to show the propagations of surface features relative to the camera motion (Fig. 4.9). The slopes of the short arrows give the feature velocities relative to the camera velocity, which can be matched to the Doppler shift occurring at the same time. Specific surface features can therefore be related to specific responses.

The first arrow appears from 200 ms to 225 ms, and shows the movement of the unbroken crest. The velocity is 945 mm/s, the phase velocity of the wave, which
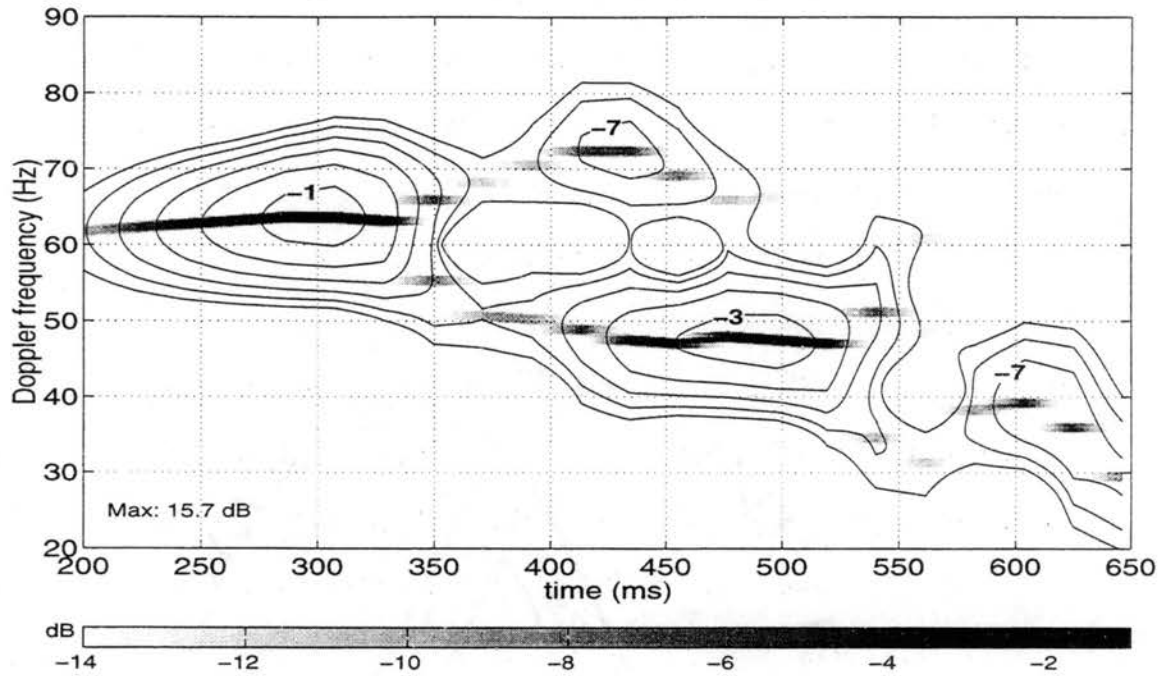
(a) VV
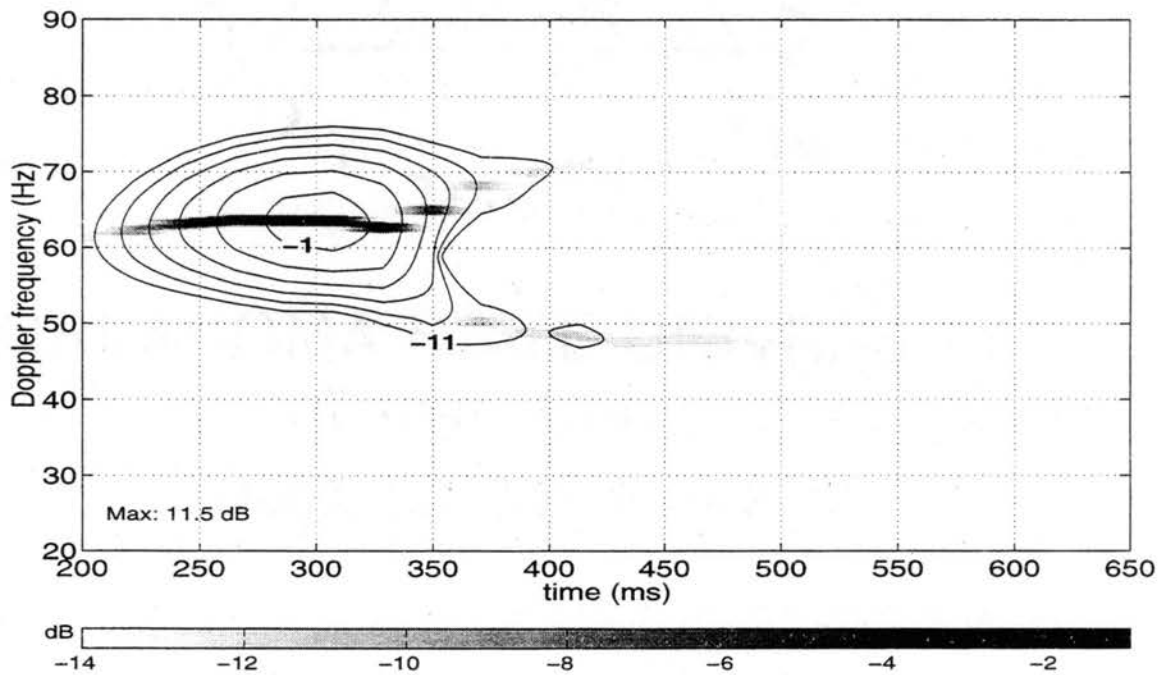
(b) HH

Figure 4.8: Time history of Doppler shift of "clean" wave at 80° incidence and 10 GHz when looking upwind.

49

corresponds to a Doppler shift of 62 Hz at 80° incidence. The second arrow extends from 275 ms to 325ms, and indicates that the plume slightly outruns the gravity wave and causes wave breaking. The corresponding Doppler shift is 64 Hz. This agrees with Lee's observation [2] that the Doppler shift of the fast signal is slightly higher than the frequency of the phase velocity of the gravity wave. The third arrow corresponds to a feature that moves faster than the phase velocity from 400 ms to 450 ms. The corresponding Doppler shift is 72.5 Hz. The fourth through seventh arrow from 350 ms to 530 ms indicate four turbulent regions generated on the front face after breaking that are carried by the orbital motion of the wave. The orbital motion is much slower than the phase velocity at this point so the regions move to the back face of the wave with increasing time. The motions of those features produce a strong Doppler shift at about 48 Hz and last from 350 ms to 530 ms in both VV and HH spectra. The eighth arrow will be discussed later. The ninth arrow shows a turbulent region that is moving at a speed corresponding to a 40 Hz shift.

The correlation between the feature speeds and the Doppler shifts at a particular time shows that roughness behind the wave crest does not contribute significantly to the total scattering. For example, the eighth arrow shows that the turbulent region that gave a 48 Hz shift at earlier time (the seventh arrow) has slowed dramatically and moved to the back face. This motion is matched only by a very weak response in Fig. 4.9 at 32 Hz. This can be further demonstrated by modifying the surface at 477 ms to remove the back face roughness and repeating the numerical calculations, as shown in Fig. 4.10(a). Part (b) of the figure shows the calculated scattering from this surface as a function of incidence angle. The surface modification introduced a change in the backscattering of less than 0.5 dB at 80° incidence.

Note that as the wave sheds energy the crest becomes less steep and the back-face shadowing is less server. Features further back on the wave profiles are therefore more
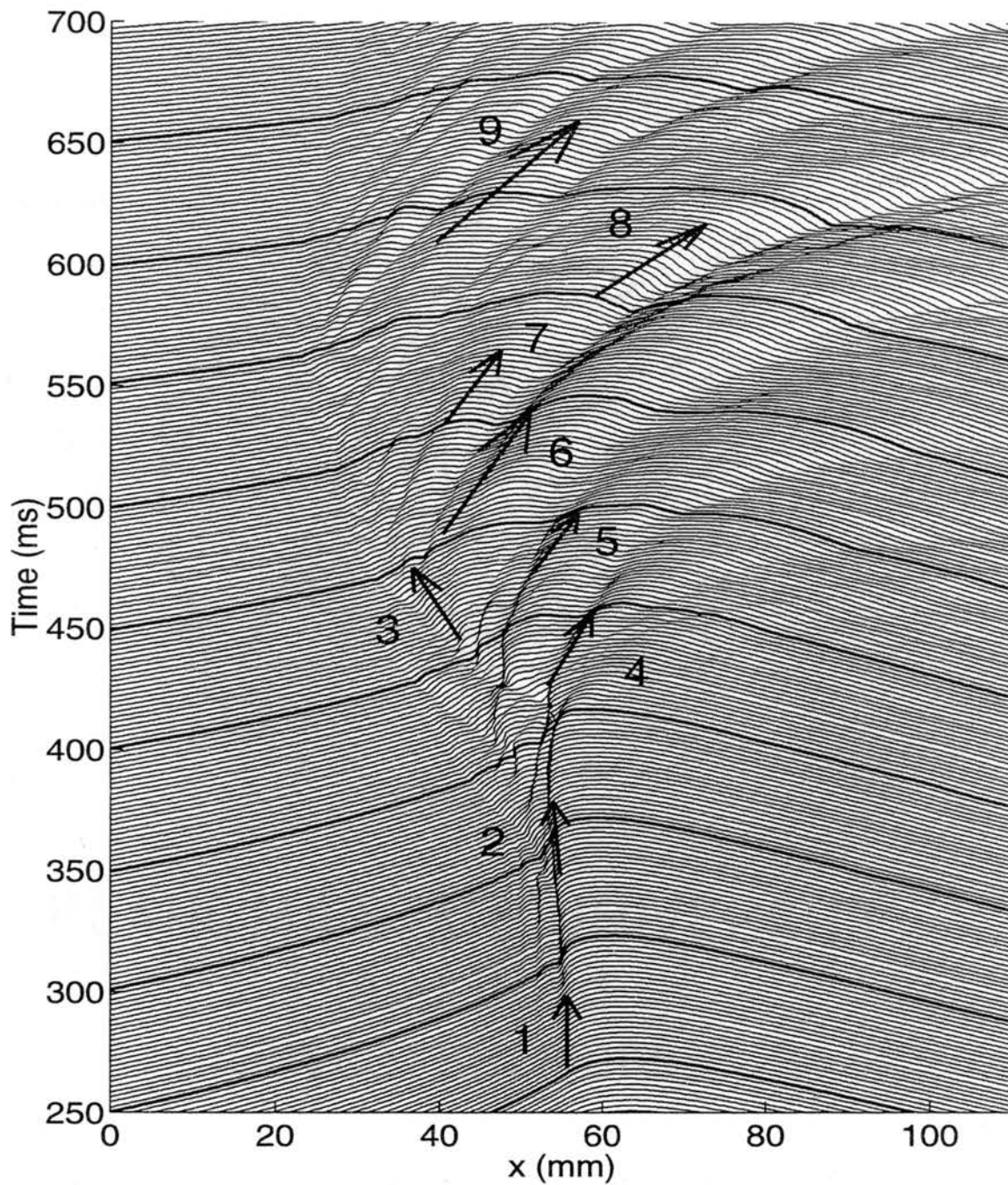
Figure 4.9: Time history of the "clean" wave with surface feature motion corresponding to the 10 GHz upwind response identified.

important at later times. Their speeds can be matched to the lower Doppler shifts of about 30 ∼ 40 Hz near the end of the time history.

4.3.2   20 GHz Response

The numerical calculations were repeated at an operating frequency of 20 GHz. The amplitude response is shown in Fig. 4.11. The response is similar to the 10 GHz response overall, but there are some significant differences. The most obvious difference is that the HH backscatter is equal to VV at 300 ms. This is the point where the wave plume is fully defined before breaking. The HH/VV ratio remains at approximately 0 dB until 360 ms. Steep features occur on the front face during this time. This will be discussed in detail in section 4.5.2. Another difference is that the scattering oscillates more rapidly after 380 ms and the decreasing of the HH signal strength at later time is less smooth.

The Doppler shifts of the 20 GHz response are shown in Fig. 4.12. The first strong response appears at approximately 128 Hz and peaks at 280 ms. This corresponds to the formation of the plume, giving a speed slightly faster than the wave phase velocity which has a Doppler shift at 124 Hz. The scattering immediately after breaking gives a Doppler shift of about 118 Hz. This is much stronger scatter than appeared at the same time at 10 GHz. The fastest scattering centered at 415 ms remains strong for a longer time, but the first slow response centered at 480 ms is much weaker at 20 GHz. These differences appear since the smaller wavelength responds to different surface features.

As before, some short arrows have been added to surface profile history to indicate the motions of possible scatterers. The first arrow shows the plume immediately before breaking. The second through fourth arrows show features moving slightly slower than the phase velocity, giving a shift just below 120 Hz from 320 ms to 420

52
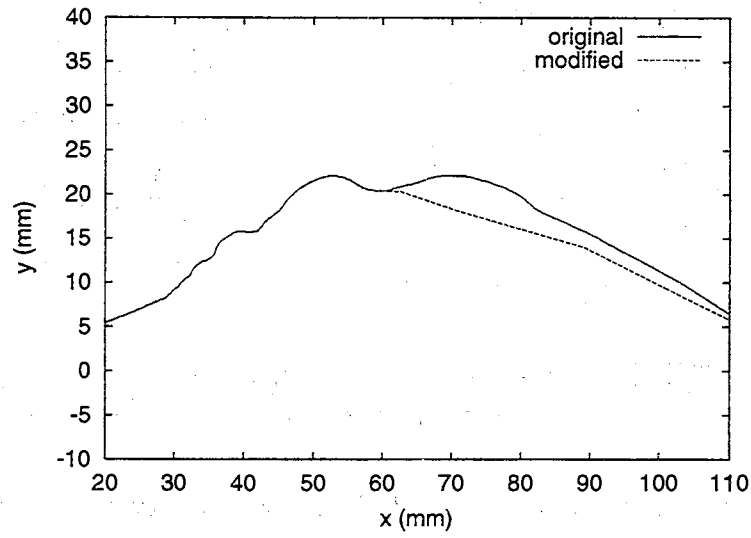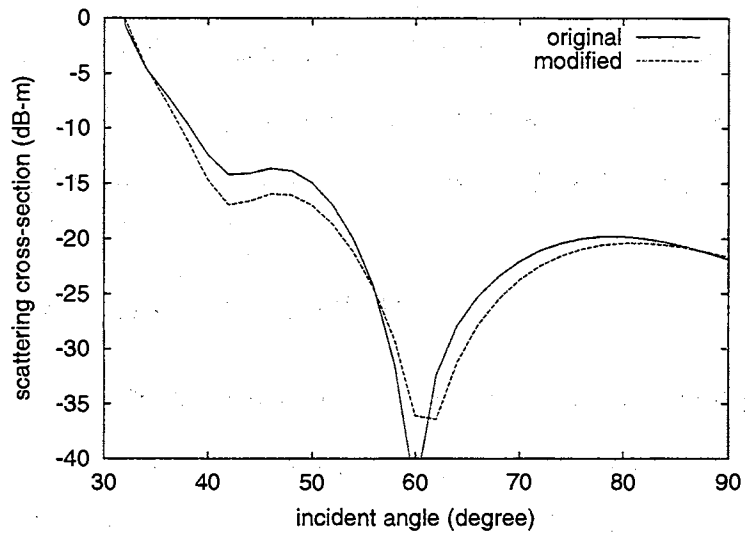
Figure 4.10: (a) Modification of "clean" wave surface at 477 ms, and (b) backscatter comparison from original and modified surface.
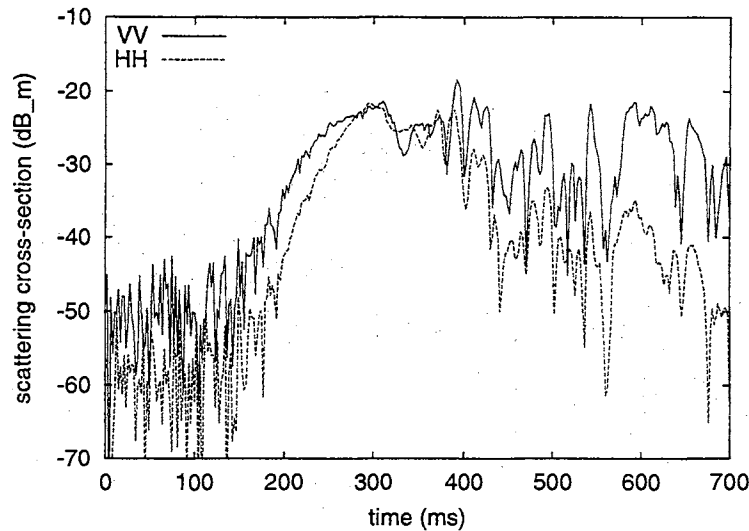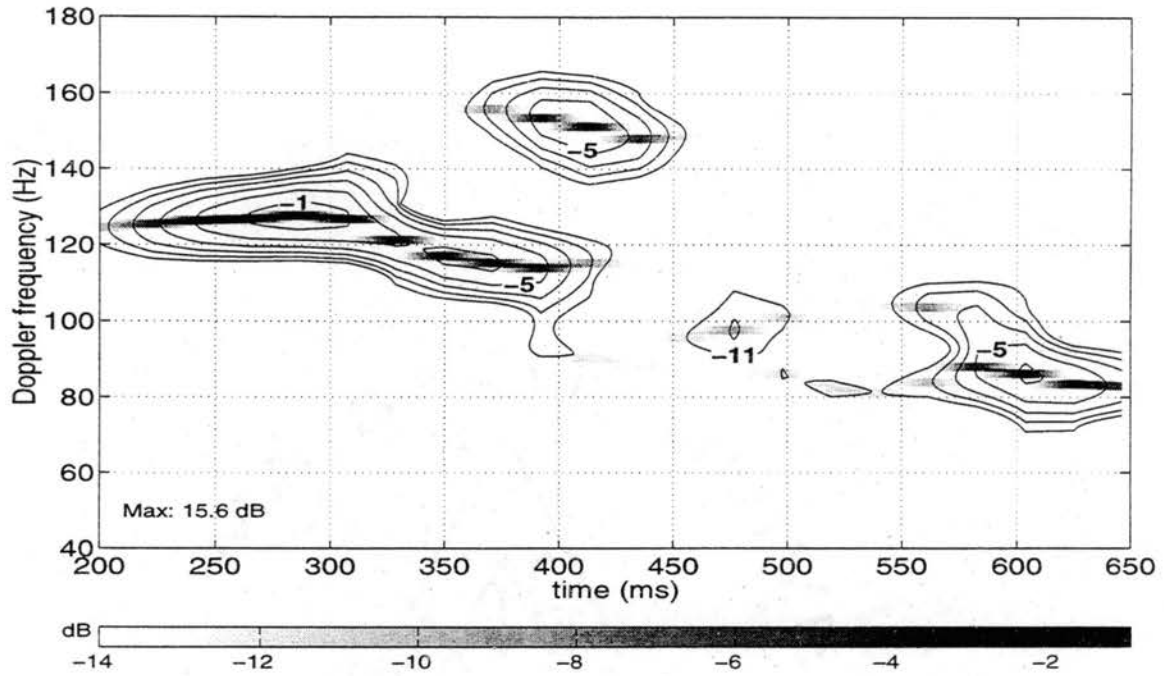
Figure 4.11: Time history of the backscattering cross-section of the "clean" wave at 20 GHz and nominal 80° incidence when looking upwind.

ms. The two arrows at about 370 ms and 420 ms show features moving faster than the phase velocity that give the shift at about 150 Hz. Although surface roughness is clearly evident on the front face from 450 ms to 550 ms there is no significant response in the Doppler response at this time. The analysis in Sec. 4.5.1 will show that the surface lacks energy at the Bragg-resonant wave number at this time and causes a weak responses here. Roughness that is resonant at 10 GHz does appear however.

4.3.3 Down-wind Looking Results

The backscattering calculations were also performed with the electromagnetic energy looking in the direction of the wave propagation (downwind looking). The incidence angle was again 80°. The calculated scattering at 10 GHz is shown in Fig. 4.14. Under these conditions the plume on the front face of the wave is shadowed. ("Front" and "back" faces are still defined in terms of the wave propagation direction, not the radar look direction.) The scattering prior to breaking is therefore quite small. The scattering rises significantly after 400 ms. At this time turbulent regions resulting from breaking have moved to the back face of the wave and are illuminated. VV

54

(a) VV
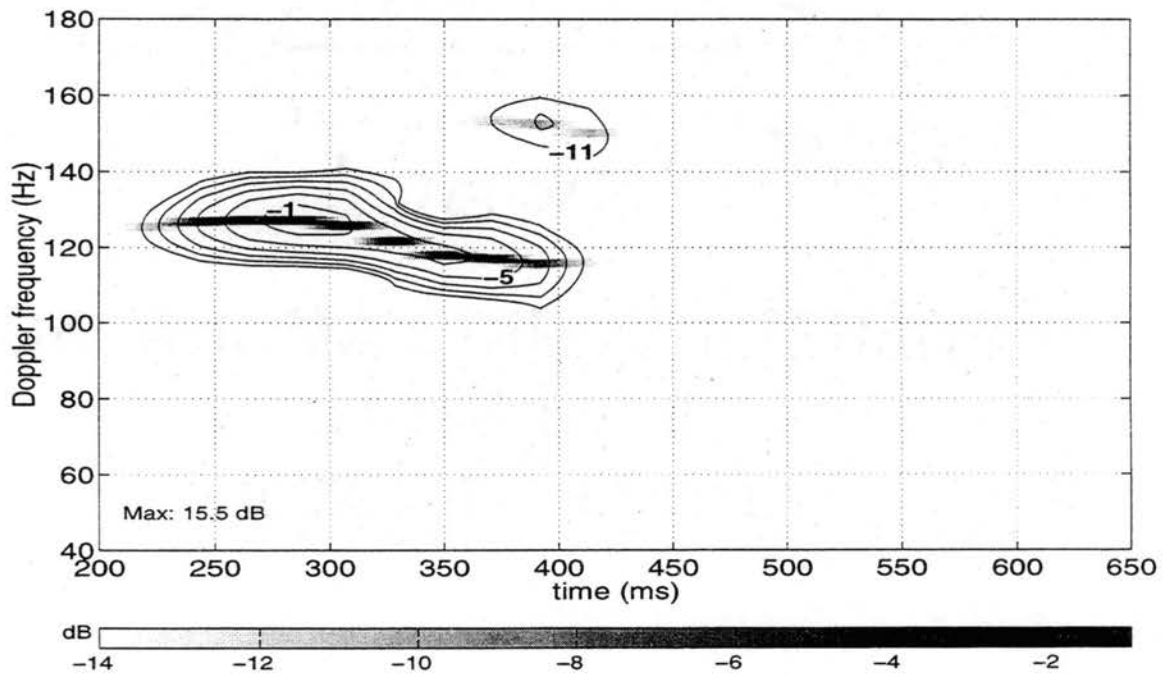
(b) HH

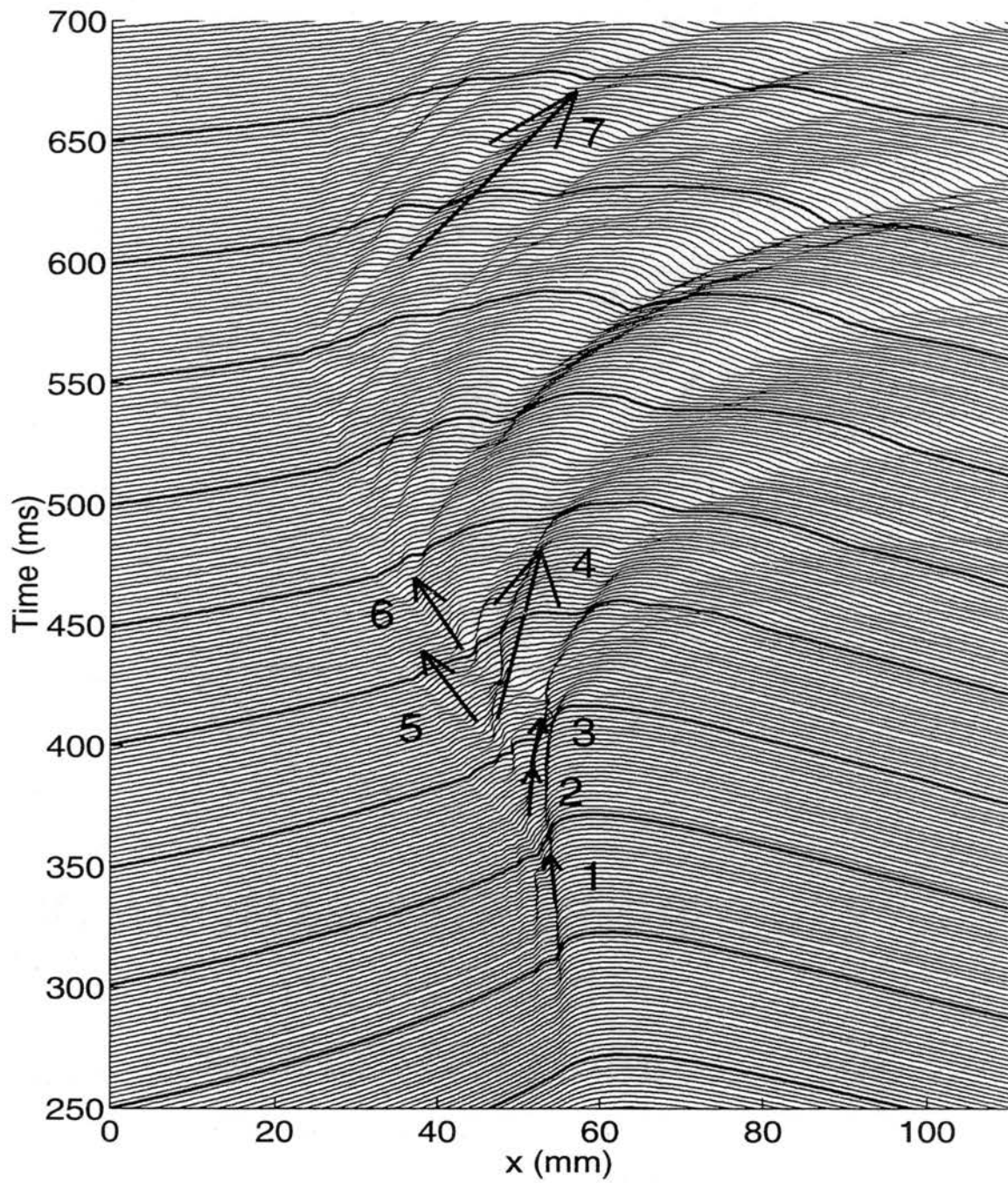Figure 4.12: Time history of Doppler shift of the "clean" waves at 80° incidence and 20 GHz when looking upwind.

Figure 4.13: Time history of the "clean" wave with surface feature motion corresponding to the 20 GHz upwind response identified.
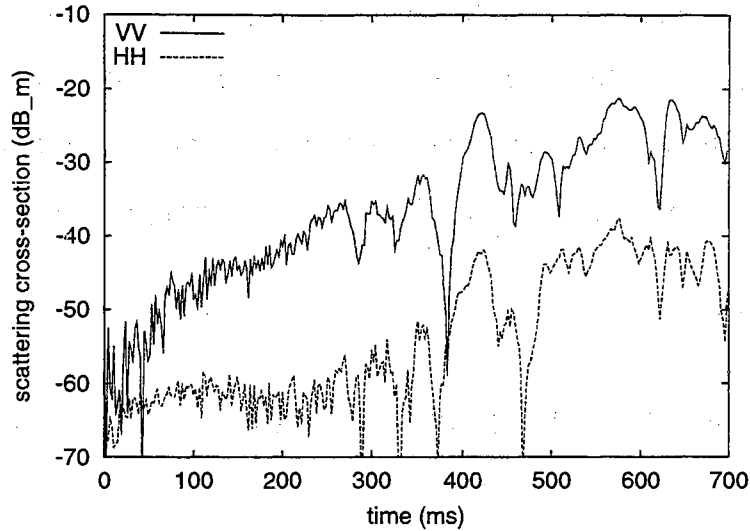
Figure 4.14: Time history of the backscattering cross-section of "clean" wave at 10 GHz and nominal 80° incidence when looking downwind.

backscattering exceeds HH at all time, which is consistent with the predictions of Bragg-scattering theory.

The Doppler history of the scatter is shown in Fig. 4.15. (Note that the wave is now moving away from the radar so the Doppler shifts are now negative.) The first response is a weak signal at −45 Hz and 420 ms. This correlates with the 45 Hz response that appears in the upwind look response at the same time. However, the responsible feature is on the front face and therefore partially shadowed, so the response is much weaker. The strongest scattering appears at −30 Hz when a large turbulent region moves on the back face. Near the end of the time history a Doppler shifts as low as −20 Hz appears. This slow speed corresponds to the orbital velocity well behind the crest. This response is not matched by a response at approximately +20 Hz in the upwind looking response, further demonstrating that the shadowed roughness does not significantly contribute to the backscattering. This is also supported by the strong response in the period from 500 to 600 ms when very little scattering in the upwind looking results.

Scatterer motions that correspond to observed Doppler shifts are marked in Fig.

4.16. The features identified differ significantly from those when looking upwind due to the shadowing effects. The first four arrows correspond to shifts of $-45\,$Hz, $-30\,$Hz, $-30\,$Hz, and $-20\,$Hz in chronological order. The fifth arrow shows a scatterer moving from front face to back face giving strong Doppler response at $-38\,$Hz in the VV spectrum but not in the HH spectrum.

## 4.4 Backscatter from the "Surfactant" Waves

4.4.1 10 GHz Response

The time history of the backscattering from the "surfactant" data set is shown in Fig. 4.17. The incidence angle was again 80° and the look direction was upwind. The signal strength increases smoothly prior to breaking as in the clean case. The HH response is approximately 5 dB below that at VV in this period. After the initial breaking at 400 ms the response is somewhat different in that the average HH scattering remains approximately constant until about 570 ms (although the signal oscillates through this time). Inspection of the surface profiles shows that very steep features appear on the wave throughout this period, with a small overturning at 570 ms. No super events appear in this response.

The Doppler shift of the scattering from the surfactant waves is shown in Fig. 4.18. There are four distinct regions of very strong scattering in the VV response. The first maximizes at about 70 Hz and 380 ms. This corresponds to the time when the crest steepens and a small jet forms prior to breaking. From 270 ms to 370 ms, the speed of this response continually increases until a Doppler shift of 70 Hz is reached. This is much higher than that expected from the wave phase velocity (62 Hz). The wave breaks immediately after this time. The larger speed difference between the plume and the gravity wave may indicates that the "surfactant" wave

58
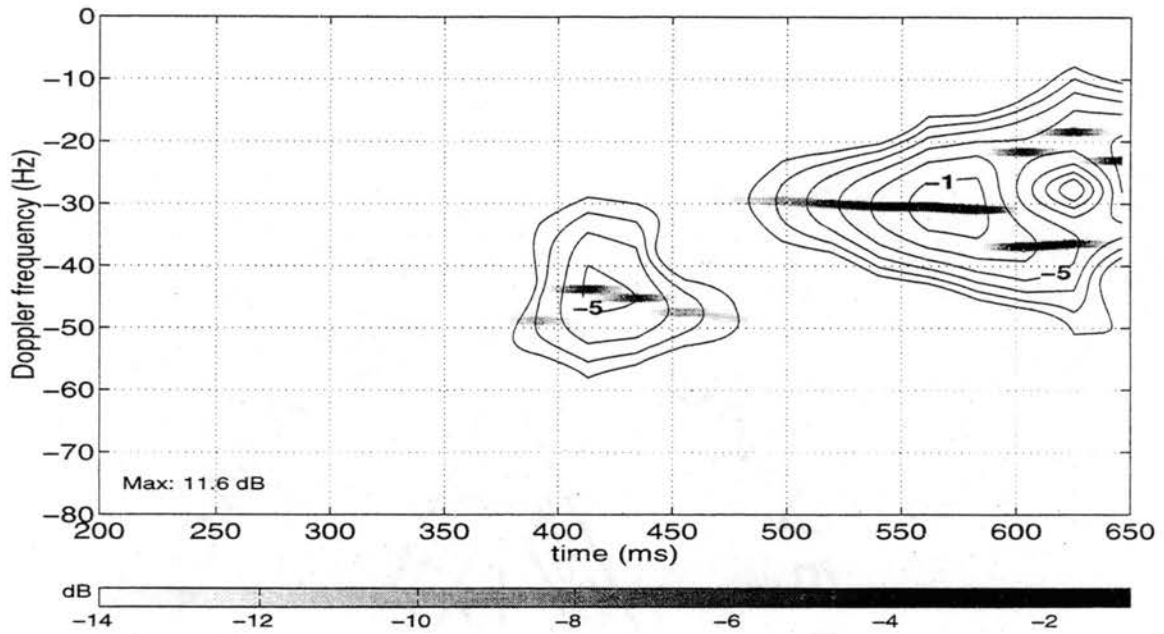
(a) VV
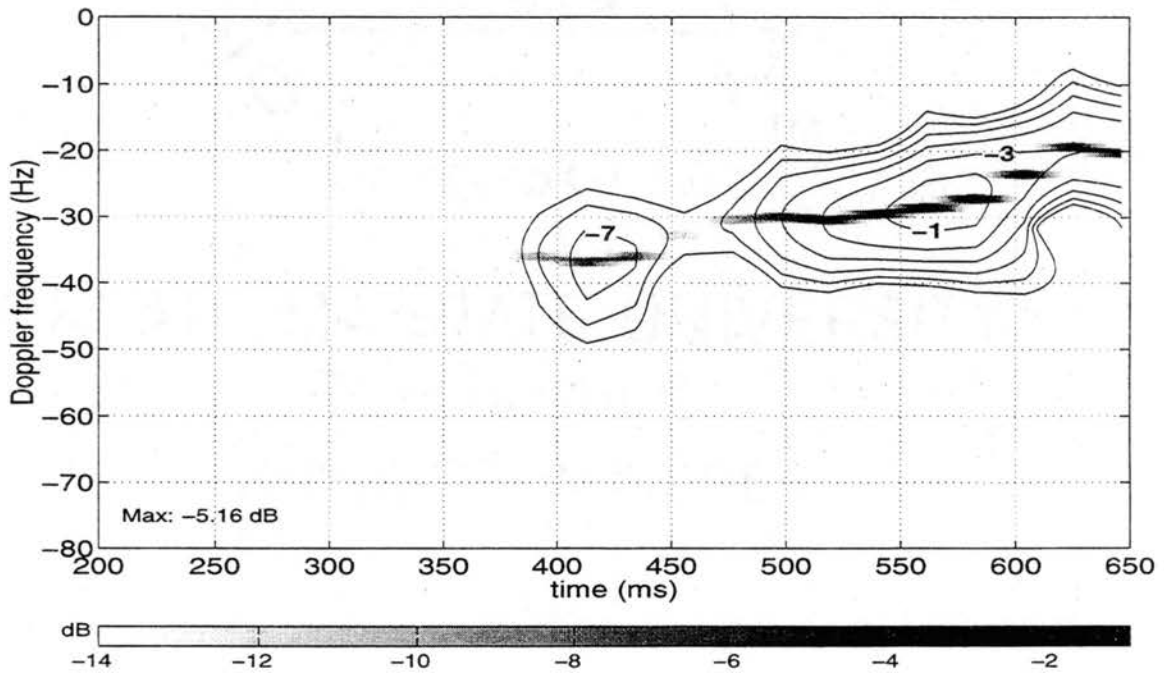
(b) HH

Figure 4.15: Time history of Doppler shift of the "clean" wave at 80° incidence and 10 GHz when looking downwind.
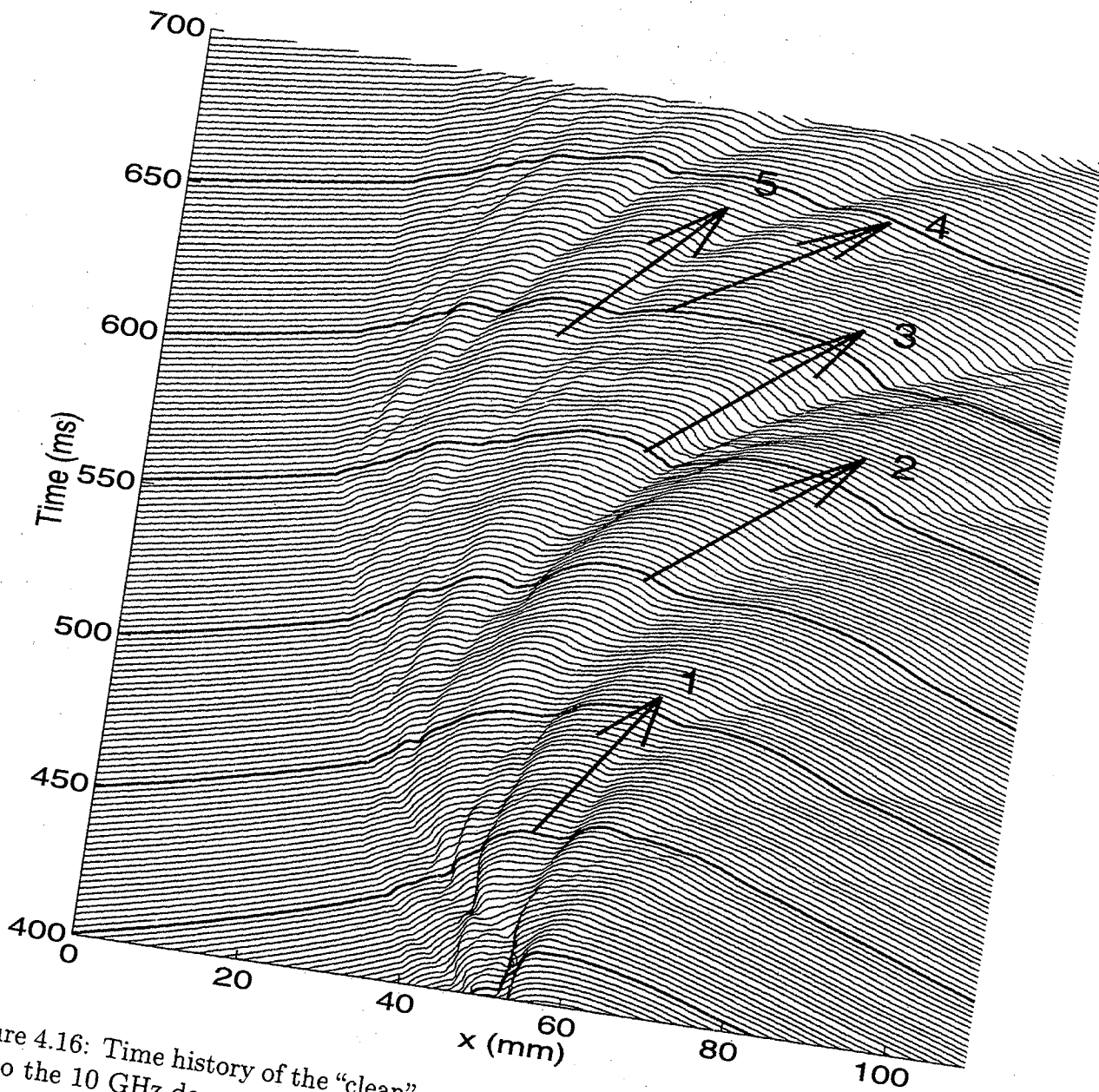
59

Figure 4.16: Time history of the "clean" wave with surface feature motion corresponding to the 10 GHz downwind response identified.
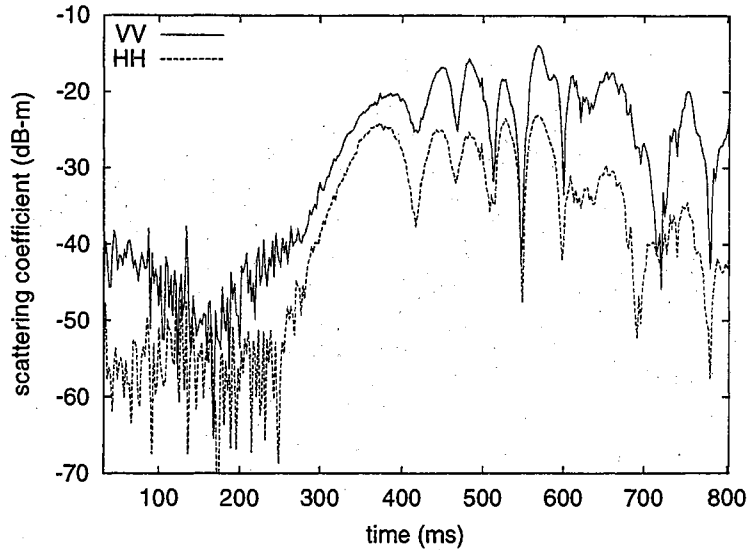
Figure 4.17: Time history of the backscattering cross-section of the "surfactant" wave at 10 GHz and nominal 80° of incidence when looking upwind.

is a more energetic spilling breaker than the "clean" wave. A second strong region occurs at 440 ms with a Doppler shift of 50 Hz, giving a slow scatterer. A third peak response is at approximately 75 Hz, peaking at 550 ms, which indicates that some scatterers are moving much faster than the wave phase velocity. Another strong slow response is centered at 620 ms with Doppler shift of 45 Hz.

The time history of the HH Doppler spectrum has approximately the same distribution as that at VV, but with lower strength. The HH slow signal of the "surfactant" surface remains much stronger than that of the "clean" surface through 570 ms. Therefore, the "surfactant" HH spectrum show more energy in the slow signal range. The strength of the first slow response peak (at 420 ms, 50 Hz) is only 2 dB lower than that of the initial fast response, and the second slow peak (at 620 ms, 45 Hz) is also only 6 dB lower. This was matched by a reduced slow response of at least 12 dB in the Doppler spectrum of the "clean" wave response.

The motions of the surface features corresponding to strong peaks in the VV Doppler spectrum have been marked by short arrows in Fig. 4.19. The first arrow shows that a jet forms when the plume outruns the gravity wave with a speed corre-

61
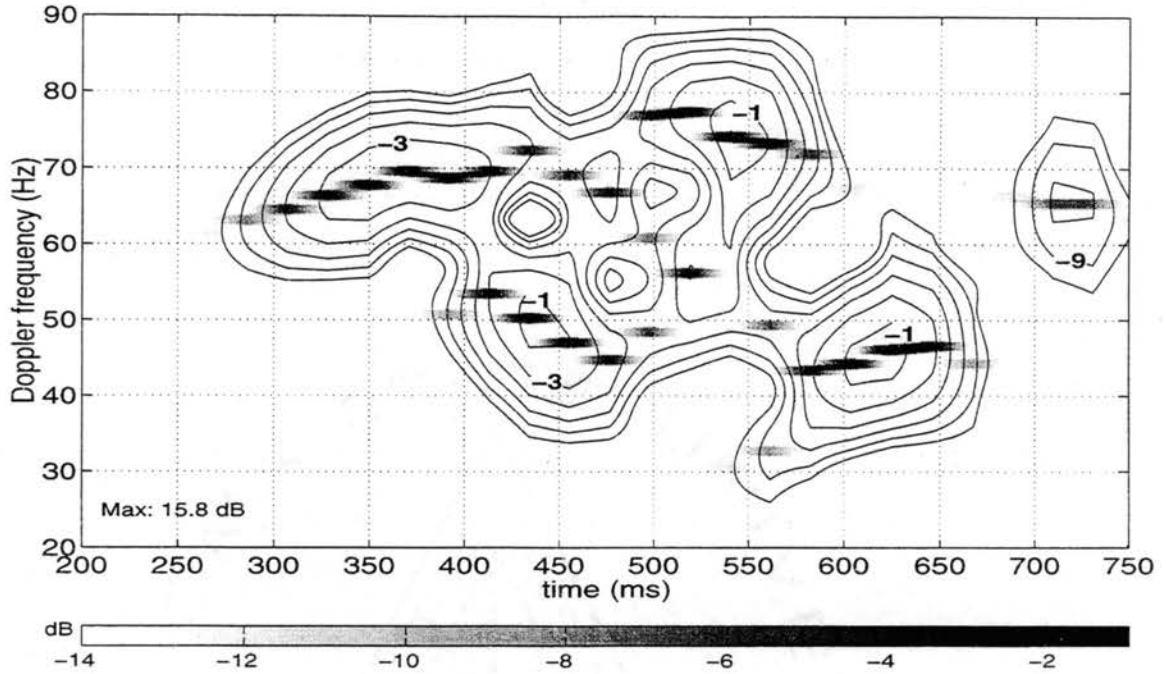
(a) VV
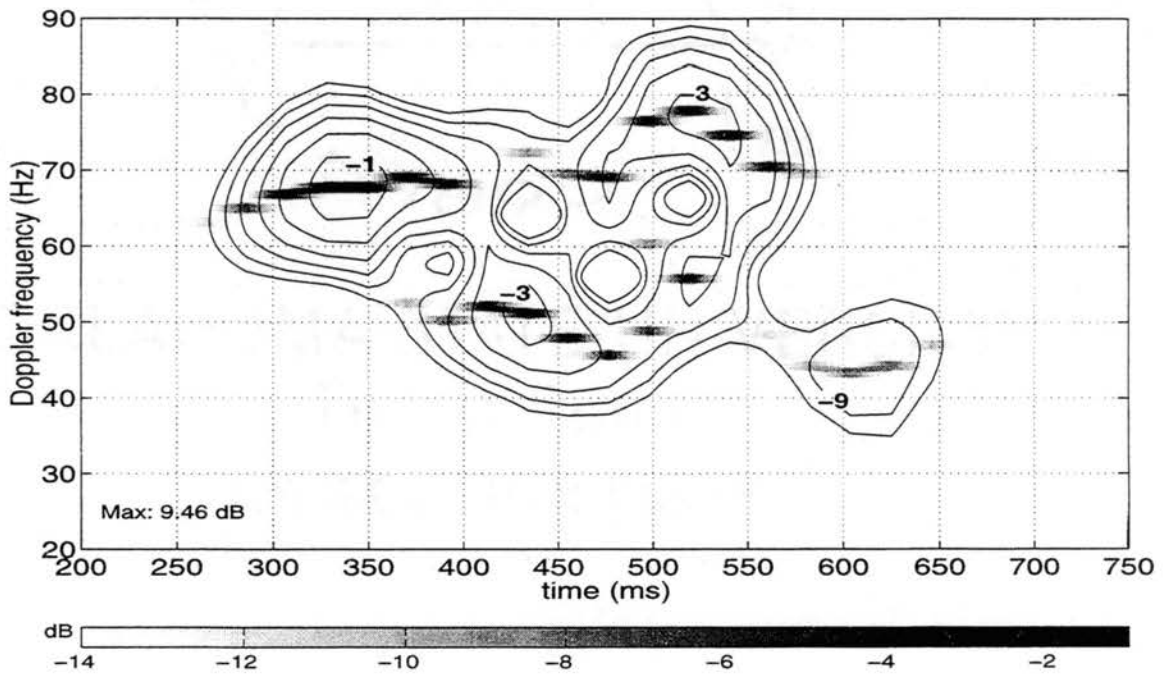
(b) HH

Figure 4.18: Time history of Doppler shift of the "surfactant" wave at 80° incidence and 10 GHz when looking upwind.

62

sponding to a Doppler shift of 70 Hz at 380 ms. The wave breaks at 400 ms, leaving the turbulent structure marked by the arrow set labeled number 2. The speed of this structure corresponds to 53 Hz at 400ms and down to 45 Hz at 500 ms. Features labeled 3 and 4 are moving faster than the phase velocity, giving shifts of 70 Hz at 400 ms and up to 78 Hz at 500 ms respectively. The fifth line shows a steep feature that moves faster than the phase velocity immediately after the second overturning event at 570 ms with a corresponding Doppler shift of 75 Hz. The sixth and seventh arrows show turbulent structures that give 45 Hz at 600 to 650 ms. The eighth arrow shows a small feature that gives the low-level 65 Hz response at 720 ms.

As was the case with the "clean" waves, the roughness on the back side of the long wave does not yield strong backscatter. Most major scatterers are located on the front face throughout the time history. The one exception is at 480 ms where the peak of a turbulent cell is sufficiently high to be illuminated and gives a response at 45 Hz. The small feature that moves forward very rapidly from 600 ms to 650 ms does produce a very fast Doppler shift. However its strength is more than 14 dB below the maximum plotted in the figure and hence does not appear. Other features, such as that at $x = 60$ mm from 450 ms to 550 ms, may produce signals of sufficient strength to detect, but can not be seen due to the limited time and frequency resolution in the plot.

4.4.2   20 GHz Response

The 20 GHz backscatter from the surfactant wave is shown in Fig. 4.20. The illumination was again upwind at 80° incidence. There is a correlation between the HH backscatter and overturning events in the wave history (micro-breaking). Overturning occurs at 370 ms, 570 ms, and 720 ms with progressively weakening strength. These are matched by strong HH returns that are equal to or even slightly exceed the

Figure 4.19: Time history of the "surfactant" wave with surface feature motion corresponding to the 10 GHz upwind response identified.

Figure 4.20: Time history of the backscattering cross-section of the "surfactant" wave at 20 GHz and nominal 80° incidence when looking upwind.
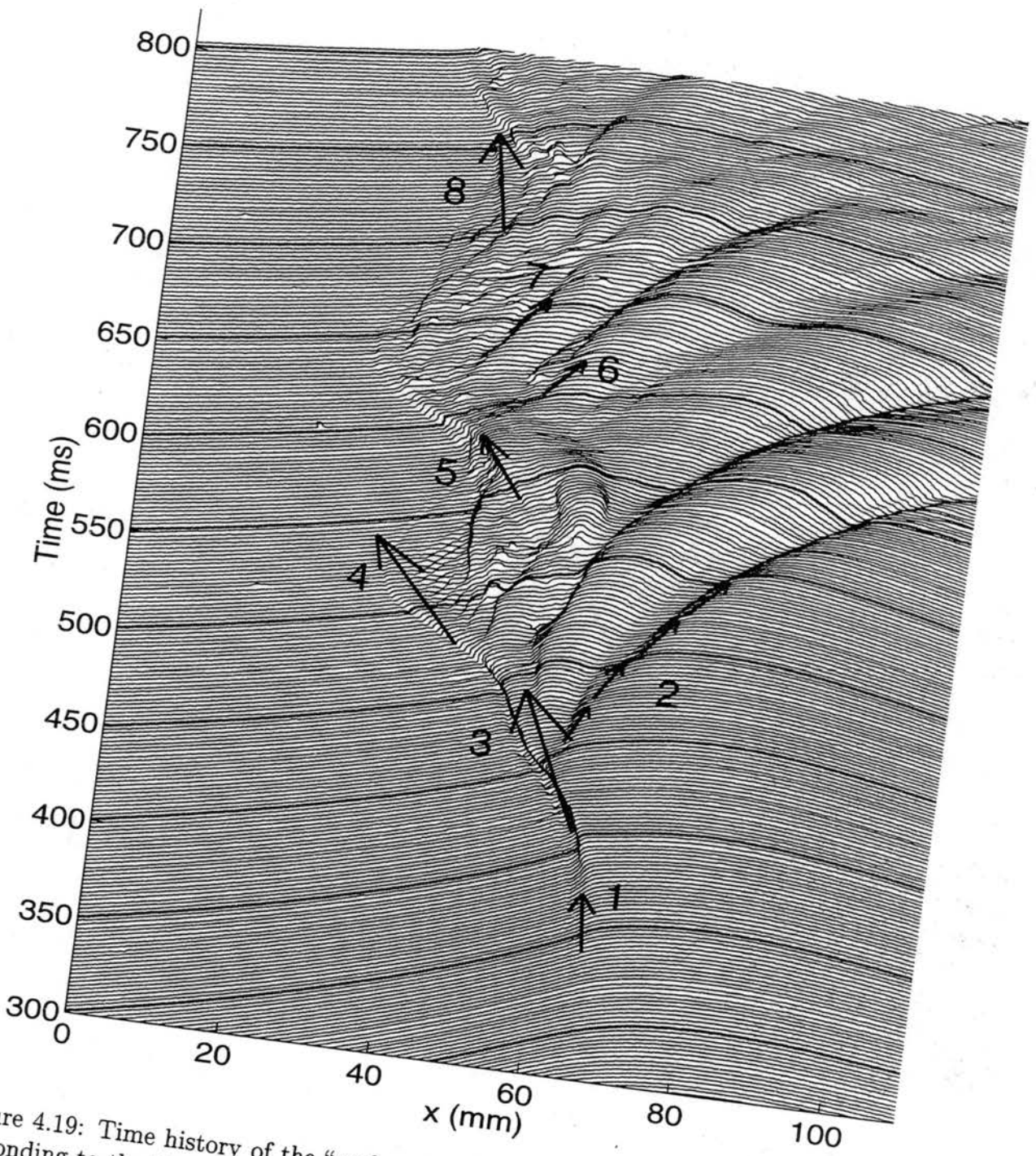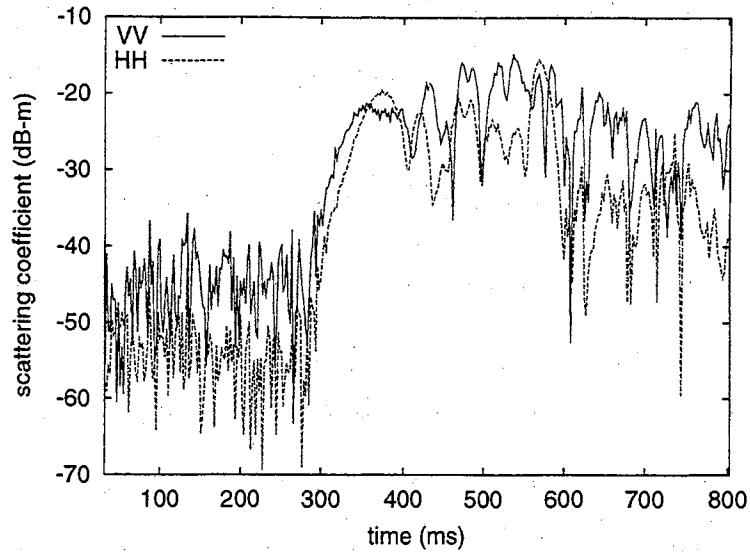
VV returns. Surface features that are very steep remain between these events, which explains why the HH response tapers off less rapidly than with the clean wave. The strongest return in both polarizations occurs at 580 ms. The corresponding Doppler shift is shown in Fig. 4.21.

The overturning events can also be recognized in the Doppler spectra of both polarizations. The Doppler shift at 140 Hz at 400 ms is the plume speed. After the initial breaking, a strong Doppler response appears at about 106 Hz at 450 ms associated with a slow moving turbulence cell. A weaker signal appears simultaneously at a higher frequency (160 Hz) associated with the fastest moving feature. The steep structure that causes the second micro-breaking produces a Doppler shift at around 125 Hz at 500 ms. Both VV and HH spectra show strong Doppler shifts at every overturning event. After the second breaking, the second fast moving feature causes a Doppler shift of 150 Hz at 530 ms while the slower moving turbulence cell gives a 110 Hz response at 630 ms in the VV spectrum. These later, less energetic turbulence structures do not have the steepness needed to give strong backscatter in HH. Hence there is no strong Doppler shift shown later than 600 ms at HH spectrum. Overall,

the 20 GHz VV spectrum responds more strongly to the fast moving, smaller features on the front face than the 10 GHz VV spectrum.

### 4.4.3 Summary of Backscattering Calculations

The numerical calculations suggest that the fast scattering that appears in high-incidence backscattering from the sea surface is due to wave breaking. When considering the clean wave, the plume that formed immediately before breaking moved faster than the wave phase velocity and gave a strong return. Turbulent cells generated by the breaking are carried by the wave orbital motion and gave slow scatter. Matching the Doppler shifts to feature velocities showed that turbulent cells on the front side and top of the wave gave the strongest backscatter. Cells on the back side are shadowed. There is also some response at Doppler shifts corresponding to speeds much higher than the wave phase velocity. These correspond to fast moving features immediately after breaking.

The "surfactant" wave produces much more energetic breaking than the "clean" wave. This should be more similar to the breaking of large ocean waves where surface tension is a less important restoring force. There are several overturning events in this time history, all matched by HH return bursts. Small super events were observed in the 20 GHz returns associated with these events.

The VV backscatter is very sensitive to small structures so makes a good small roughness detector. However, some of the smallest features can only be detected at the higher radar frequency. On the other hand, the HH response to the small-scale roughness is rather weak compared to the VV response. However, HH backscatter is a good indicator of wave overturning. The steep surface features caused by the plume can produce strong backscatter in both VV and HH polarizations in the absence of small roughness, such as the fast signal produced by the major wave breaking
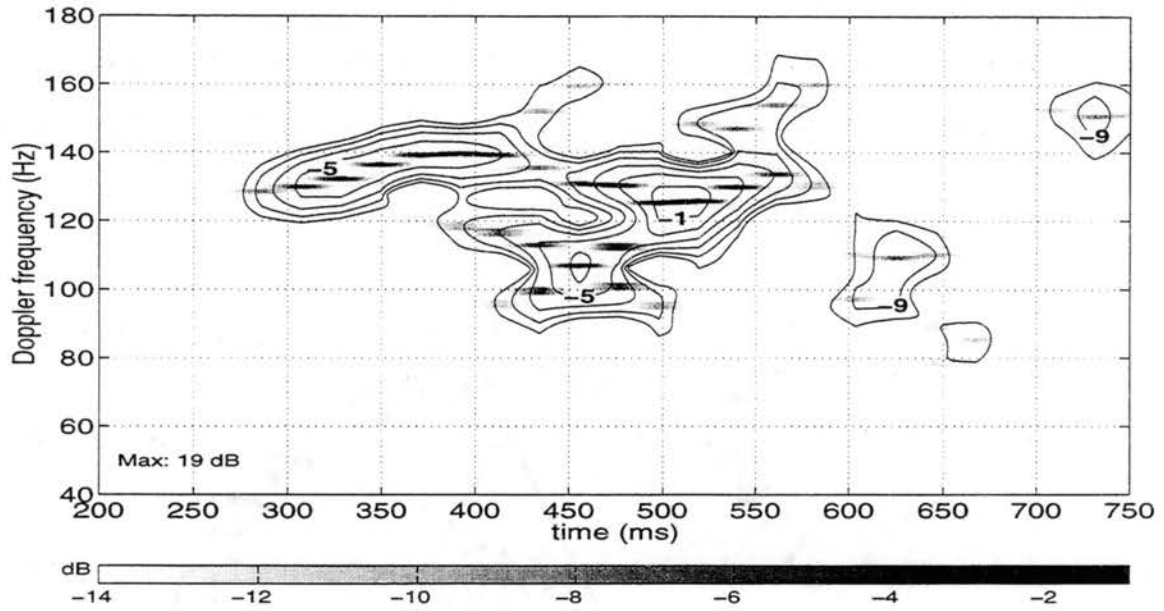
(a) VV
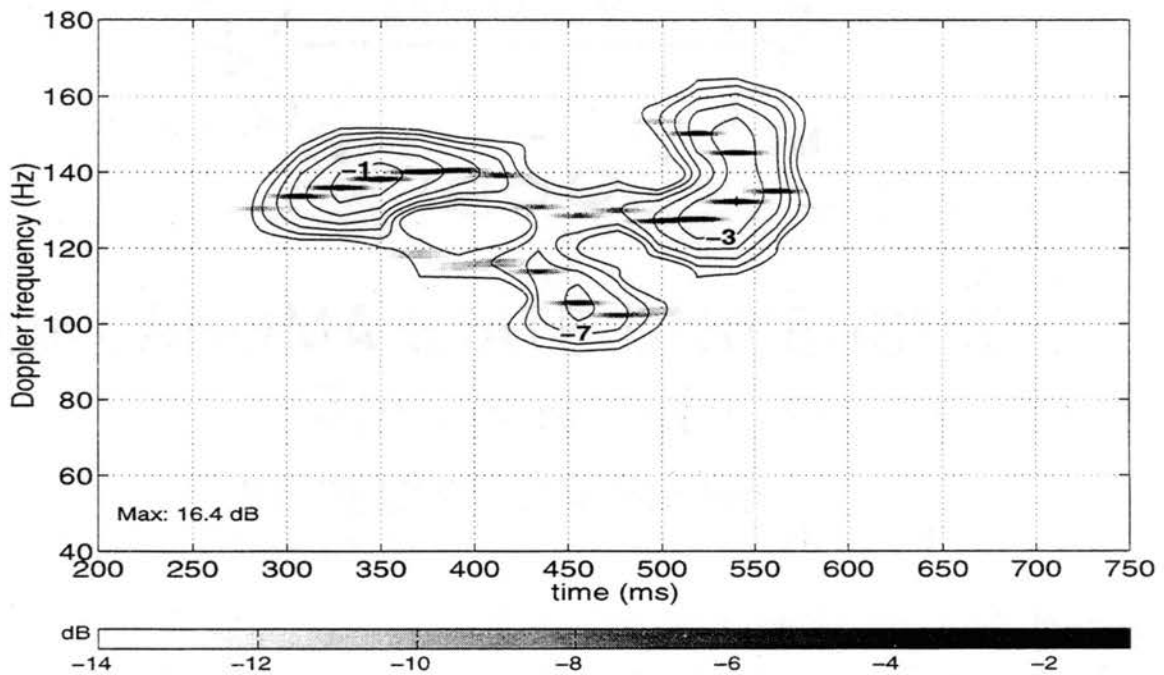
(b) HH

Figure 4.21: Time history of Doppler shift of the "surfactant" wave at 80° incidence and 20 GHz when looking upwind.

67

events. However, when the surfaces are covered by small roughness, then only HH backscatter has significant burst response to the steep feature while VV backscatter remains unaffected. This was observed at the second and third micro-breaking events of the "surfactant" waves.

4.5 Scatterers and Scattering Mechanism

Several different mechanisms can contribute to backscattered signals. Features that present surface sections perpendicular to the radar look direction will lead to quasi-specular reflection. Distributed surface roughness on the other hand most likely scatters through Bragg resonance. Rapid changes in the surface slope or curvature can give direct back-diffraction. In this section, the numerical calculation results are analyzed to find possible major scattering mechanisms giving the "fast" and "slow" scatterers.

4.5.1 "Slow" Signal

After wave breaking, turbulence structures are generated on the front side of the long wave. Since they are not bound to the large-scale wave, they move at a slower speed and drift toward the back side of the long wave. Because of the orbital motion, the speed of the turbulent cells is not uniform and the distances among adjacent turbulent cells change with time. This moves the surface roughness energy through different wave numbers, giving rapidly changing Bragg-resonant scattering. Hence the slow signals fluctuate rapidly.

Two similar examples to demonstrate signal fluctuations can be found in the backscattering from the "clean" wave during the periods from 440 ms to 455 ms and 480 ms to 506 ms. The time history of the VV returns shows two nulls, at 455 ms and 506 ms in Fig. 4.22(a). The backscatter from three sample surfaces, at 440

ms, 450 ms and 455 ms, are marked to illustrate the changing of return power at the first null. The other three markers indicate the backscatter from the surfaces at 480 ms, 495 ms and 506 ms to demonstrate the variation at the second null. The backscatter-versus-incidence-angle plots of the first three and the second three surfaces are shown in parts (b) and (c) of Fig. 4.22 respectively. The backscatter at 80° from each surface is marked by the corresponding marker used in plot (a). Bragg resonant peaks can be clearly observed in plots (b) and (c) at 80° with the earliest occurring profiles (marked by circles). They move away from 80° incidence with increasing time in both plots, which indicates the surface energy has been re-distributed to other wave numbers. Hence, the backscatter shows a null.

Possible scatterers on the surfaces at 440 ms, 450 ms, 455 ms and 465 ms that give the response in Fig. 4.22 are shown in Fig. 4.23. The facet formed by points A and B has the length and tilt angle needed to produce Bragg scattering at around 80° incidence, as found from equation (2.3). As the distance between them grows with time, surface energy has been shifted to other wave numbers, and hence the backscatter at 80° decreases. The backscatter does not again increase until a facet of similar length and tilt is formed at 465 ms.

The backscattering from the clean wave at 20 GHz does not have strong response from 450 ms to 550 ms, while the same surfaces give strong Bragg scattering at 10 GHz. Roughness structures that have surface energy at the Bragg wave number at 80° incidence and 10 GHz may not give strong Bragg scattering at same incidence angle but at higher radar frequency. Figure 4.24 shows the backscattering from a clean wave at 487 ms. While the 10 GHz response has a Bragg-resonant response at 80°, the 20 GHz response is quite low. The lack of surface energy at the Bragg wave number also explains the low-strength region from 450 ms to 550 ms in the 20 GHz "clean" wave Doppler spectra (Fig. 4.12).
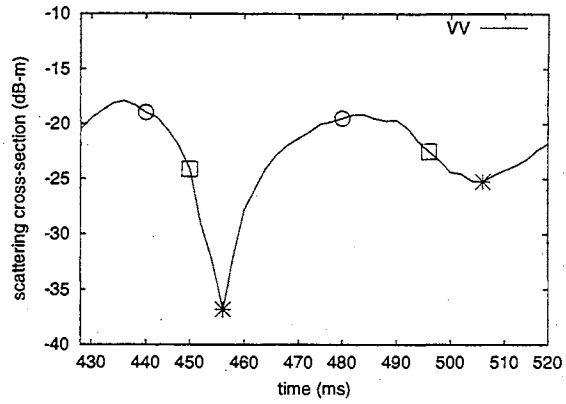
(a)
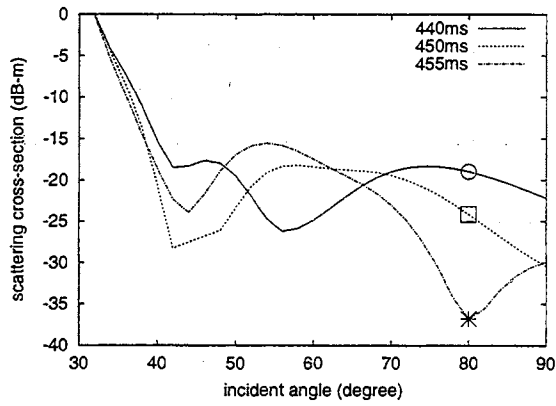
(b)
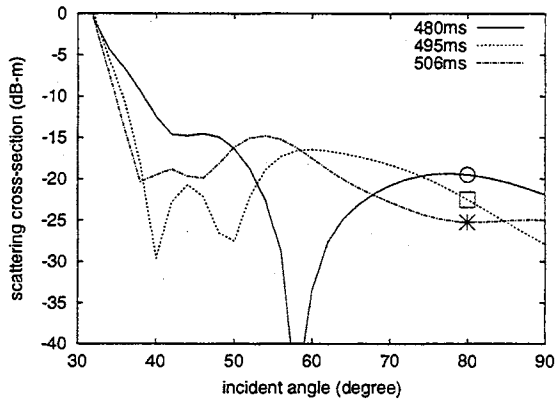
(c)

Figure 4.22: Demonstration of the changing Bragg resonance at VV polarization: (a) The time history plot of the slow signal at 10 GHz, 80° of incidence, (b) backscattering cross-section versus incidence angle during 440 ~ 455 ms, and (c) backscattering coefficient versus incidence angle during 480 ~ 506 ms from "clean" waves

Figure 4.23: Possible Bragg scatterers on "clean" surface profiles.

Figure 4.24: Comparison of the backscattering from the "clean" wave at 487 ms with radar frequencies 10 GHz and 20 GHz.
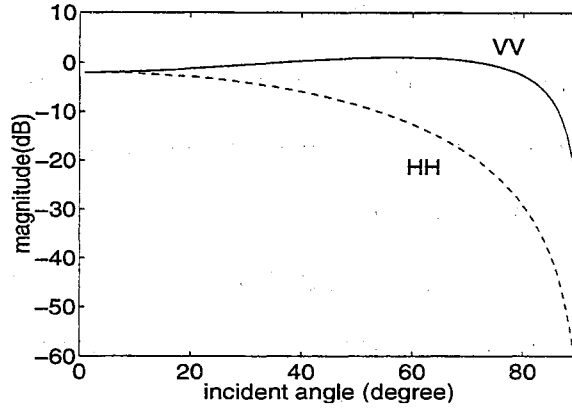
Figure 4.25: The comparison of magnitude of α_{hh} and α_{vv} at different angles of incidence
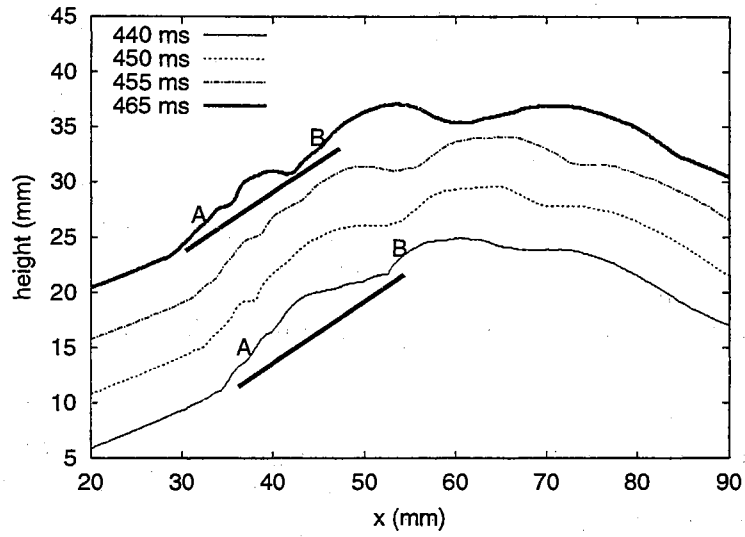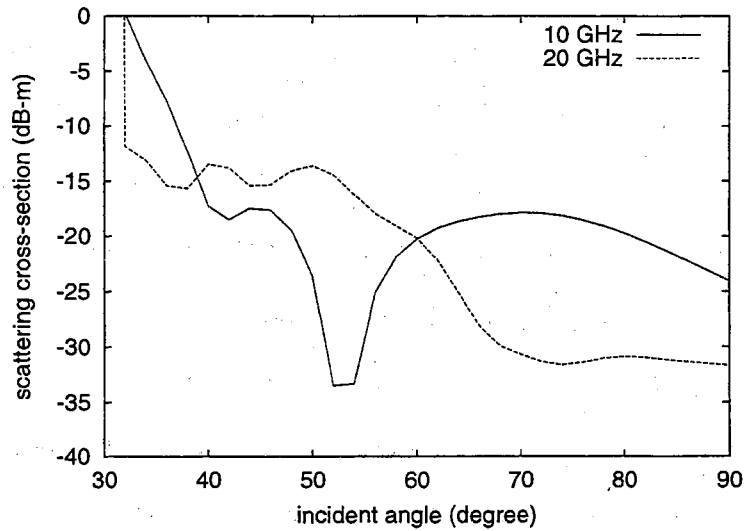
According to the SPM model, the backscattering magnitude in HH and VV should be due to the small-scale roughness energy at the same spectral wave number. In this case, the ratio of the HH and VV scattering can be simply predicted by the ratio of the coefficients α_{hh} and α_{vv} in Eq. (3.6). Figure 4.25 shows the dependence of α_{vv} and α_{hh} on the incidence angle. The magnitude of α_{vv} remains large from small to large incidence angles, while α_{hh}'s drops rapidly.

The VV/HH ratio of the 10 GHz numerical calculation for both "clean" and "surfactant" waves are shown in Fig. 4.26. (VV/HH ratios are plotted here rather than the more typical HH/VV ratios for clarity in the following discussion.) In this section, only the slow signal is considered (after 370 ms for "clean" waves and after 400 ms for "surfactant" waves). The VV/HH ratio of the fast signal will be discussed later in section 4.5.2. Overall the ratio shows a general increasing trend in the slow signal range. The nominal incidence angle of the radar is 80°. However, the dominant Bragg-resonant scatterers are located on the front face of the long wave, so the tilt of the long wave modifies the local incidence angle, and hence modulates the VV/HH ratio from that expected at 80° incidence. The VV/HH ratio of the slow signal therefore increases with increasing local incidence angle which is caused by the decreasing front-face slope with time after initial wave breaking.

To confirm that the scattering is indeed due to Bragg scattering, the ratio of α_{vv} and α_{hh} is also plotted in Fig. 4.26. The local angle of incidence was found from the tilt of the large-scale surface at the point where the dominant scatterer was identified. Two examples plotted in Fig. 4.27 shows the identified local facet. The local incidence angle is defined as the angle between the incident ray and the vector normal to the facet. The MM/GTD calculations show good agreement with SPM α ratios at most time. There are two major exceptions in the part (a), calculated from "clean" waves. The first occurs at 550 ms where a relative minimum appeared in the backscatter due to little small-scale roughness appearing on the front face. The backscatter from the back-side roughness becomes relatively important at that time, as confirmed by the Doppler history of Fig. 4.8. This violates the assumption that all major scatterers are located on the same planar facet. The small-scale roughness on different facets has different local incidence so the numerical results disagree with the SPM α ratios. Another period of poor agreement ranges from 650 ms to 697 ms. Here the crest amplitude has dropped dramatically so that the back side of the wave is no longer shadowed. Again, some backscatter is contributed from scatterers on the back side, and hence the SPM α ratios fail to predict the true VV/HH ratio.

With the "surfactant" waves, the overall trend of the VV/HH ratio is also increasing in the slow signal after the initial breaking (part (b) of Fig. 4.26). However, the slope of the front face of the "surfactant" wave is larger than that of the "clean" wave at the end of the time history. Hence the VV/HH ratio of "surfactant" wave does not increase to the same level as that of "clean" wave. The SPM α ratios agree with numerical calculations well except from 680 ms to 730 ms, where the front-side roughness has little energy and back-side roughness has a rather large amplitude. Therefore, this is another case where backscatter from the back-side roughness invalids the SPM α ratio prediction. The VV/HH ratio drops at 550 ms where a micro-breaking event

occurs. The local incidence angles decrease due to steep features present at that time, and hence the SPM α ratio reduces.

Overall the backscatter after the initial wave breaking ("slow" signal) has good agreement with predictions based on SPM. The backscatter strength oscillation can be explained by the surface energy shifting away or into the Bragg resonant wave number. The backscatter strength ratio between polarizations matches the SPM α ratio as well. These results suggest that Bragg scattering is the major scattering mechanism responsible for the backscattering after the initial breaking event.

4.5.2 "Fast" Signal

The VV signal is approximately 5 dB greater than the HH signal from 150 ms to 325 ms in the 10 GHz "clean" wave results . There is no distributed surface roughness on the surface in this period, so Bragg resonance is not responsible for the fast signal. From 250 ms to 300 ms small parasitic capillary waves appear on the front face, but their wavelengths (3 $\sim$ 5 mm) are far too small to give a Bragg resonance at 10 GHz. The local incidence angle on the front face also changes with time. This would suggest a change in the VV/HH ratio if strong Bragg scattering were occurring, which is not observed.

The surfaces profiles from "clean" waves around the time when the maximum backscatter occurs are plotted in Fig. 4.28, zoomed around the plume area. The steep features of the plume marked by "A" and "B" are possible scatterers for the fast signal. As the size of the plume grows, the steep feature becomes more apparent (from A to B), and the strength of backscatter increases. When the plume breaks and the steep feature changes the backscatter strength drops to a null. The surface slope does not exceed 70° at any points, so quasi-specular scattering is not occurring. Diffraction from the plume is therefore the major scattering mechanism for the fast
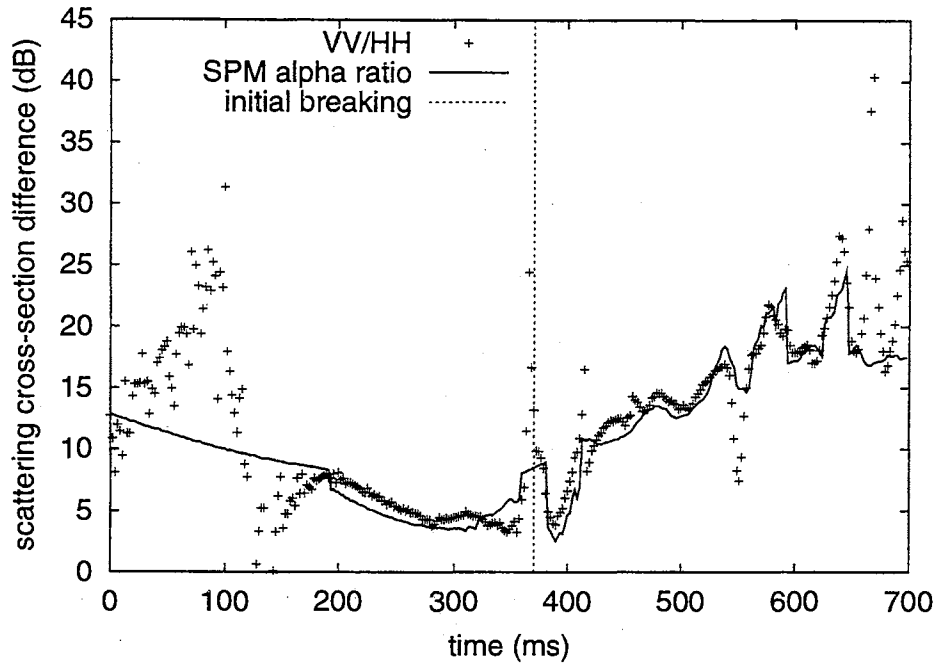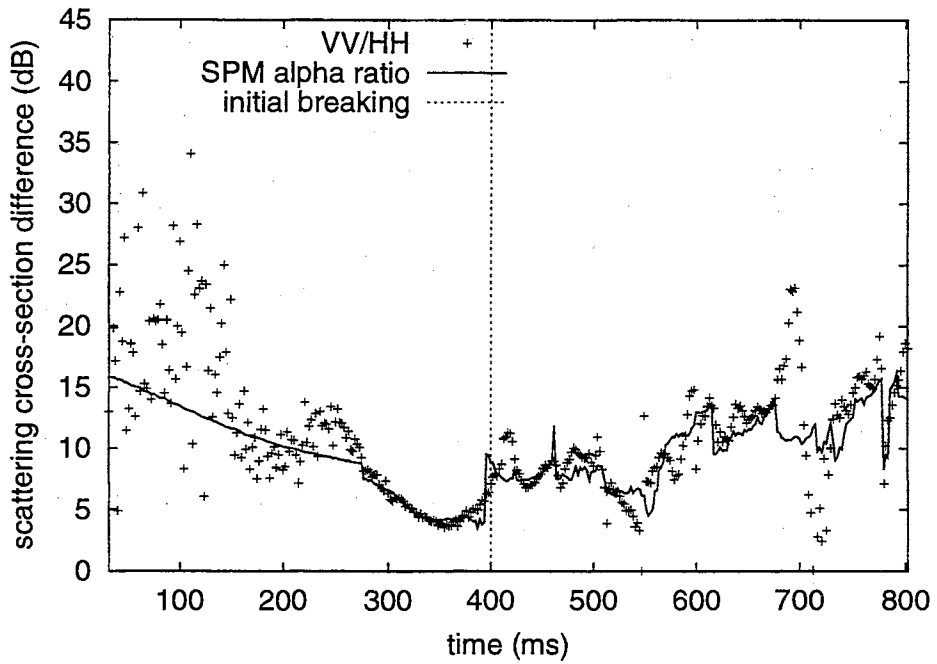
Figure 4.26: Difference in the VV and HH backscattering at 10 GHz and nominal 80°
incidence. (a) "Clean" waves and (b) "Surfactant" waves. The solid line is the SPM
α ratio, and the points are the numerical calculation results. The dotted vertical line
shows the time of initial wave breaking.
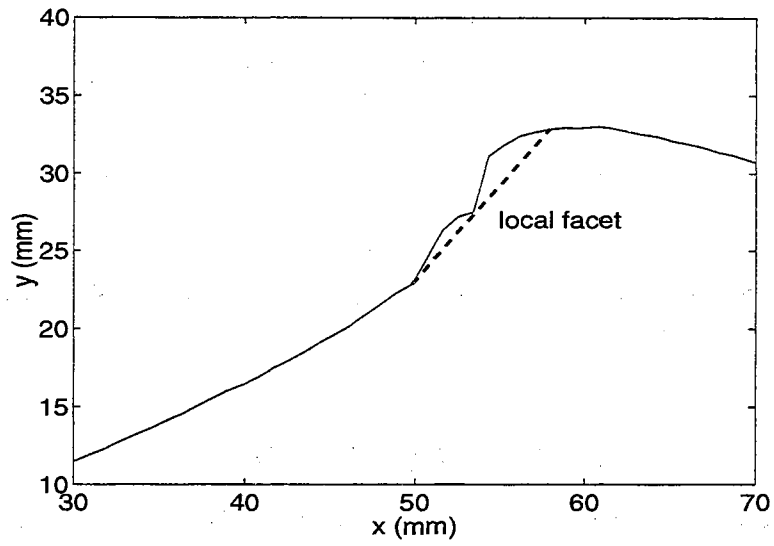
(a)
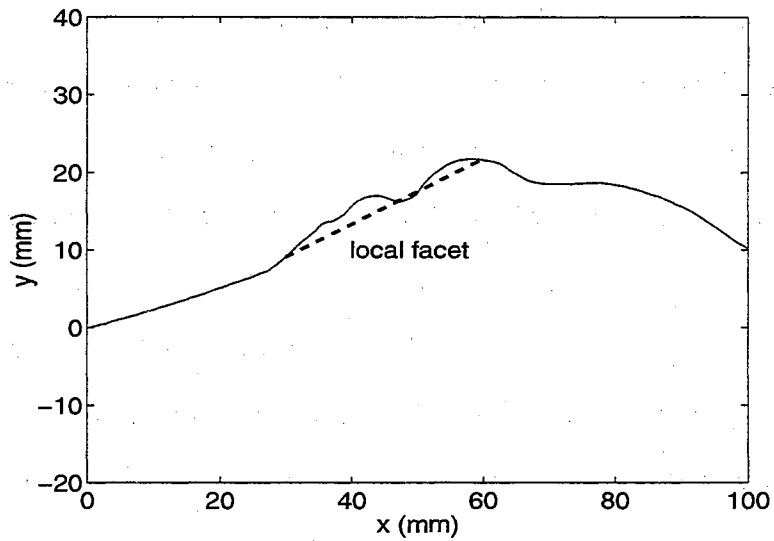
(b)

Figure 4.27: The definition of local facets: (a) "Clean" wave at 328 ms before breaking. (b) "Clean" wave at 500 ms after breaking.
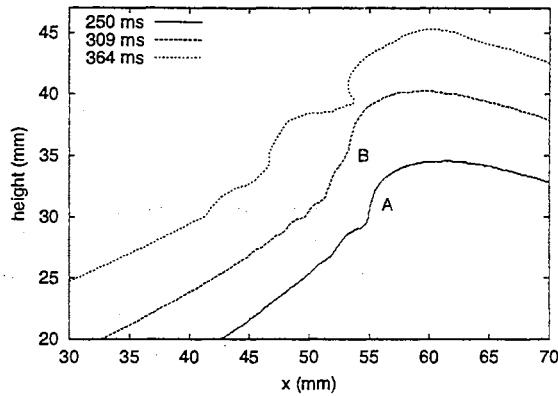
Figure 4.28: Plume profiles at different times on "clean" waves

signal.

SPM can predict the backscattering from small roughness even though a Bragg resonance is not established. The steep feature in Fig. 4.28 is just a single bulge which does not produce Bragg scattering but the VV/HH ratios of the fast signal can be predicted by the SPM α ratio accurately in Fig. 4.26(a). The local incidence angle is evaluated by taking the slope of local facet on which the steep feature is sitting into account. An example of defining local facet is shown in Fig. 4.27(a). Also, there are some steep features formed by the turbulence immediately after wave breaking. One of them causes the "clean" wave VV/HH ratio to drop to a null at around 400 ms, and another one is at 550 ms of "surfactant" wave. The SPM α ratio can trace it only by taking the slope of the steep feature into account.

When the incident radar frequency rises to 20 GHz, the backscatters from the steepest features give VV/HH ratios close to 0 dB at high incidence angles. This is probably because the tangent-plane approximation needed for accurate specular reflection is better met at the higher frequency.

Steep features which may cause the fast signal are also observed in the "surfactant" waves. The "surfactant" waves are more energetic, and the steep features are even more apparent. They almost always appear prior to overturning events. Figures 4.29(a) and (b) shows the steep features (marked by "A") presents before the first
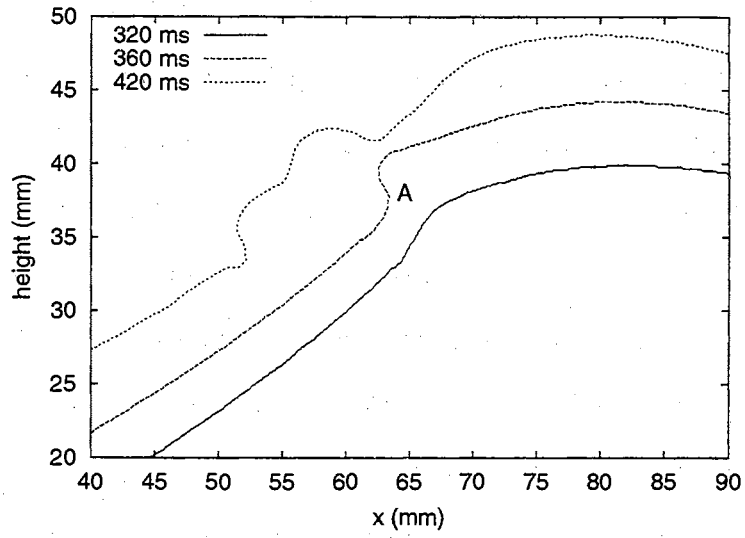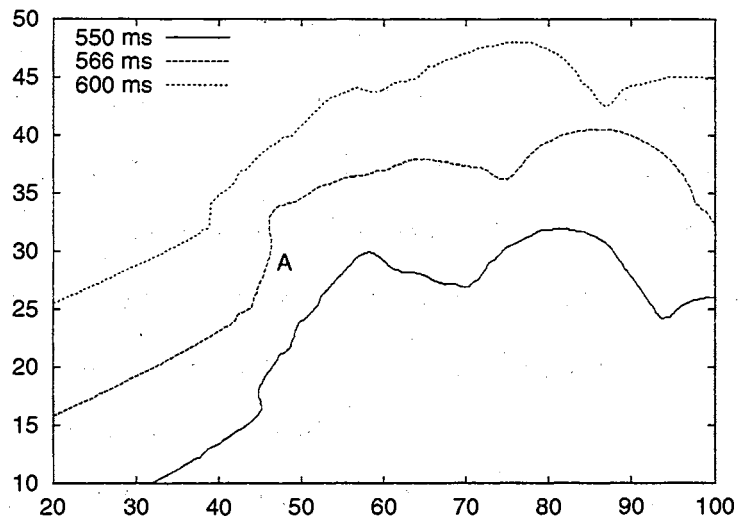
Figure 4.29: The steep feature on the "surfactant" waves at (a) the initial breaking and (b) the second overturning.

and second overturning. Strong HH backscatter is continuously produced by these steep features. At 10 GHz, the HH bursts are not apparent. However, at 20 GHz, the shorter wavelength scatters more strongly from these features and produces a burst in HH returns (Fig. 4.20 at 370 ms, 570 ms and 720 ms). The scatter from these steep features may or may not have HH/VV ratios approaching or exceeding 0 dB. Super events appeared at 570 ms and 720 ms at 20 GHz, but not at 10 GHz.

The SPM α ratios also agree with numerical calculations well in the fast signal range for the "surfactant" waves (Fig. 4.26(b)). The VV/HH ratio of both "surfactant" and "clean" waves decreases before wave breaking, and reaches its global minimum at the time where the steepest feature is formed. This agreement suggests that the diffraction from the steep feature is the major scattering mechanism for the backscatter before or immediately after breaking event.

4.5.3 Summary

The HH/VV ratios of the numerically calculated results agree with the SPM α ratios well as long as the major scattering is caused by the small roughness and the major scatterers are localized to one planar facet. The slope of that planar facet is used to evaluate the local incidence angle for the computation of the SPM α ratio. Correct identification of the scatterers is necessary to achieve good agreement, so the strongest scatterers can be recognized more confidently.

The roughness distributed over the surface suggests that Bragg scattering is responsible for the "slow" scattering after wave breaking. This is supported by the Bragg resonant peaks shown in the plots of the backscatter from individual surfaces after wave breaking at various incidence angles in Fig. 4.22(b) and (c). The oscillation of the slow signal strength is caused by the shifting of surface energy among wave numbers. Finally, the increasing VV/HH ratios after wave breaking further support

of the Bragg-scattering conjecture. The slow signal is due to turbulent structures remaining on the surface after breaking.

The plume is thought to be responsible for the fast scattering because of the time correlation with the Doppler signal. This is verified by the disappearance of the fast signal when radar is looking downwind and the plume is shadowed. The VV/HH ratio of the plume scatter may less than, equal, or greater than 0 dB, depending upon the radar frequency and the geometry.

Small super events have been observed in the backscatter from the "surfactant" waves at 20 GHz. However, there is only one crest included in each surface in this data set, which is quite different from the realistic ocean surfaces where multiple wavelengths of the dominant waves are illuminated, all of which will include wind-generated roughness on the surface. Hence, the direct comparison of the numerical calculations with the field observations may not be appropriate. Also, as mentioned in the first chapter, the multiple-bounce model proposed by Wetzel [16] is considered a prominent model to explain the super events. In order to study the effect of multi-path reflection and Brewster angle damping, the front faces of these surface data can be artificially extended to allow the multiple-bounce reflection to occur, so that sea spike events may be observed in the numerical calculations. This is considered in the following section.

4.6   Super Events

As mentioned, direct measurements of the front face of the long wave are available only for a short distance. This removes the multi-path reflection point that is thought to give "super events" where the HH backscatter exceeds that at VV [10]. The surface was therefore extended as in Fig. 4.30 to give a reflection point. This extension is different from the roll-off infinite extensions for the MM/GTD approach. Here a
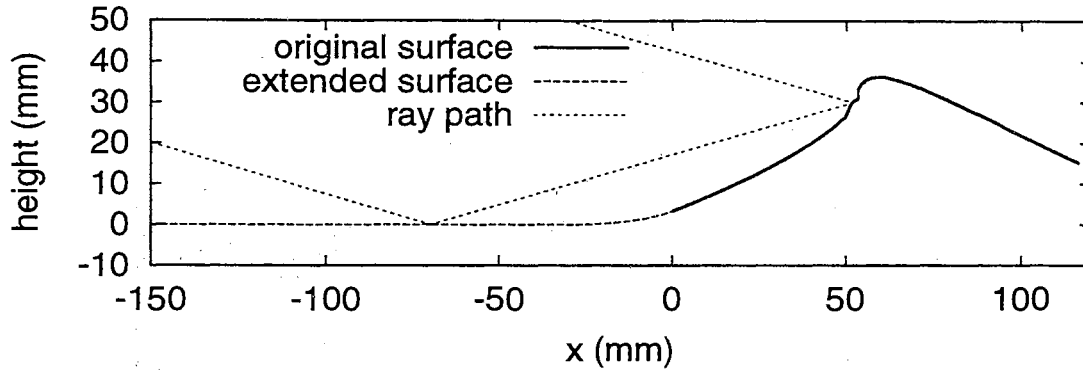
Figure 4.30: Front-side extension of a "clean" wave at 318 ms

finite length horizontal extension is smoothly connected to the original surface. The MM/GTD infinite extension is attached at the front of the horizontal section, as was done by West [20]. The length of the horizontal extension is 500 mm. The short-dashed line in the figure shows a multi-path reflection ray path between the extension and the plume structure.

4.6.1 Backscatter from Extended "Clean" Wave

The time history of the amplitude of the scattering cross-section of the horizontally extended "clean" waves at 80° incidence and 10 GHz is given in Fig. 4.31. It is very similar to the time history of the backscatter from the original "clean" waves except that the amplitudes before wave breaking have changed. The fast signal strength of VV is reduced about 2 dB over all, and that of HH is increased about 4 dB. Therefore, the HH/VV ratio approaches 0 dB, and even slightly exceeds it for a short time, giving a brief super event. The VV slow signal remains almost unchanged. The HH slow signal at around 400 ms increases about 2 dB, however, the change decreases with time.

The added extension only changes the fast signal which appears only when the plume is forming. This confirms that plume scatter is responsible for the multi-path reflection. As predicted by the model of Wetzel [16], the multi-path reflection gives
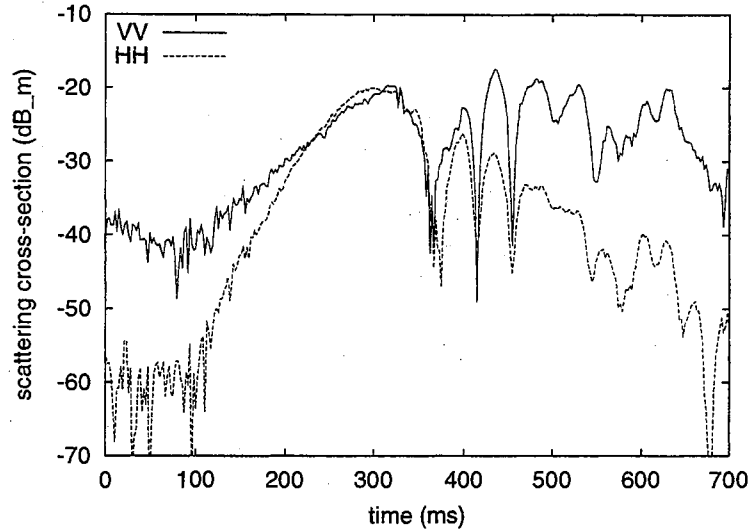
(a) extended surface

Figure 4.31: The time history of the backscattering cross-section from the front-face-extended "clean" wave at 10 GHz and 80° incidence when looking upwind.

interference that increases the HH backscatter and decreases the VV backscatter at this specific incidence angle and radar frequency. Stronger super events can occur at other incidence angles. This is shown by Fig. 4.32 where the backscatter from the single extended surface at 300 ms is plotted. As expected, interference oscillation patterns appear with changing incidence due to the changing multi-path length. The Brewster angle damping further reduces the oscillation range of VV backscatter, especially at high incidence angles [17]. The interference causes a strong super event at 75°. Other runs (not shown) showed that a stronger super event occurred at at 80° incidence and 14 GHz.

The Doppler history of the scattering from the extended wave is shown in Fig. 4.33. Comparison with Fig. 4.8 shows that the locations of the relative local peaks in the spectrum are almost unchanged by the extension. For example, the fast Doppler shift of 63 Hz at 300ms, the slow Doppler shift of 48 Hz from 430 ms to 530 ms, and the very fast Doppler shift of 72 Hz from 400 ms to 450 ms in VV response are not affected.
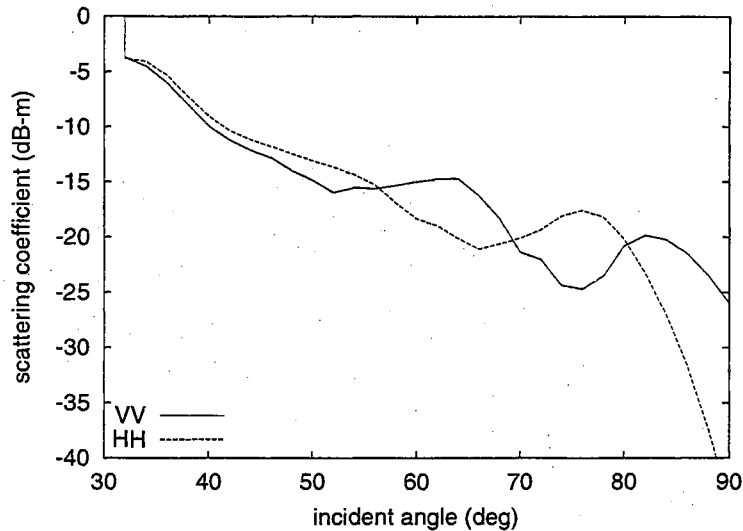
Figure 4.32: The backscatter versus incidence angle from the front-side-extended "clean" wave at 300 ms and 10 GHz.

The multi-path reflection and the Brewster angle damping only modified the location of the global maximum. For the original surfaces, the global maximum appeared at the initial fast Doppler peak at both polarization. With extension, the magnitude of the fast Doppler signal decreased at VV, so a slow signal is now maximum. The HH maximum remains at the fast Doppler signal, but the magnitude is now slightly higher.

As a final check, the Doppler shift was calculated from the complete time history of the returns rather than from windowed sub-domains. The results with and without the horizontal extension are shown in part (a) and (b) of Fig. 4.34 respectively. The Doppler splitting effect is evident in both plots, with the fast and slow peaks located at 64 Hz and 49 Hz respectively. The VV fast peak is about 3 dB stronger than the slow peak while the HH fast peak is 9 dB stronger than the slow peak. Including the multi-path reflection increased the HH fast signal to the same strength level as the VV fast signal. On the other hand, the strengths of the VV peaks only changed slightly. The extended surface results agree with the observations of Lee *et al.* [2] which showed a similar splitting shown in Fig. 1.3 when examining mechanically
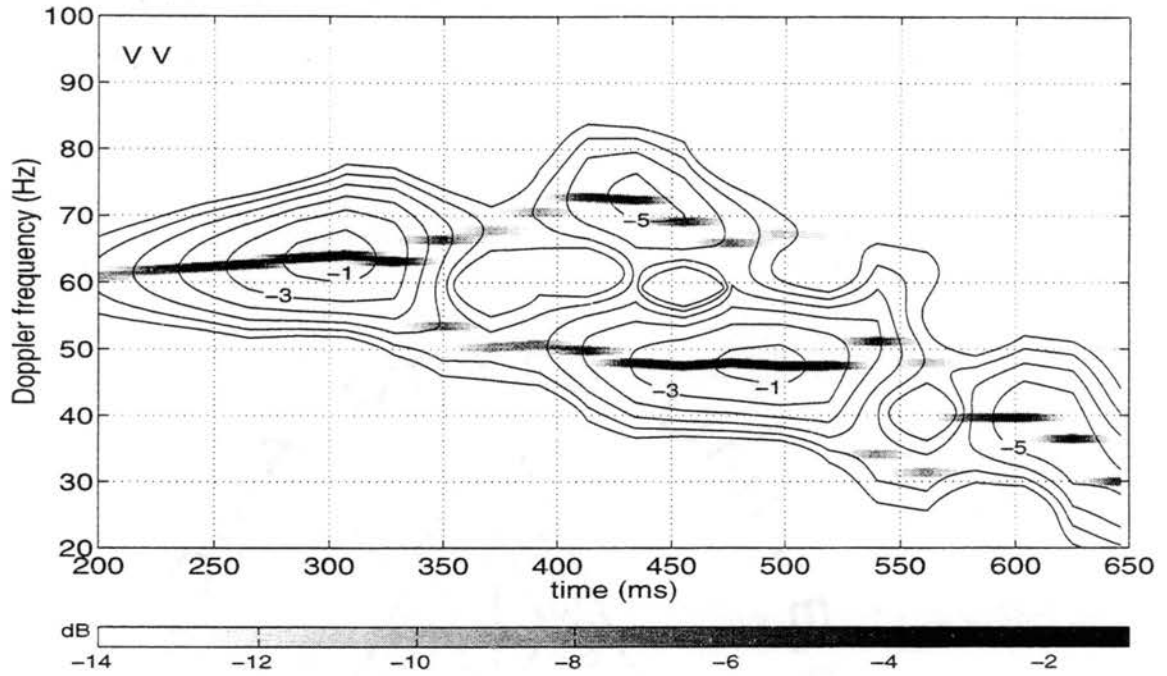
(a) Extended surface, VV
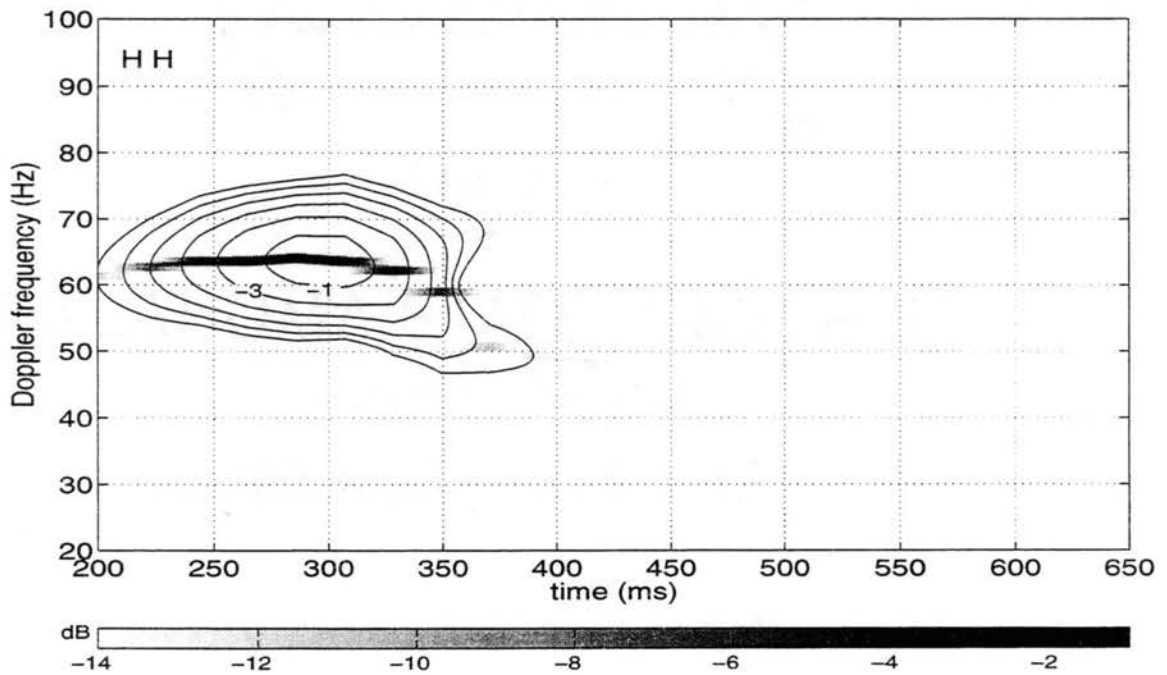
(b) Extended surface, HH

Figure 4.33: Time history of the Doppler shift from the artificially extended "clean" waves at 80° incidence and 10 GHz.

generated waves with no wind. Under different illumination conditions, the increase in the HH fast-scatter strength can be large, and the HH/VV ratio can be much greater than 0 dB.
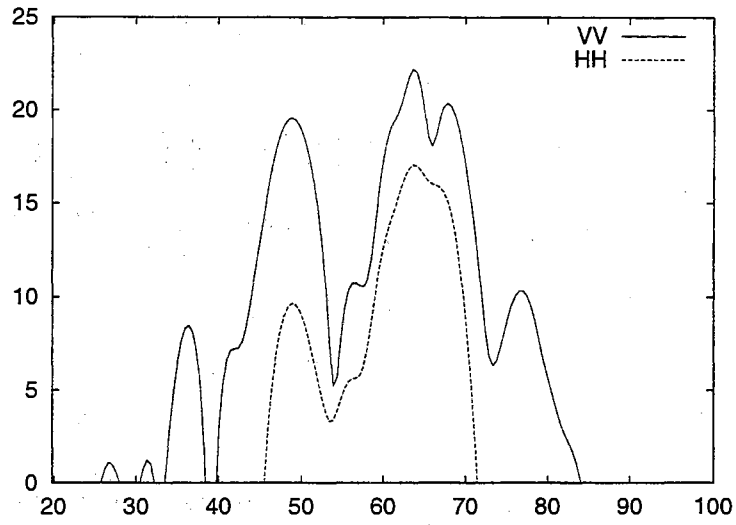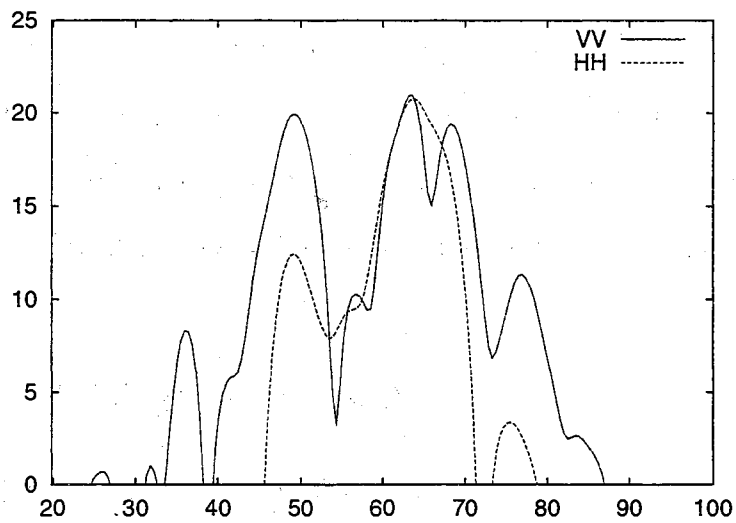
Figure 4.34: Doppler spectrum of the total backscatter from the (a) original (b) front-side extended "clean" waves at 80° incidence and 10 GHz when looking upwind.

Chapter 5

BACKSCATTERING SIMULATIONS WITH TSM MODEL

Slow and fast scatterers have been identified in the backscatter from the sample breaking wave profiles calculated by the numerical MM/GTD approach. Analysis of the backscatter has identified likely surface features and scattering mechanisms responsible for the slow and fast scatter. In this chapter the ability of the two-scale surface analytical scattering model to predict the calculated scattering is investigated. The perturbation approach of Brown [35] is used to allow an instantaneous comparison of the two-scale model (TSM) scattered field with the MM/GTD results.

5.1   TSM Simulations Procedures

Application of the TSM requires the rough surface be separated into large- and small-scale components. This is often achieved by applying an ideal, brickwall low-pass filter in the surface wave-number domain to obtain the large-scale surface, while a high-pass filter with the same cutoff threshold yields the small-scale surface [41]. This approach is particularly useful when the scattering surface is generated numerically from a given roughness spectrum. The large- and small-scale components can then be generated

independently. This approach is not as useful when treating the deterministic surfaces considered here. A brick-wall filter can only be applied by performing a fast Fourier transform (FFT) and setting the spectral components outside the passband to zero. This introduces unacceptable ringing (the Gibbs phenomenon) when the inverse FFT is performed to give the filtered surface. Instead, another filtering method was used.

The large-scale surface was obtained by applying multiple passes of a three point triangular-weighted moving average (MA) filter to the original surface. The impulse response of the filter is given by

$$h(n) = \frac{x(n-1) + 2x(n) + x(n+1)}{4} \tag{5.1}$$

As the number of passes used is large, this is equivalent to applying a single pass of a multi-point Gaussian MA filter. Figure 5.1(a) shows the effective MA window after 100 passes of the three point MA filter. The effective low-pass transfer function is found from the FFT of plot (a) of the figure, shown in plot (b). This function again approximates a Gaussian envelope. Since the transfer function repeats itself every 2π, the effective cutoff wave number for this filter can be derived as

$$K_c = [\int_0^\pi (\frac{1 + \cos K}{2})^N dK]/\Delta x \tag{5.2}$$

where Δx is the sampling step size in horizontal direction, and N is the number of MA passes. The cutoff threshold is also shown in Fig. 5.1(a).

Application of the moving average requires that the surface be sampled uniformly in the horizontal direction. The surface elevation data was provided as a series of x-y points that were non-uniformly spaced in each dimension. The surfaces were therefore resampled. A cubic spline interpolation algorithm from the FITPACK subroutine [48] was used to resample the surface, which maintains continuity of the second derivative in the resampled surface. This algorithm has an adjustable tension factor. A zero tension factor will give cubic-spline interpolation, and a higher value (e.g. 50) will
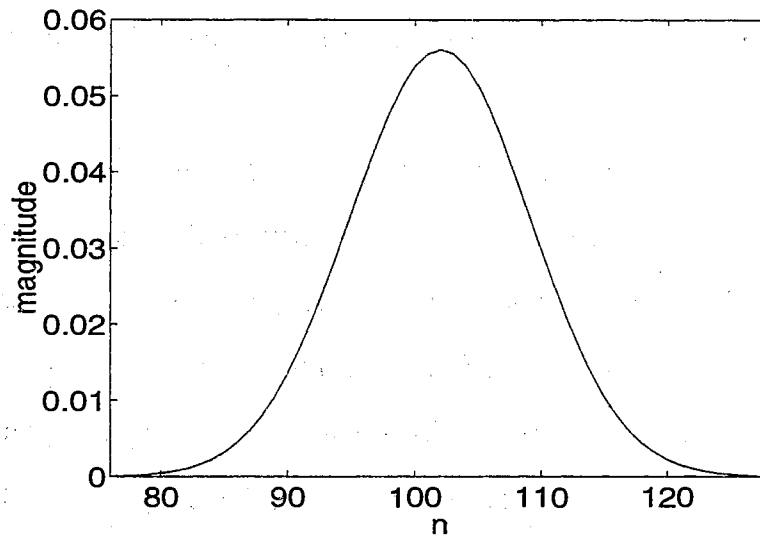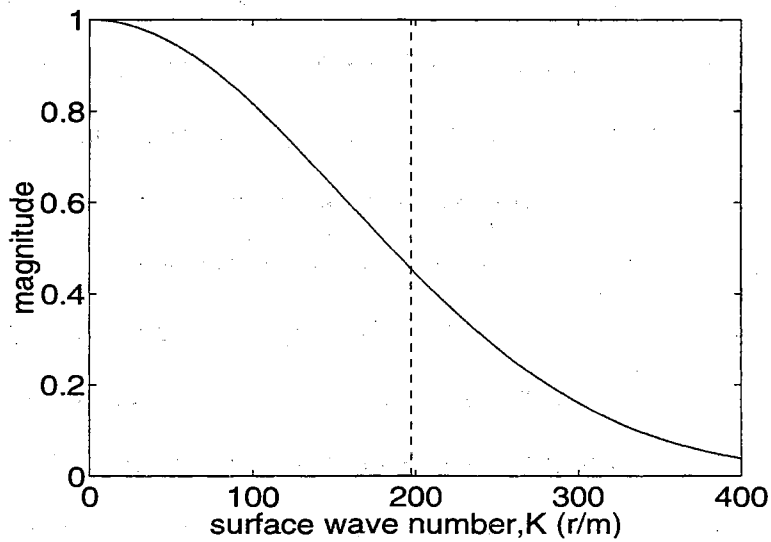
Figure 5.1: (a) The equivalent MA filter after 100 passes of the three-point MA filter. The spatial sampling step size is 0.9 mm. (b) Transfer function of the 3-point MA filter after 100 passes. The dashed lines indicate the effective cutoff threshold of $K_c = k$ at 10 GHz.

give a more linear-interpolation-like result. A tension factor of 50 is used for this study. Once the large-scale surface has been obtained, it can be subtracted from the original surface to yield the small-scale component. Figure 5.2 shows a surface separation example.

Resampling and filtering surfaces with multi-valued sections required additional consideration. Multi-valued surfaces clearly cannot be uniformly sampled in the horizontal plane. Instead, the resampling and filtering was performed in a plane tilted to the horizontal where the surface could be described by a single-valued function. The two-scale model was also applied in this tilted reference plane. The tilting angle was chosen so that the tilted front face was approximately horizontal (Fig. 5.3(a)). In some cases even the tilting was insufficient to remove all multi-valued points. This case is demonstrated in Fig. 5.3(b), which shows the "clean" wave at 360 ms. This was addressed by making small modifications on the surface itself, as shown in the figure. Figure 5.4 shows the comparison of the MM/GTD calculated backscatter from the modified and original surface at different incidence angles at both polarizations. The only significant difference in the response is a small change in the depth of the null at 77° in the VV case. Changes of this magnitude make very little difference in the total energy scattered from the complete time history and are of little importance.

After the surface separation, the Kirchhoff's approximation was applied on the large-scale surface to find the electric surface current using equation (3.1) and (3.2). The KA far-field scattering can then be computed via the radiation equation (3.3) or (3.4). The SPM method presented by Brown [35] was applied on the small-scale surface to find the perturbed field (Eq. (3.9)). The TSM field is the coherent addition of those two fields. The MM/GTD results serves as the exact results, to which the TSM results will be compared.

90
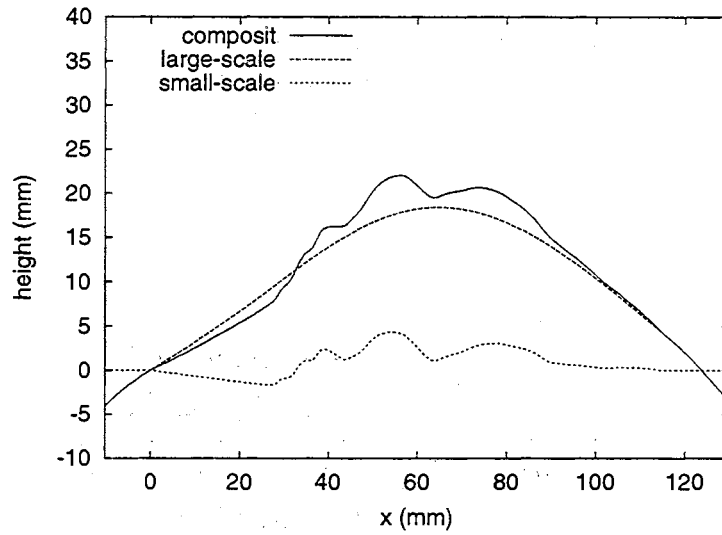
(a)
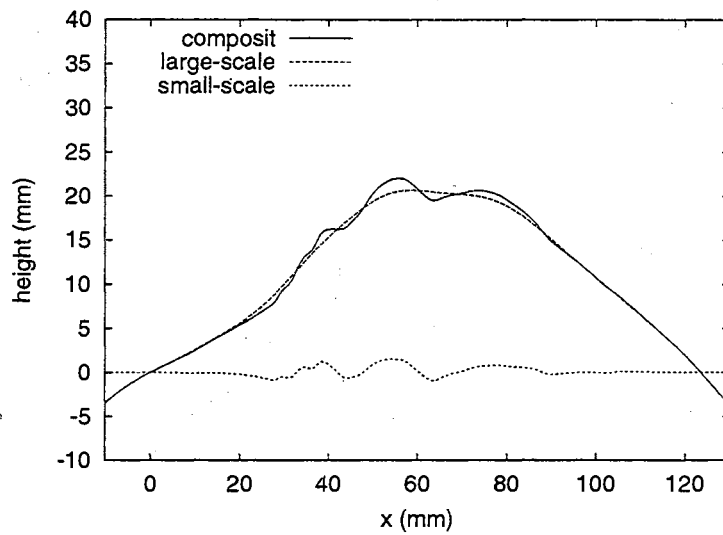
(b)

Figure 5.2: Examples of surface separations via different thresholds. (a) $K_c = k/3.0$.
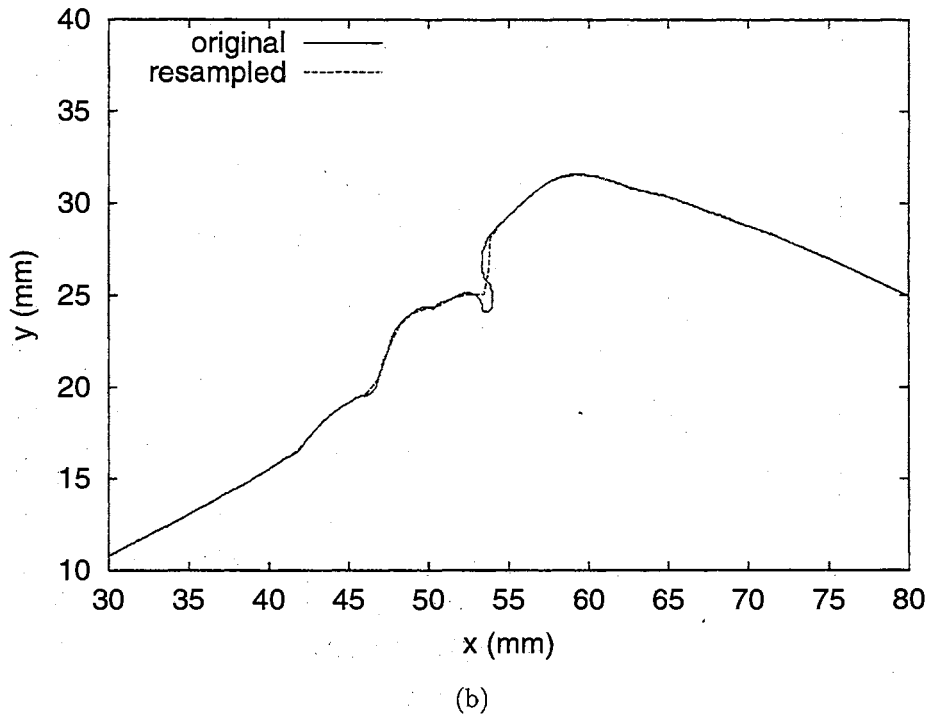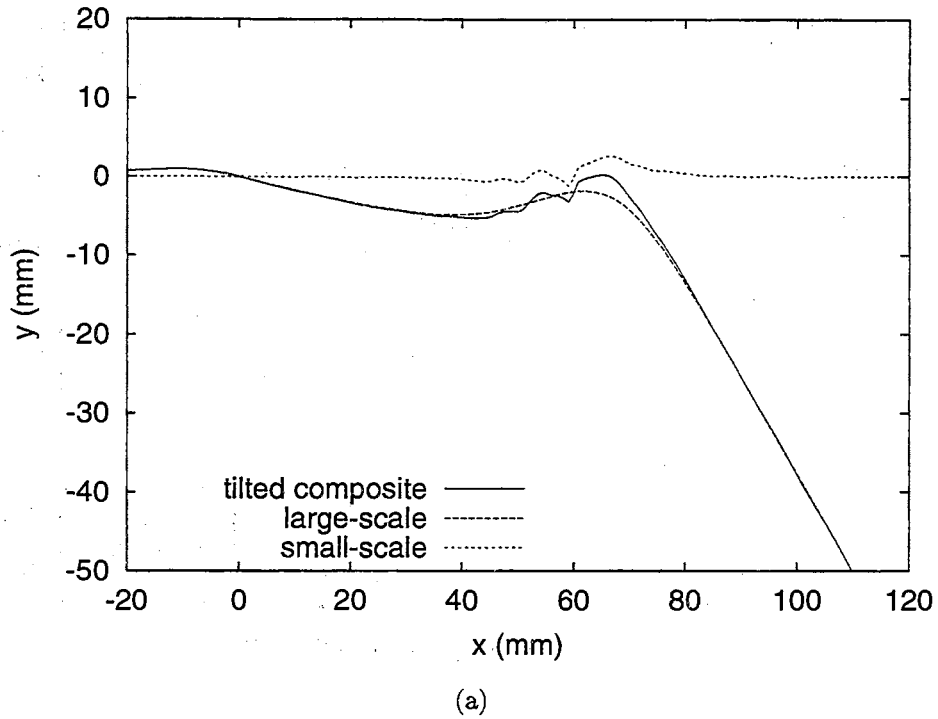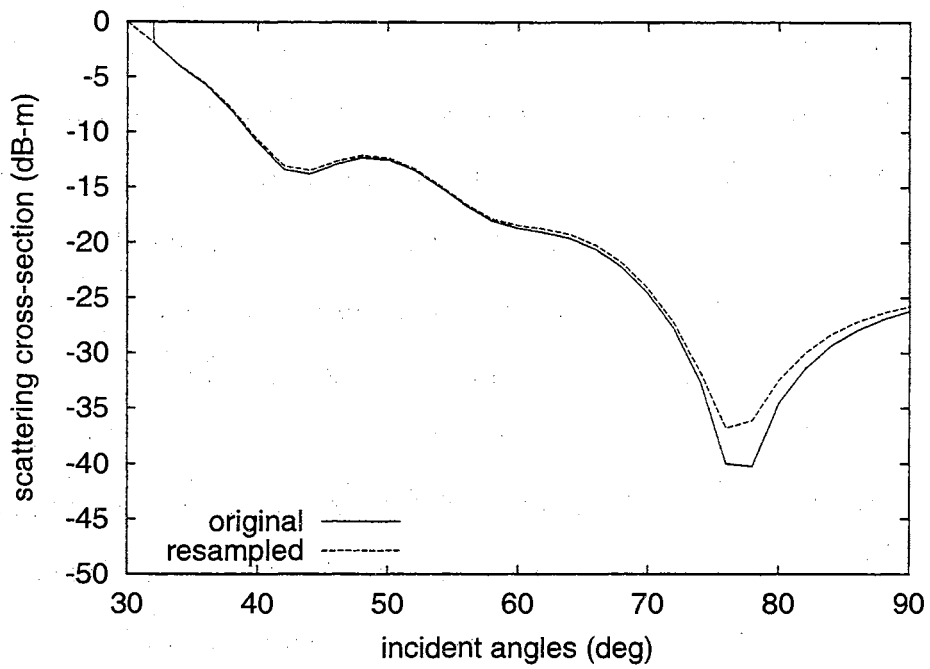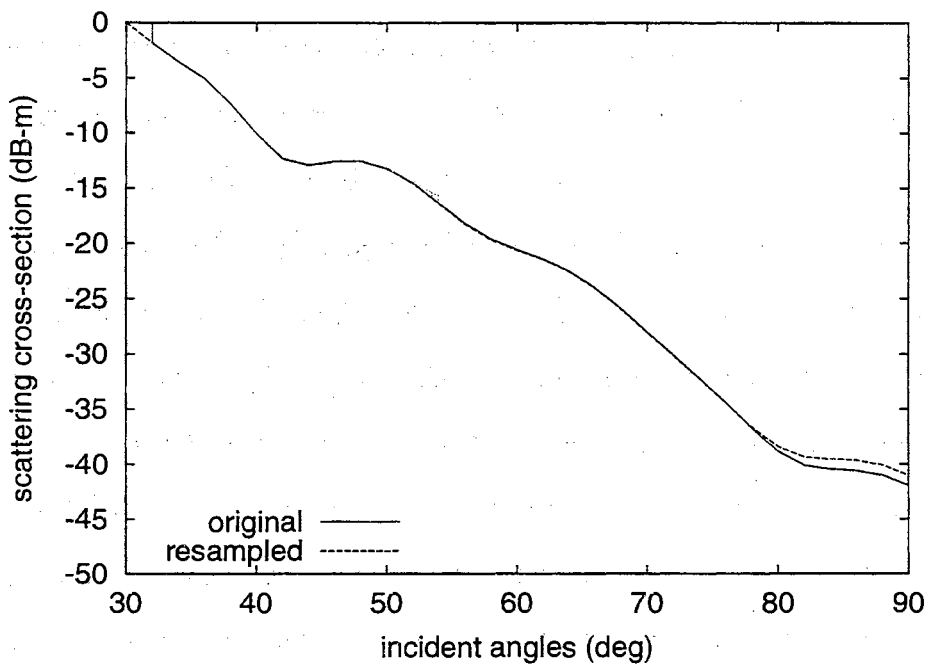(b) $K_c = k$.

(a)

(b)

Figure 5.3: Surface separation example. (a) The tilted composite and separated surfaces. (b) Original and resampled surface from "clean" wave at 360 ms.

Figure 5.4: Calculated 10 GHz backscatter from original and resampled "clean" waves at 360 ms. (a) VV. (b) HH.

93

5.2 Surface Separation Threshold

The goal of the surface-scale separation is to yield a large-scale surface that is sufficiently smooth that the Kirchhoff approximation can be accurately applied (i.e. the radius of curvature is large compared to the electromagnetic wavelength), while the remaining small-scale roughness should have an amplitude much smaller than the radar wavelength. These criteria can not always be easily met simultaneously. A cutoff threshold must be chosen that minimizes the errors introduced by failures to meet these criteria.

As mentioned previously, different thresholds have been used for the scale separation in the literature. For example, Brown [35] used the cutoff $K_c = k/3.0$, where k is the radar wave number. Durden and Veseckey used $K_c = k/2.0$. However, these studies limited the application of TSM to surface numerically generated from idealized linear roughness spectra. The deterministic surfaces considered here are very nonlinear. (Breaking itself is a nonlinear process.) The net result is that more energy appears at a given short wave number than expected from the linear spectra, and the surface height criterion for the SPM approximation is violated using the earlier thresholds. This is shown in Fig. 5.2(a), which shows the separation of the "clean" wave at 487 ms surface using $K_c = k/3.0$ at 10 GHz ($\lambda = 3\,\mathrm{cm}$). In this work a threshold of $K_c = k$ is used. The application to the 487 ms surface is shown in Fig. 5.2(b). Less energy is now contained in the small-scale surface, and its maximum deviation of $\pm 2\,\mathrm{mm}$ meets the requirement to be small compared to the 30 mm wavelength. The resulting large-scale surface also meets large radius curvature requirement. Other thresholds might give better results with other surfaces, but it is not realistic to expect an optimal value be found for different surfaces (e.g. surfaces before and after breaking). Calculation of the complete scattering history with different thresholds showed that $K_c = k$ gives the best overall accuracy across the complete time history

at the large incidence angles with which we are concerned. Other thresholds that yield improved results at specific times will also be shown.

5.3 Time History of the TSM Calculations

5.3.1 "Clean" Waves

The backscatter from the "clean" wave at 80° incidence and 10 GHz calculated by TSM is compared with the MM/GTD results in Fig. 5.5. The magnitudes of the backscatter computed by the KA and SPM components of TSM are also plotted to show the contributions from large- and small-scale surfaces respectively. The VV TSM results are almost exclusively due to scatter from the small-scale surface computed using SPM. The KA results are more than 15 dB lower, and hence do not have a significant effect on the TSM results. Overall the VV TSM results agree well with the reference MM/GTD scattering, but there are still some regions of small disagreement. One is in the neighborhood of 570 ms, and the other is after 620 ms where TSM under-predicts by about 3 dB on average.

At HH the TSM results do not agree as well with the MM/GTD results, especially in the fast signal region where it under-predicts by about 3 dB. In the slow signal period, TSM still accurately predicts the backscatter until about 650 ms. After that, the signal strengths are lower than -45 dB and TSM does not agree with MM/GTD. Although the KA scattering levels are similar at both polarizations, the TSM results are more affected by the KA contribution at HH than at VV because of the lower SPM response at HH.

At 300 ms, the peak SPM scattering in HH is about 10 dB below that in VV while the total scattering differs only about 3 dB. The backscatter from the large-scale surface computed with KA is too weak to raise the TSM level to the correct level at

HH. Figure 5.2 shows the large-scale surface at 300 ms after separation. The plume structure is completely removed from the large-scale surface when the separation $K_c = k$ is used. Hence the KA results do not have a significant contribution. Changing the separation threshold to $K_c = k/0.8$ returns energy to the large-scale surface, as shown in Fig. 5.2.

The TSM backscatter calculation using the larger surface separation wave number of $K_c = k/0.8$ is plotted in Fig. 5.7. TSM calculations at VV still agree reasonably well with MM/GTD results. The SPM contribution drops by about 3 dB, due to the reduced surface height in the small-scale surface with the fast signal, but shows little change in the slow signal. On the other hand, the KA results increase about 5 dB in both the fast and slow signals. The net results is that TSM is not dramatically affected by the changing cutoff wave number.

The TSM results of the fast signal at HH however are improved by using the larger cutoff wave number. The TSM returns almost overlap the MM/GTD results before 400 ms. However, the backscatter at later times is over-predicted by TSM. The decreasing of SPM due to the higher cutoff wave number is similar to that in the VV case, but the backscatter from large-scale surface calculated using KA increases in the slow signal, and leads the over-prediction of TSM.

Discussions

The calculations applied to the clean wave shows that while TSM applied using cutoff wave number $K_c = k/1.0$ can accurately predict the VV backscatter, the larger cutoff of $K_c = k/0.8$ is more appropriate for the fast signal at HH polarization. It was shown in Chapter 4 that the fast signal is produced by the plume feature through the diffractive scattering. Because of the rather large radius of curvature of the plume compared to the radar wavelength, the diffractive backscattering from a single bulge
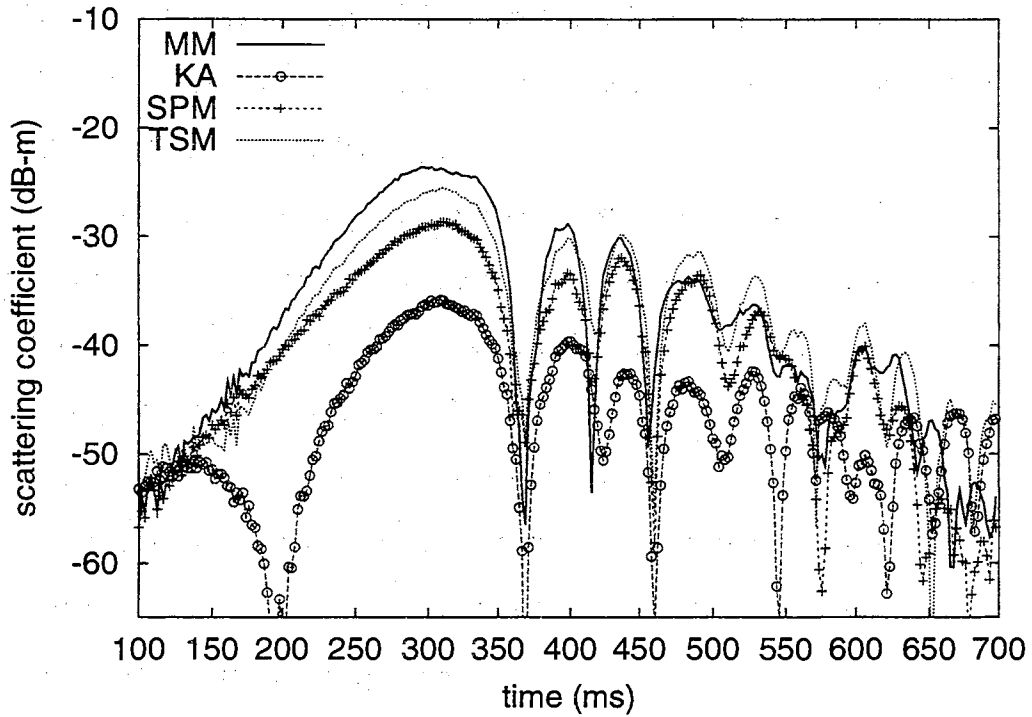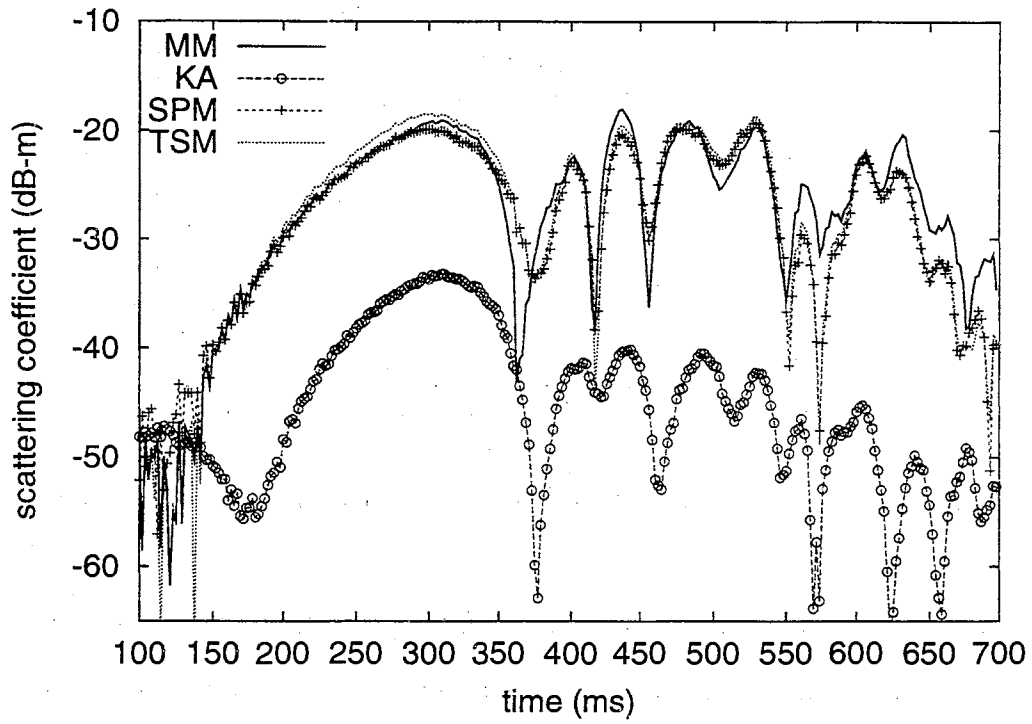
Figure 5.5: Backscattering from "clean" wave calculated using TSM with $K_c = k$ compared with the MM/GTD results at 80° incidence and 10 GHz. (a) VV (upper plot). (b) HH (lower plot).
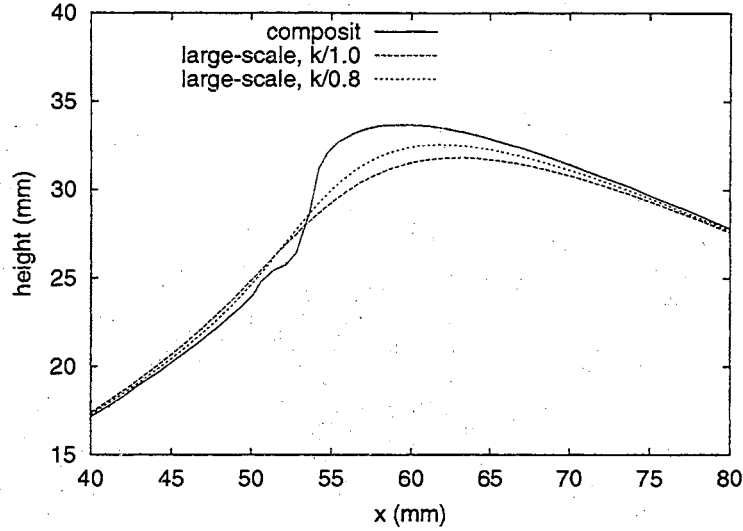
Figure 5.6: Large-scale surface of "clean" wave at 300 ms separated by different cutoff wave numbers.

can be well predicted by the KA approach. Therefore, it is more appropriate to distribute most of the plume feature into the large-scale surface and compute the diffractive backscatter through KA. Figure 5.6 showed that the large-scale surface produced using the cutoff $K_c = k/0.8$ had more of the plume feature, explaining the better accuracy of TSM with the fast signal.

However, the larger cutoff wave number also distributes apparent distributed-surface roughness into the large-scale surface after wave breaking. This gives Bragg resonance through KA, as shown by the synchronization of the signal strength oscillations in the SPM and KA results in Fig. 5.7. The tangent-plane assumption of KA is violated when Bragg-resonant small-scale roughness appears on the large-scale surface, giving an over-prediction of the HH scattering. The incorrect KA results lead to the over-prediction of the TSM results at HH. Similar error is not introduced at VV since the SPM results are still dominant.

At lower incidence, TSM with $K_c = k/1.0$ is even more accurate. The TSM calculation at an incidence angle of 70° is shown in Fig. 5.8. The small disagreements between the VV TSM and MM/GTD calculations at 570 ms and after 620 ms shown
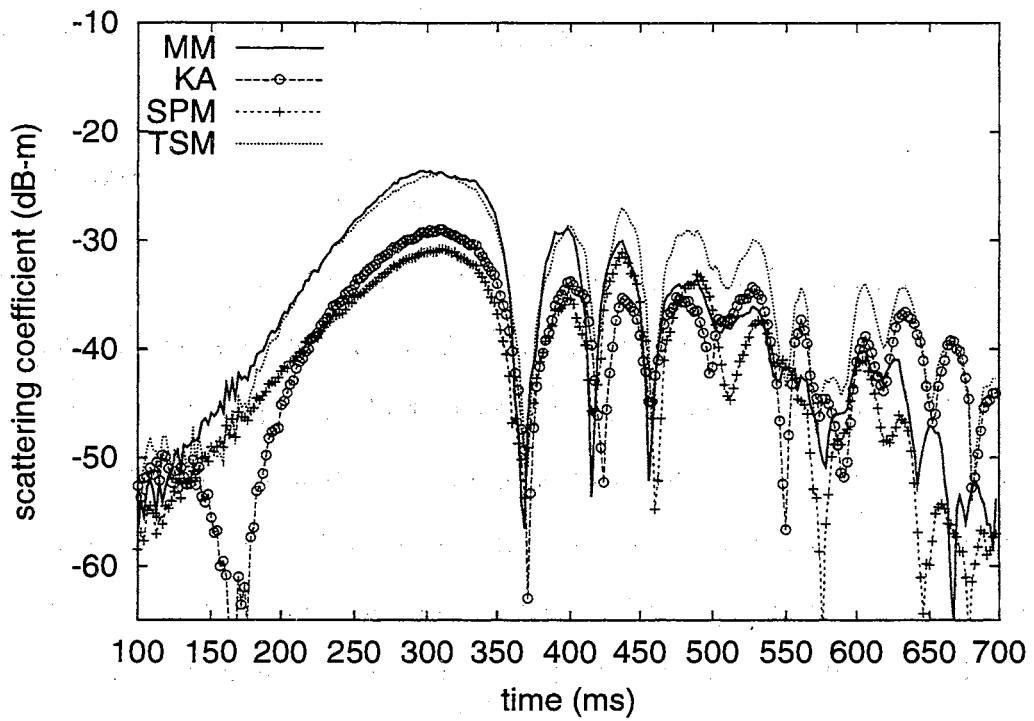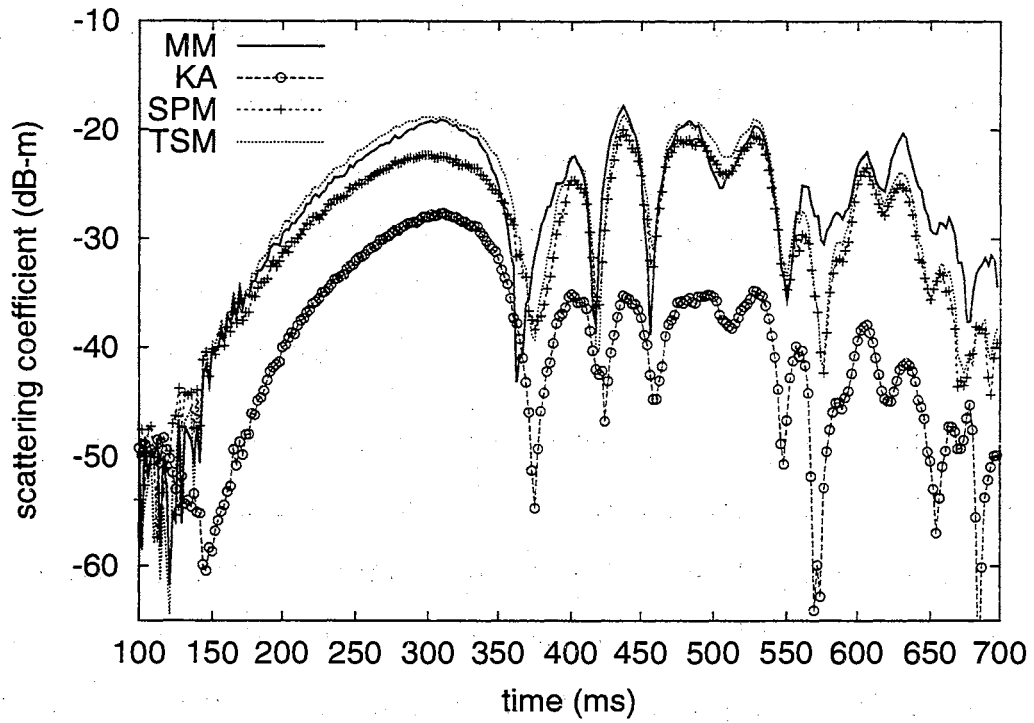
Figure 5.7: Same as Fig. 5.5, but with surfaces separated using $K_c = k/0.8$

in the 89° incidence results of Fig. 5.5 disappear at 70° incidence. The HH TSM results also agree well with MM/GTD well after 650 ms. It was shown in Chapter 4 that the contributions of the backscatter from the partially shadowed back side of the wave is significant at those moments. The TSM calculations are affected by the simplified shadowing treatment used there. The dominant scatterer is less severely shadowed at the lower angle incidence, and TSM regains accuracy.

5.3.2 "Surfactant" Waves

The TSM calculation of the backscatter from the "surfactant" wave at 10 GHz and 80° incidence using the cutoff wave number $K_c = k/1.0$ is shown in Fig. 5.9. The SPM results still dominate the TSM results at all time at VV polarization. The agreement at this polarization is very good at all times. At HH polarization, TSM under-predicts the reference MM/GTD by about 2 dB for the fast signal, and again gives a very accurate prediction in the slow scatter period.

5.4 Summary

The calculations show that TSM can give accurate predictions of the backscatter from both spilling breakers at 80° incidence and 10 GHz. A surface-separation cutoff wave number of $K_c = k$ gives acceptable TSM results overall. However, a larger cutoff wave number of $K_c = k/0.8$ can produce more accurate results with the clean wave before breaking. Roughness causes TSM to over-predict the scattering when a large amount of turbulent structure appears on the surface and is distributed into the large-scale surface. It is unrealistic to expect to use an optimal cutoff wave number suitable for different incidence angles, frequencies, and roughness distributions. However, it was shown that a larger cutoff such as $K_c = k/0.8$ may be more appropriate to separate comparatively smooth surfaces without large-amplitude roughness. This is because
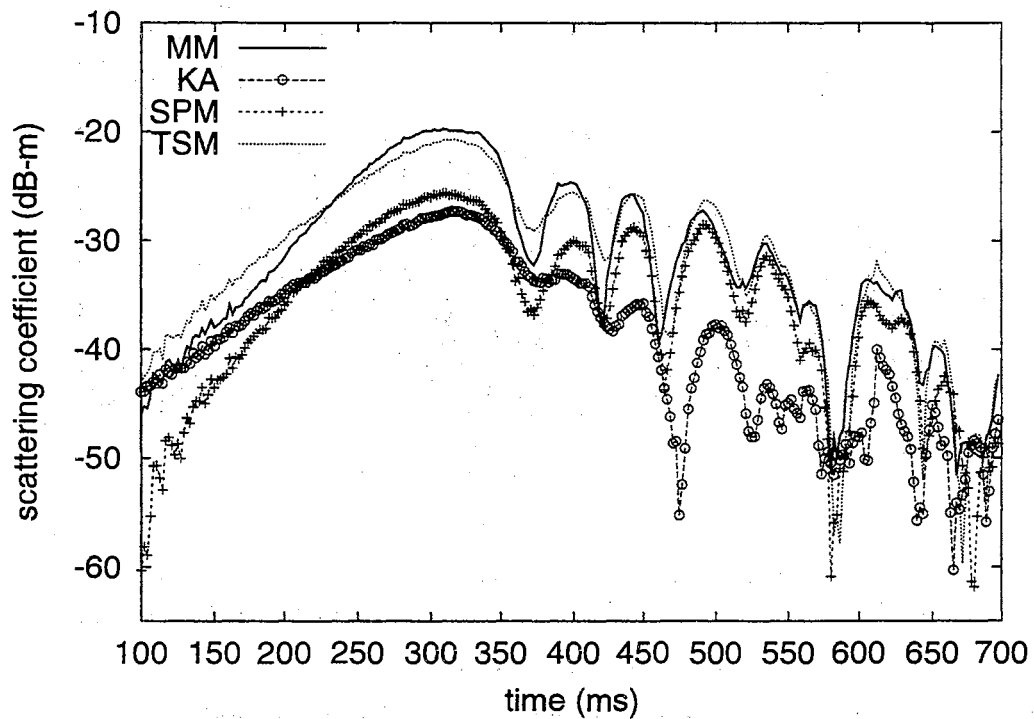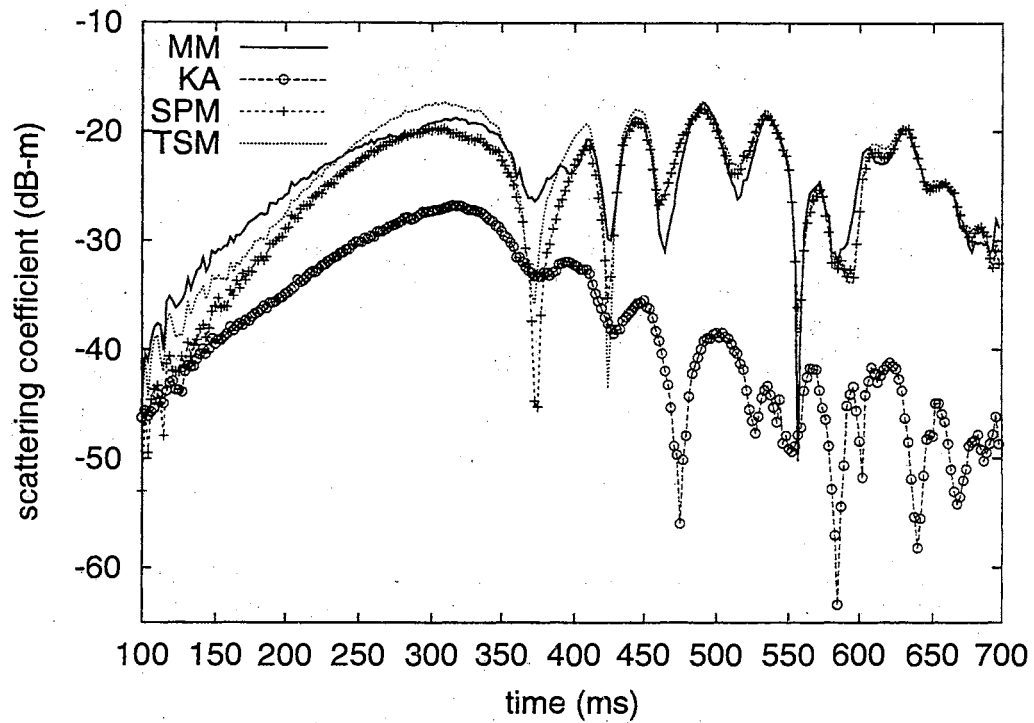
Figure 5.8: Same as Fig. 5.5, but at 70° incidence.
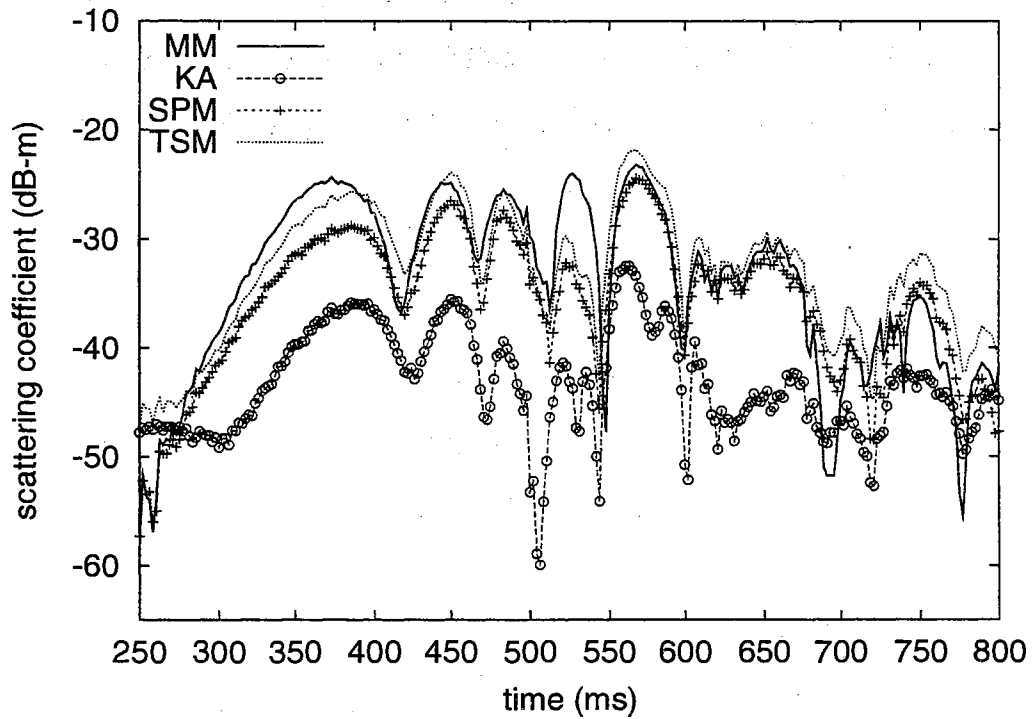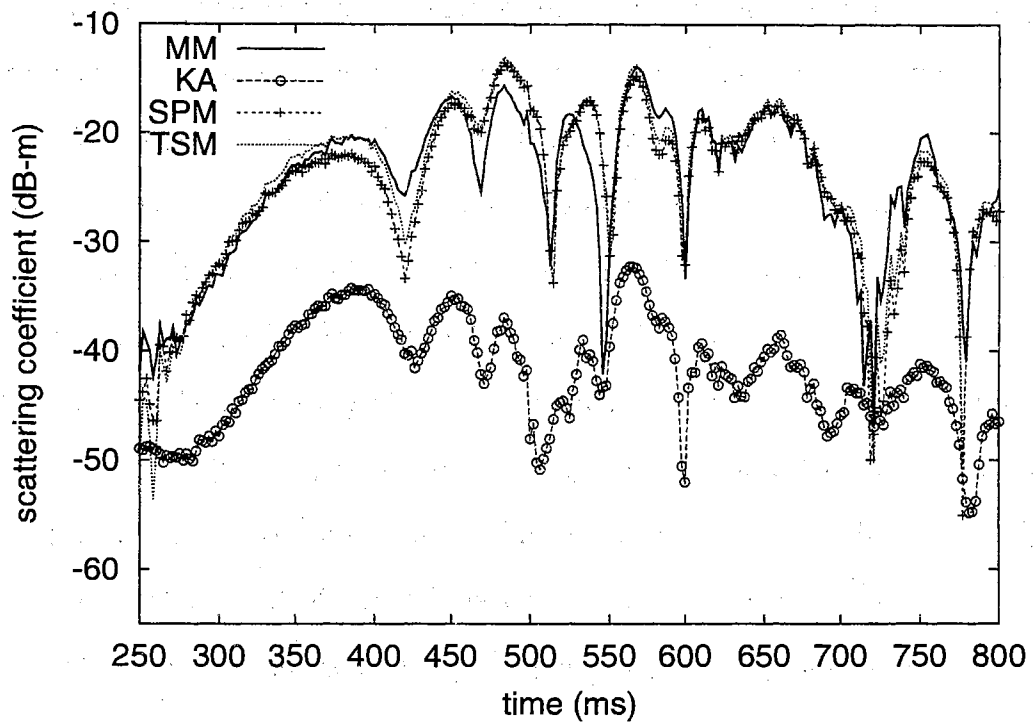
Figure 5.9: Backscattering from "surfactant" wave calculated using TSM with $K_c = k$ compared with the MM/GTD results s at 80° incidence and 10 GHz. (a) VV (upper plot). (b) HH (lower plot).

the larger cutoff places more of the plume feature energy into the large-scale surface, and KA is able to compute the diffractive scattering from that feature. After breaking, distributed-surface roughness appears on the surface, so a smaller cutoff such as $K_c = k$ or even smaller is appropriate. This distributes the small roughness into the small-scale surface where SPM correctly predicts the Bragg scattering. The TSM results at VV are less sensitive to a change in the cutoff wave number. Different cutoffs over a wide range from $k/1.7$ to $k/0.8$ only modified the relative levels of the SPM and KA scattering, but the TSM scattering after addition did not change significantly. On the other hand, TSM is very sensitive to surface energy distribution between the large- and small-scale surface at HH polarization. Since the HH SPM results are usually much smaller than the VV SPM results, the accuracy of KA becomes relatively more important. Therefore, maintaining the validity of the tangent-plane assumption is the most important consideration in choosing the cutoff for the implementation of TSM at HH polarization. Overall a cutoff wave number of $K_c = k$ gives acceptable TSM results for backscattering calculations at incidence angle of 80° and 10 GHz.

Chapter 6

CONCLUSIONS

Observations of large-incidence angle backscattering from the ocean surfaces have shown phenomena which are not explained by current analytical models. Sea spike events are short bursts of strong backscatters characterized by large HH/VV ratios. In some cases the HH return strengths can actually exceed those of VV. These are termed "super events". The decorrelation times of sea spikes are typically about several hundred milliseconds at HH polarization and only tens of milliseconds at VV. Another feature of large-incidence backscatter is the "Doppler split effect". The peaks of the Doppler shift of both polarizations are overlapping at low to moderate incidence angles. As the incidence angle increases the Doppler peak of the HH backscatter shifts to a higher frequency, while the VV peak stays at the lower frequency. The signals corresponding to the larger Doppler shift are termed "fast" signals, and signals producing smaller Doppler shift are termed "slow" signals. The above two mentioned events are beyond the prediction of two-scale model (TSM) which is the most commonly used analytical model for sea-surface scattering. Several models have been developed to explain the sea spike and Doppler splitting effect. Among them are the multi-path reflection model proposed by Wetzel [16] and extended to include Brewster angle damping by Trizna [17].

The goal of this study was to identify the "fast" and "slow" scatters through numerical calculation of the backscattering from two series of water wave profiles. The

hybrid MM/GTD numerical technique developed by West *et al.* [27] was applied to the individual deterministic water surface profiles to calculate the time history of the backscattering. The time histories of two mechanically generated spilling breaker waves, both generated without wind but with one including soap to act as a surfactant, were treated here.

The time histories of the backscattering at 80° incidence when looking upwind were found by finding the backscatter from each profiles in the wave history. The scattering was found at both 10 and 20 GHz. Two distinct types of responses appeared in the backscatter time history. The first appeared before wave breaking and was characterized by slowly rising amplitude. The second appeared after wave breaking, and was characterized by a rapidly oscillating amplitude. The time history of the Doppler spectra of the backscatter was also computed from the phase-preserved scattered field using a time dependent fast Fourier transform. The VV spectra of the "clean" waves included strong signals at both high and low Doppler frequencies. The HH spectrum also showed strong signals at the higher frequency but much weaker signals at the lower Doppler frequency. The above mentioned slowly rising-up signals corresponded to the higher Doppler frequency, and hence were recognized as the "fast" signal. Plume structures formed immediately before breaking were thought to be the "fast" scatterers. The rapidly-oscillating backscatter signals after breaking corresponding to the lower Doppler shift were the "slow" signals. Turbulence structures generated after breaking were recognized as the slow scatterers. Comparing time history of surface profiles to Doppler spectra identified the motions of the slow scatterers. The slow scatterers were shown to be turbulent cells generated after breaking that are carried by the orbital motion of the long wave. This comparison showed that major scatterers which produced strong backscattering were located on the front face of wave. The roughness on the back face did not produce significant backscattering.

105

The time history of the backscatter calculated from the "surfactant" wave was similar to that of the "clean" waves. However, the surfactant waves were more energetic than the clean waves, and there were several overturning events in this time history. All overturning events were matched by bursts of backscattering at HH. Super events have been observed in the 20 GHz response during the first two overturning events. The steep features which gave strong HH returns were more often seen in this wave history. Therefore the slow-signal strengths at HH did not drop as fast as those in the "clean" waves.

Oscillation of the slow signal strength was well explained by Bragg scattering theory. Changing of the tilting or the distance between turbulent cells shifted the surface small-scale roughness energy into or away from the Bragg wave number, and hence caused fluctuations in the Bragg scattering. The VV/HH ratios of the numerical calculations also had good agreement with the SPM α ratios at most of the time. These agreements suggested that the Bragg scattering was the major scattering mechanism after wave breaking. Non-Bragg diffractive scattering is believed to be the scattering mechanism before wave breaking.

The modeled surface profiles were artificially extended horizontally to give a multi-path reflection backscatter path from the plume structure. Super events were observed in the backscattering from the extended surface at 80° incidence and 10 GHz while larger HH/VV ratios were seen at other incidence angles. Only the backscatter strength prior to wave breaking was changed by to the multi-path reflection. The interference altered the fast backscatter strength at HH and VV respectively, and hence large HH/VV ratios may be observed at specific incidence angles and frequencies in the fast signal region. The backscatter after wave breaking was not affected.

Finally, the performance of a two-scale model implementation that can be applied to deterministic surfaces in predicting the scattering from the breaking wave profiles

was examined. The numerical MM/GTD calculations served as the exact results to which the TSM results were compared. The cutoff wave number used when separating the surface into large- and small-scale components was shown to have a significantly affect on the accuracy of TSM. Cutoff wave number of $K_c = k$ gave a good compromise for overall accuracy in the slow and fast signal regions. TSM was very accurate in predicting the VV backscatter at $80°$ incidence and 10 GHz throughout the wave evolution. However, it significantly under-predicted the HH fast backscatter. While it is unrealistic to find an optimal cutoff wave number for all combinations of incidence angle, frequency, and roughness distributions, some insight to the choice of the proper cutoff has been gained through this study. The TSM scattering at VV polarization was not significantly affected by the cutoff wave number used. However, the HH scattering is more strongly dependent on KA scattering from the large-scale surface. Hence, the choice of cutoff wave number should weigh more strongly on maintaining the accuracy of the tangent-plane assumption on the large-scale surface.

BIBLIOGRAPHY

[1] P. H. Y. Lee, J. D. Barter, K. L. Beach, C. L. Hindman, B. M. Lake, H. Run-galdier, J. C. Shelton, A. B. Williams, R. Yee, and H. C. Yuen, "X band microwave backscattering from ocean waves", *Journal of Geophysical Research*, vol. 100, no. C2, pp. 2591–2611, Feb. 1995.

[2] P. H. Y. Lee, J. D. Barter, K. L. Beach, B. M. Lake, H. Rungaldier, H. R. Thompson Jr., and R. Yee, "Scattering from breaking gravity waves without wind", *IEEE Transactions on Antennas and Propagation*, vol. 46, no. 1, pp. 14–25, Jan. 1998.

[3] J. W. Wright, "A new model for sea clutter", *IEEE Transactions on Antennas and Propagation*, vol. AP-16, no. 2, pp. 217–223, May 1965.

[4] G. R. Valenzuela, "Scattering of electromagnetic waves from a tilted, slightly rough surface", *Radio Science*, vol. 3, no. 11, pp. 1057–1066, Nov. 1968.

[5] P. Beckmann and A. Spizzichino, *The Scattering of Electromagnetic Waves from Rough Surfaces*, Pergamon, New York, 1963.

[6] S. O. Rice, "Reflection of electromagnetic wave from slightly rough surfaces", *Communications in Pure and Applied Mathematics*, vol. 4, no. 2, pp. 351–378, Aug. 1951.

[7] F. T. Ulaby, R. K. Moore, and A. K. Fung, *Microwave Remote Sensing: Active and Passive*, vol. 2, Artech House, Norwood, Massachusetts, 1986.

[8] J. C West, "Effect of shadowing on electromagnetic scattering from rough ocean-wave-like surface at small grazing angles", *IEEE Transactions on Geoscience and Remote Sensing*, vol. 35, no. 2, pp. 293–301, Mar. 1997.

[9] A. I. Kalmykov and V. V. Pustovoytenko, "On polarization feature of radio signals scattered from the sea surface at small grazing angles", *Journal of Geophysical Research*, vol. 76, pp. 1960–1964, 1976.

[10] D. B. Trizna, J. P. Hansen, P. Hwang, and J. Wu, "Laboratory studies of radar sea spikes at low grazing angles", *Journal of Geophysical Research*, vol. 97, no. C7, pp. 12529–12537, 1991.

[11] W. Alpers, D. B. Ross, and C. L. Rufenach, "On the detectability of ocean surface wave by real and synthetic aperture radar", *Journal of Geophysical Research*, vol. 86, no. C7, pp. 6481–6498, 1981.

[12] D. R. Lyzenga, A. L. Maffett, and R. A. Shuchman, "The contribution of wedge scattering to the radar cross section of the ocean surface", *IEEE Transactions on Geoscience and Remote Sensing*, vol. GE-21, no. 4, pp. 502–505, Oct. 1983.

[13] J. R. Duncan, W. C. Keller, and J. W. Wright, "Fetch and wind speed dependence of Doppler spectra", *Radio Science*, , no. 9, pp. 809–819, 1974.

[14] A. T. Jessup, W. C. Keller, and W. K. Melville, "Measurements of sea spikes in microwave backscatter at moderate incidence", *Journal of Geophysical Research*, vol. 95, pp. 9679–9688, 1990.

[15] W. J. Plant, "A model for microwave Doppler sea return at high incidence angles: Bragg scattering from bound, tilted waves", *Journal of Geophysical Research*, vol. 102, no. C9, pp. 21,131–21,146, Sept. 1997.

[16] L. Wetzel, "On microwave scattering by breaking waves", in *Wave Dynamics and Radio Probing of the sea surface*, O. M. Phillips and K. Hasselmann, Eds., pp. 273–283. Plenum, 1986.

[17] D. B. Trizna, "A model for Brewster angle effects on sea surface illumination for sea scatter studies", *IEEE Transactions on Geoscience and Remote Sensing*, vol. 36, no. 5, pp. 1232–1244, Sept. 1997.

[18] Kwoh D. S., B. M. Lake, and H. Rungaldier, "Microwave scattering from internal wave modulated surface waves: A shipboard real aperture coherent radar study in the georgia strait experiment", *Journal of Geophysical Research*, vol. 93, no. C10, pp. 12,235–12,248, 1988.

[19] J. C. West, J. M. Sturm, and Sletten M., "Small grazing angle radar scattering from a breaking water wave: demonstration of Brewster angle damping", *Geoscience and Remote Sensing Symposium*, vol. 4, pp. 2207–2209, 1996.

[20] J. C. West, "Ray analysis of low-grazing scattering from a breaking water wave", *IEEE Transactions on Geoscience and Remote Sensing*, 1999, in press.

[21] V. W. Pidgeon, "Doppler dependence of radar sea return", *Journal of Geophysical Research*, vol. 73, pp. 1333–1341, Feb. 1968.

[22] G. R. Valenzuela and M.B. Laing, "Study of Doppler spectra of radar sea echo", *Journal of Geophysical Research*, vol. 75, no. 3, pp. 551–563, Jan. 1970.

[23] M. J. Smith, E. M. Poulter, and J. A. McGregor, "Doppler radar measurements of wave groups and breaking waves", *Journal of Geophysical Research*, vol. 101, no. C6, pp. 14,269–14,282, June 1996.

[24] W.C. Keller, W. J. Plant, and G. R. Valenzuela, "Observations of breaking ocean waves with coherent microwave radar", in *Wave Dynamics and Radio Probing of the Sea Surface*, O. M. Phillips and K. Hasselmann, Eds., pp. 286–293. Plenum, 1986.

[25] J. T. Johnson, T. S. Robert, J. A. Kong, L. Tsang, and Pak K., "A numerical study of the composite surface model for ocean backscattering", *IEEE Transactions on Geoscience and Remote Sensing*, vol. 36, no. 1, pp. 72–82, 1998.

[26] W. D. Burnside, C. L. Yu, and R. J. Marhefka, "A technique to combine the geometrical theory of diffraction and the moment method", *IEEE Transactions on Antennas and Propagation*, vol. AP-23, no. 4, pp. 551–558, July 1975.

[27] J. C. West, J. M. Sturm, and S.-J. Ja, "Low-grazing scattering from breaking water waves using impedance boundary MM/GTD approach", *IEEE Transactions on Antennas and Propagation*, vol. 46, no. 1, pp. 93–100, Jan. 1998.

[28] W. J. Pierson and L Moskowitz, "A proposed spectral form for fully developed wind seas based on the similarity theory of S. A. Kitaigorodskii", *Journal of Geophysical Research*, vol. 69, pp. 5181–5190, 1964.

[29] M. A. Donelan and W. J. Pierson, "Radar scattering and equilibrium ranges in wind-generated waves with application to scatterometry", *Journal of Geophysical Research*, vol. 92, pp. 4971–5029, 1987.

[30] J. H. Duncan, V. Philomin, H. Qiao, and J. Kimmel, "Formation of a spilling breaker", *Physics of Fluids*, vol. 6, no. 8, pp. 2560–2561, Aug. 1994.

[31] C. A. Balanis, *Advanced Engineering Electromagnetics*, Wiley, New York, 1989.

[32] M. I. Skolnik, *Radar Handbook*, McGraw-Hill, New York, 1970.

[33] J. W. Wright, "Backscattering from capillary waves with application to sea clutter", *IEEE Transactions on Antennas and Propagation*, vol. AP-16, no. 2, pp. 217–223, May 1965.

[34] A. K. Fung and M. F. Chen, "Numerical simulation of scattering from simple and composite random surfaces", *Journal of the Optical Society of America, Series A*, vol. 2, no. 12, pp. 2274–2284, Dec. 1985.

[35] G. S. Brown, "Backscattering from a Gaussian-distributed perfectly conducting rough surface", *IEEE Transactions on Antennas and Propagation*, vol. AP-26, no. 3, pp. 474–475, May 1978.

[36] W. L. Stutzman and G. A. Thiele, *Antenna Theory and Design*, John Wiley and Sons, New York, 1981.

[37] G. R. Valenzuela, "The effect of capillarity and resonant interactions on the second-order doppler spectrum of radar sea echo", *Journal of Geophysical Research*, vol. 49, pp. 5031–7037, 1974.

[38] M. L. Burrows, "A reformulated boundary perturbation theory in electromagnetism and its application to a sphere", *Canadian Journal of Physics*, vol. 45, pp. 1729–1743, May 1967.

[39] J. C. West, "Electromagnetic scattering from finite conductivity wind-roughened water surfaces", *IEEE Transactions on Geoscience and Remote Sensing*, 1999, in press.

[40] S. L. Durden and Vesecky J. F., "A numerical study of the separation wavenumber in the two-scale scattering approximation", *IEEE Transactions on Geoscience and Remote Sensing*, vol. 28, no. 2, pp. 271–272, Mar. 1990.

[41] J. C. West, B. S. O'leary, and J. Klinke, "Numerical calculation of electromagnetic scattering from measured wind-roughened water surface", *International Journal of Remote Sensing*, vol. 19, no. 7, pp. 1377–1393, 1998.

[42] R. F. Harrington, *Field Computation by Moment Methods*, Robert E. Krieger Publishing Co., Florida, 1982.

[43] J. M. Sturm and J. C. West, "Numerical study of shadowing in electromagnetic scattering from rough dielectric surfaces", *IEEE Transactions on Geoscience and Remote Sensing*, vol. 36, no. 5, pp. 1477–1484, Sept. 1998.

[44] T. B. A. Senior and J. L. Volakis, "Generalized impedance boundary conditions in scattering", *Proceedings of the IEEE*, vol. 79, no. 10, pp. 1413–1420, Oct. 1991.

[45] E. I. Thorsos, "The validity of the Kirchhoff approximation for rough surface scattering using a Gaussian roughness spectrum", *Journal of the Acoustical Society of America*, vol. 83, no. 1, pp. 78–82, Jan. 1988.

[46] J. M. Sturm, *Numerical Investigation of Radar Scattering From Rough Land Surface*, Oklahoma State University, School of Electrical and Computer Engineering, Stillwater, Oklahoma 74078, 1996.

[47] A. V. Oppenheim and R. W. Schafer, *Discrete-Time Signal Processing*, Prentice-Hall, New Jersey, 1989.

[48] A. K. Cline, "FITPACK", *http://www.netlib.org/fitpack/index.html*.

VITA

SHIOU-JYH JA

Candidate for the Degree of

Doctor of Philosophy

Thesis: NUMERICAL STUDY OF MICROWAVE BACKSCATTERING
FROM BREAKING WATER WAVES

Major Field: Electrical Engineering

Biographical:

Personal Data: Born in Tainan, Taiwan, on September 13, 1968, the son of
Gong-ming Ja and Chiao-su Lee.

Education: Received Bachelor of Science in Electro-Physics from National Chiao-
Tung University, Hsin-Chu, Taiwan in May 1991, and Master of Science
in Electrical Engineering from Oklahoma State University, Stillwater, Ok-
lahoma in December 1995. Completed the requirements for the Doctor of
Philosophy degree in Electrical Engineering at Oklahoma State University
in December 1999.

Professional Experience: Research Assistant at Oklahoma State University De-
partment of Electrical and Computer Engineering from January 1996 to
December 1999.